Collected figures from HELIOPHYSICS II. SPACE STORMS AND RADIATION: CAUSES AND EFFECTS

edited by
CAROLUS J. SCHRIJVER
Lockheed Martin Advanced Technology Center
and
GEORGE L. SISCOE
Boston University

This document contains the figures from the published volume of Heliophysics II as submitted to Cambridge University Press, prior to possible revisions in the graphics and captions during the copy editing process. This collection is intended only as an aid to students and teachers for use in, e.g., lectures and study sessions.

Contents

1

Perspective on heliophysics

by George L. Siscoe and Carolus J. Schrijver

2

Introduction to space storms and radiation

by Sten Odenwald

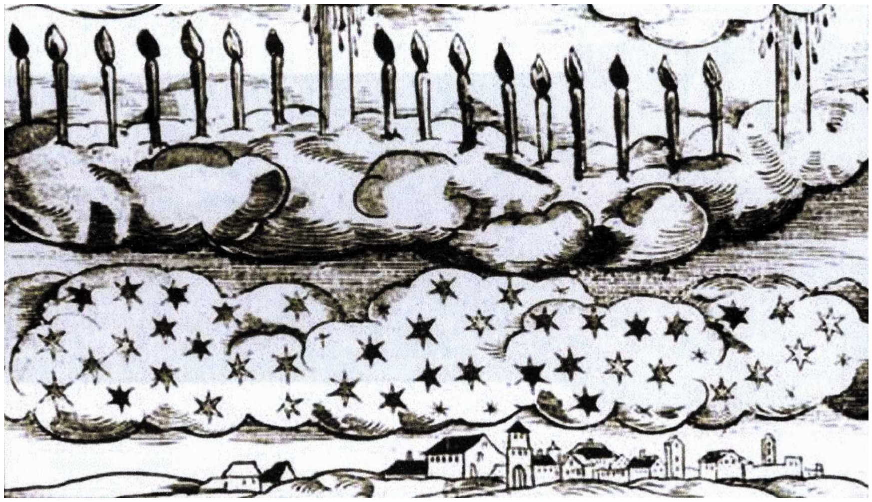

Fig. 2.1. Early drawing of the aurora, depicted as candles in the sky; ca. 1570. Original print in Crawford Library, Royal Observatory, Edinburgh.

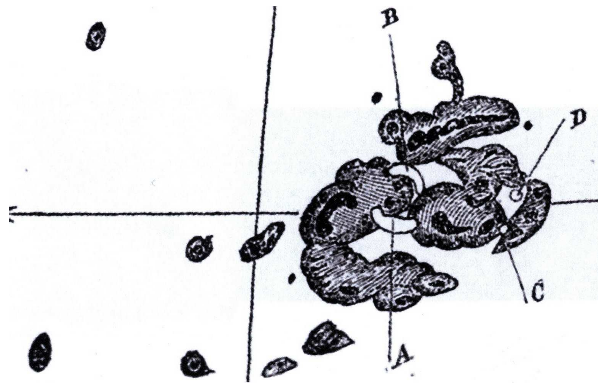

Fig. 2.2. Carrington's sketch at 11:18 GMT on September 1, 1859 of the sunspot and the lettered (white) flaring regions (from Carrington, 1859).

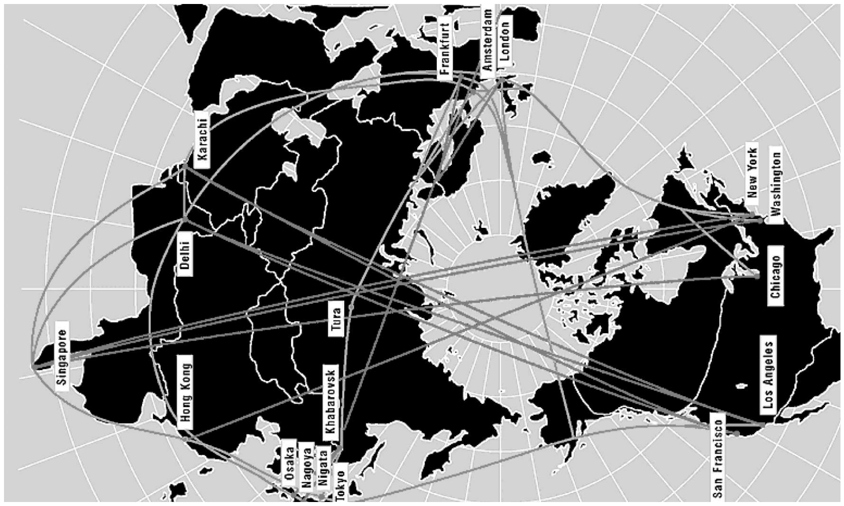

Fig. 2.3. Polar airline routes used by United Airlines ca. 2006 carrying 1,500 flights per year. (Courtesy Hank Krakowski)

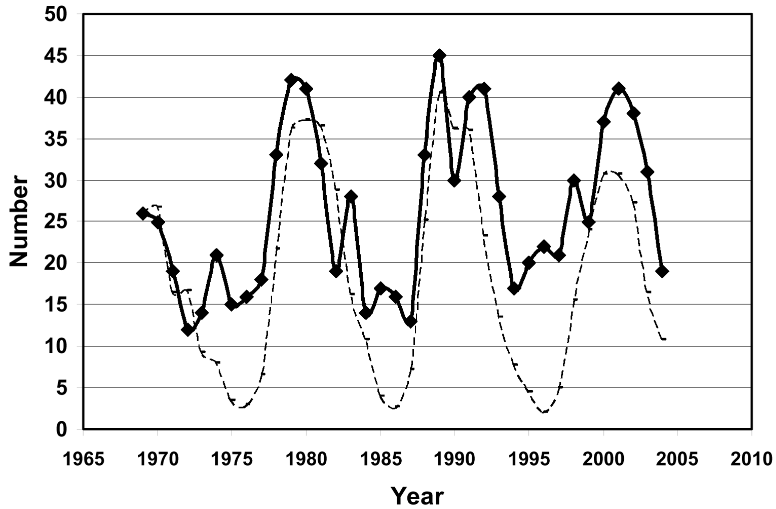

Fig. 2.4. The number of de-orbited satellites in low-Earth orbit (LEO) compared to the sunspot cycle (Odenwald, Green and Taylor, 2006)

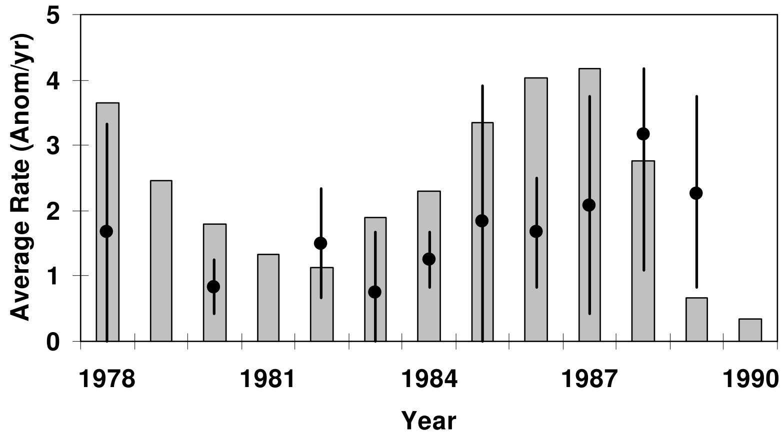

Fig. 2.5. Satellite anomaly rates for satellites in geosynchronous Earth orbit (GEO) listed in the NGDC anomaly archive. The reference histogram is the annual cosmic ray flux at Climax, re-scaled to show phase. (Odenwald, 2009)

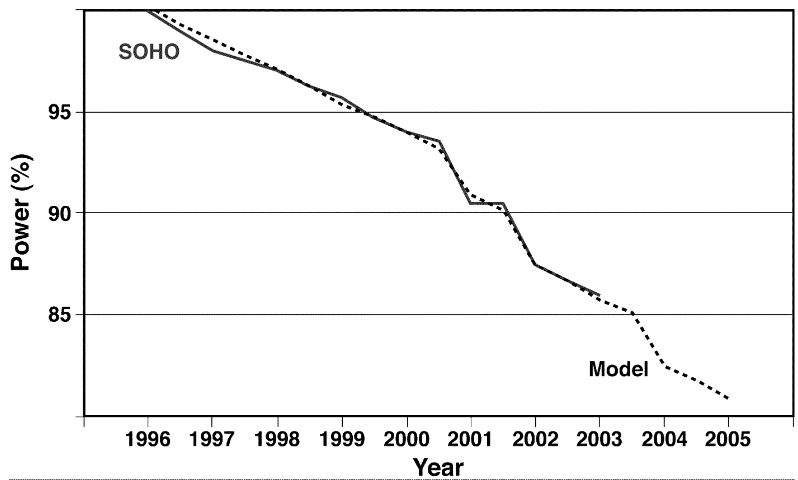

Fig. 2.6. Solar panel power reduction for SOHO from 1996-2003. The model (dashed line) includes a 2% GCR decline per year and the effects of known SPE events. The large dip near the center of the curve was the Bastille Day event in July, 2000. A second drop occurred during the intense SPEs on November 4 and 23, 2001 (from Odenwald et al, 2005).

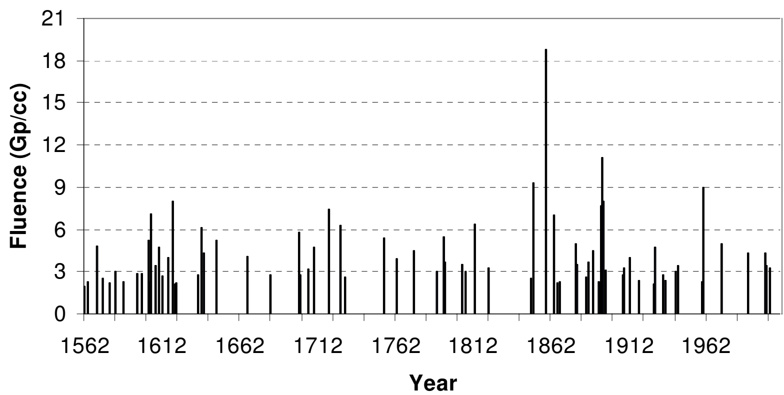

Fig. 2.7. Fluences (10^9 particles/cm^3) at Earth for energies exceeding 30 MeV SPE events since 1562 derived from NOy abundance anomalies in ice cores. September 2, 1859 is the most intense event in 500 years. Note that the November 15, 1960 event (5$^{\text{th}}$ from the right) predates the commercial satellite era that started around 1980 (from McCracken et al., 2001).

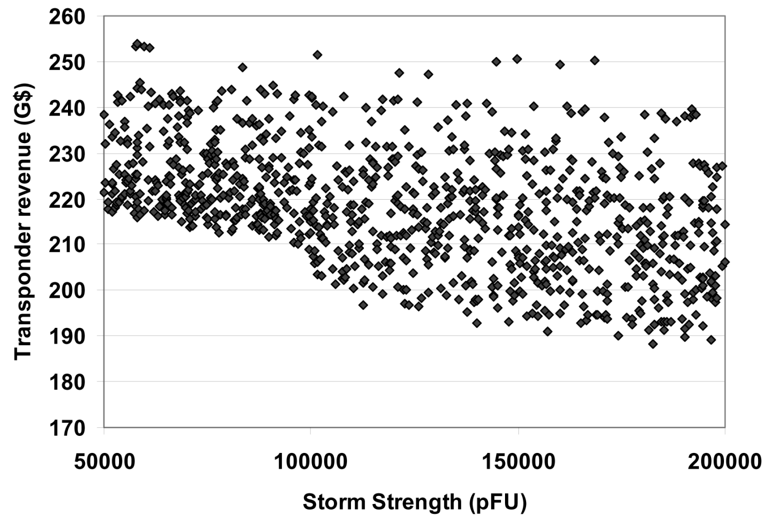

Fig. 2.8. Monte-Carlo model results for cumulative transponder revenue versus storm strength in units of particle flux units (pfu = particles/cm^2/sec). The 1859 Superstorm event would appear at about 150,000 pfu. The largest SPE events during cycles 22-23 equalled 45,000 pfu. The vertical dispersion is due to the variation of the onset year from 2008 to 2018 (from Odenwald and Green, 2007).

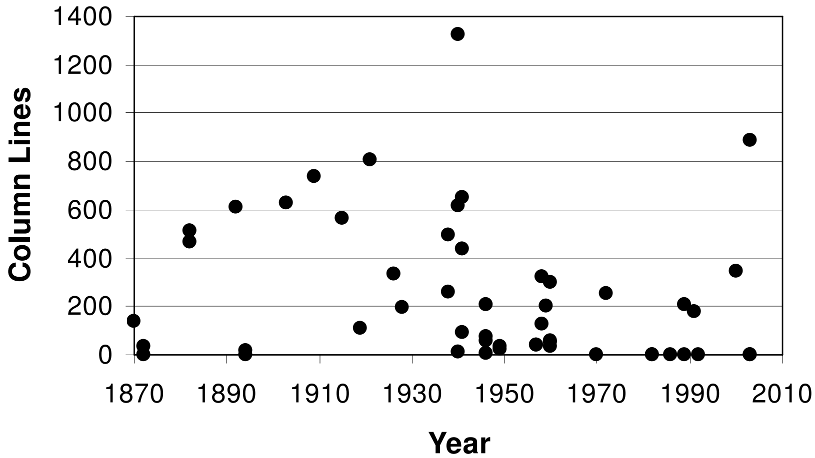

Fig. 2.9. The total number of space weather-related column lines per year published by the New York Times, Chicago Tribune, Boston Globe, Los Angeles Times and the Washington Post for space storms occurring each year with geomagnetic AA index exceeding 150, showing a sharp decline in coverage after ca. 1950 (from Odenwald, 2007).

3

In-situ detection of energetic particles

by George Gloeckler

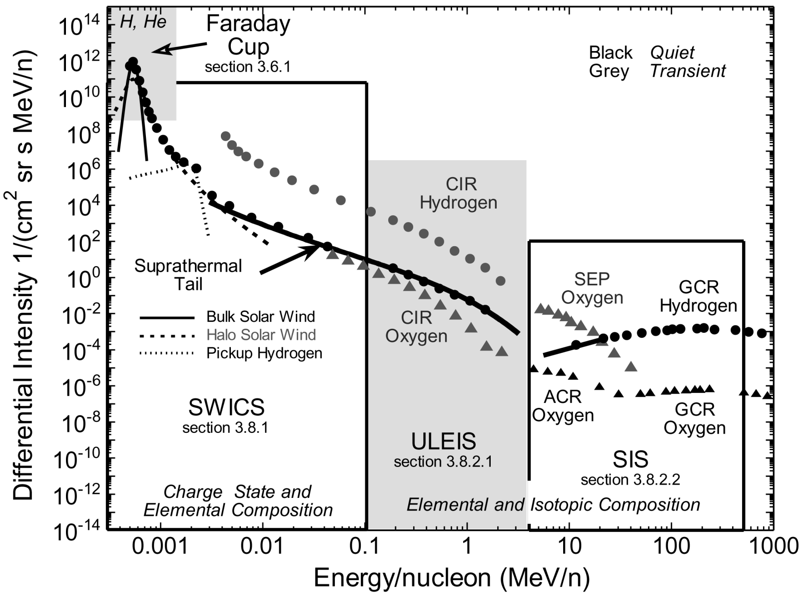

Fig. 3.1. Differential intensities of protons (circles) and oxygen ions (triangles) for various particle populations (see Ch. 9 for a description of the populations) observed in the heliosphere. The four shaded boxes represent the energy and dynamic ranges of four instruments (described in Section 3.8) that measure the energy spectra and composition of ions and nuclei (cf., Fig. 9.1). Symbols: black - quasi-steady state; grey - transient states.

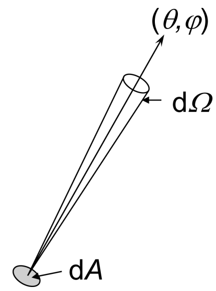

Fig. 3.2. Ideal small detector of area dA with a narrow conical field of view dΩ centered on its look direction.

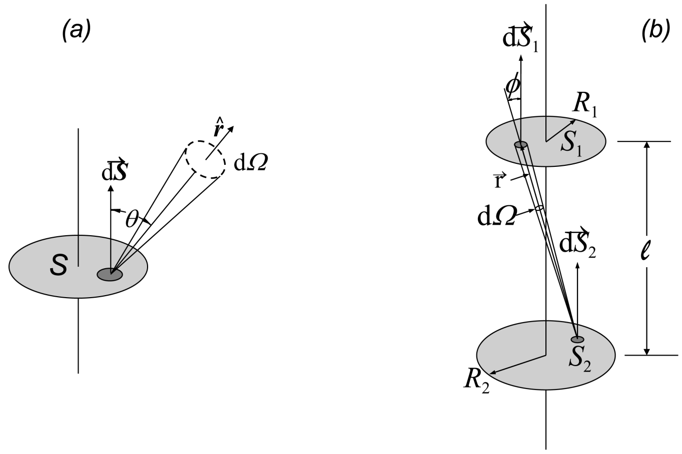

Fig. 3.3. Relationship (a) between dS, dΩ, $\mathbf{r}$ and Θ for a single planar detector and (b) between dS_1, dS_2 dΩ, $\mathbf{r}$ and Θ for a two-detector telescope.

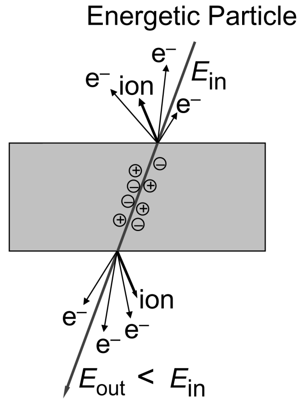

Fig. 3.4. Interaction of an energetic particle with a slab of material showing the ejection of electrons and ions from the two surfaces and ionization of matter inside the slab. The average charge state of the particle leaving the slab will depend primarily on its energy and not on its initial degree of ionization. For example, an energetic neutral atom will most likely be charged when exiting the slab.

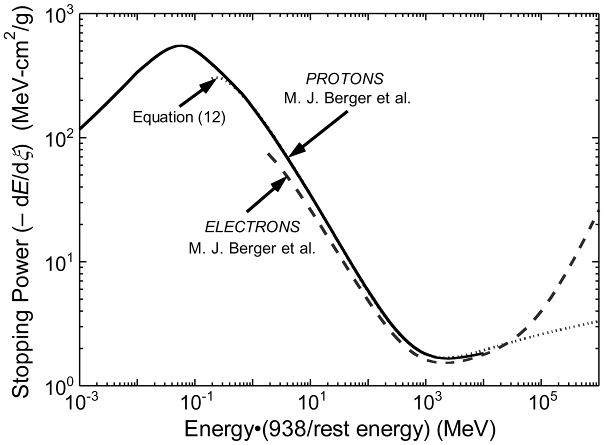

Fig. 3.5. Comparison of the stopping power for protons traversing silicon computed using Eq. (3.12) with that based on experimental stopping power data (Berger et al., http://physics.nist.gov/PhysRefData/Star/Text/contents.html).

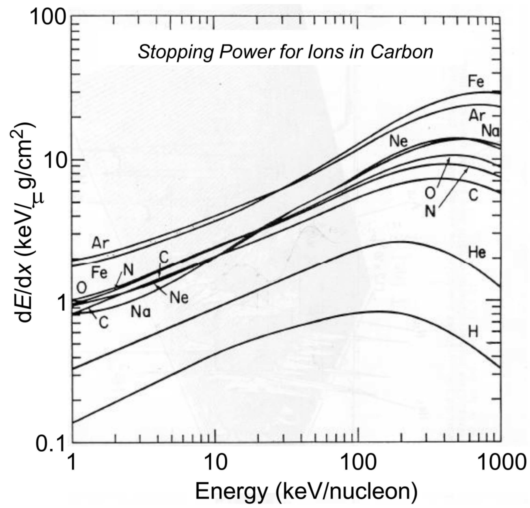

Fig. 3.6. Energy loss in thin carbon foils for energetic particles of various elements. (from Gloeckler et al., 1980, private communication)

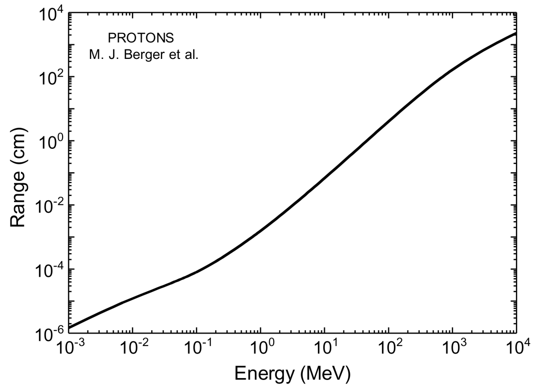

Fig. 3.7. Range of protons in silicon, based on experimental data compiled by Berger et al.; see http://physics.nist.gov/PhysRefData/Star/Text/contents.html.

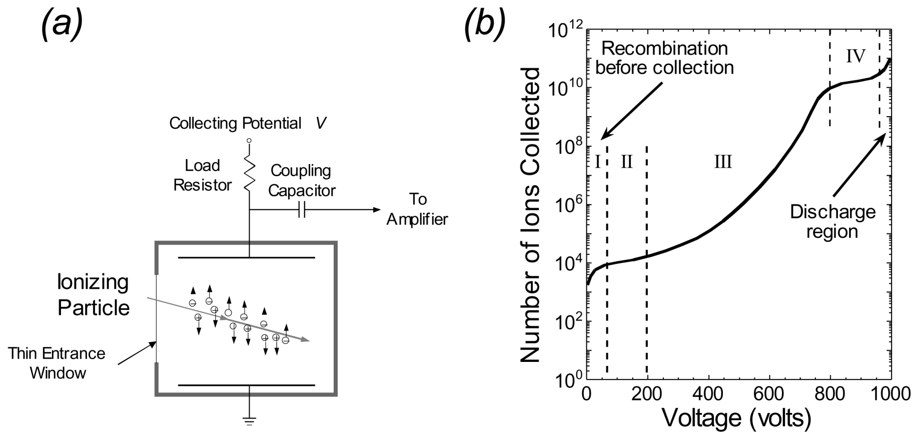

Fig. 3.8. *(a)* Schematic diagram of a gaseous ionization chamber. *(b)* Collected counts or pulse height as a function of applied voltage, illustrating the regions of operation of a gas chamber. Regions II, II and IV correspond respectively to the ionization chamber, the proportional counter and the Geiger counter mode of operation. (from Gloeckler, 1970)

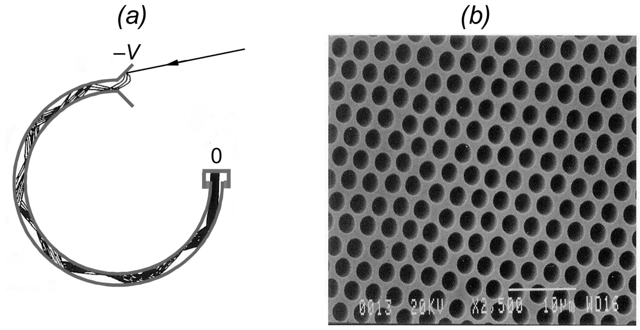

Fig. 3.9. (a) Cross section of a channeltron. (b) Photograph of a section of the surface of a microchannel plate. Courtesy of Burle Industries, Inc.

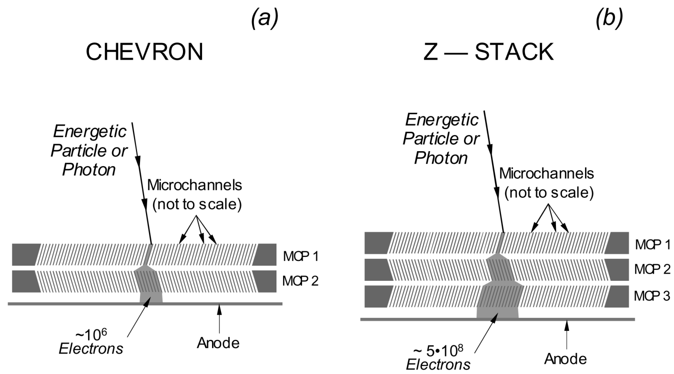

Fig. 3.10. Schematic drawing of MCPs in a chevron (a) and in a Z-stack arrangement (b). A single energetic particle enters one microchannel of MCP 1 and initiates a secondary electron avalanche in that channel. The cloud of electrons leaving that MCP then spreads to several microchannels of the next plate staring avalanches in each of these channels. About 10^6 electrons are collected by the anode behind the chevron configuration and $\sim 5\,10^7$ in the Z-stack arrangement.

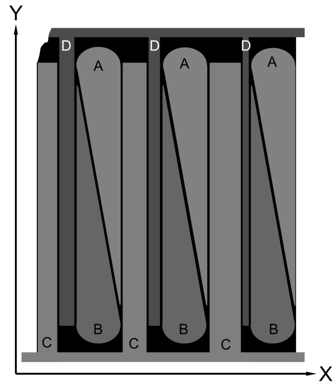

Fig. 3.11. A portion of a four-electrode wedge and strip anode. Black regions are insulators, the rest conductors. Each set of wedges and strips labeled A, B, C and D, respectively are tied together to four separate conductors on the back of the anode. The X and Y positions are given by the ratio of signals: $X = C/(C + D)$ and $Y = A/(A + B)$.

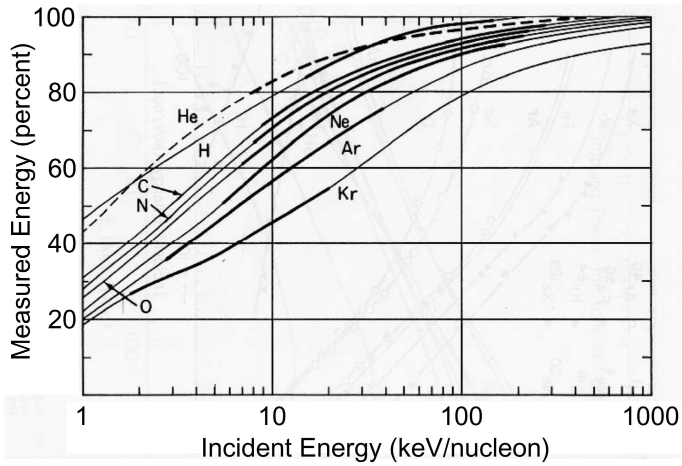

Fig. 3.12. Total energy defect in solid-state detectors with 19 mg/cm^2 Au front surface for ions H through Kr between 1 and 1000 keV/nucleon. Bold curves are least squares fits of measurements. From Ipavich et al. (1978).

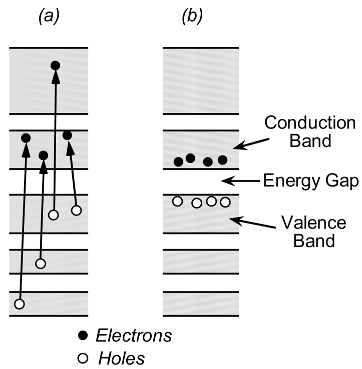

Fig. 3.13. Production of electrons and holes in a semiconductor resulting from passage of an energetic particle. *(a)* Initial conditions with highly excited states; *(b)* residual excitation after about 10^{-12} s.

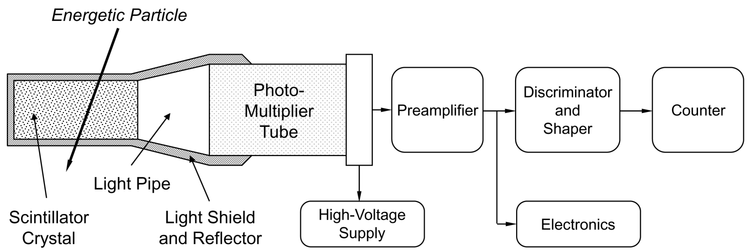

Fig. 3.14. Diagram of a scintillation detector with typical electronic circuitry.

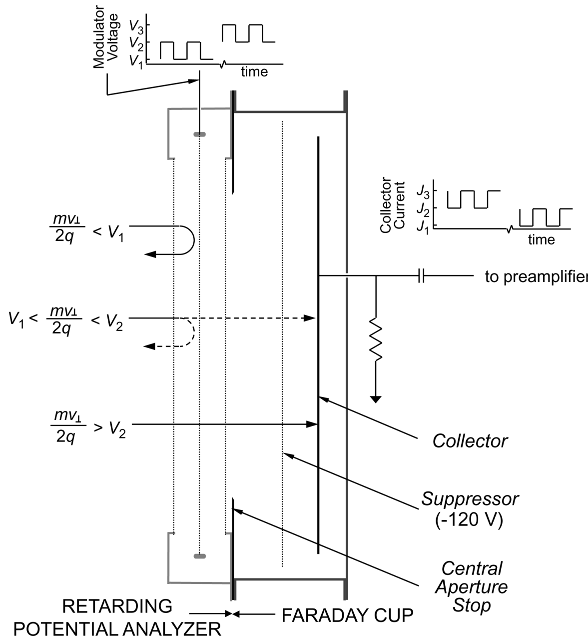

Fig. 3.15. Simplified cross sectional view of the Faraday cup sensor on the Wind spacecraft. The retarding potential analyzer section is on the left. The Faraday cup section is shown on the right. From Ogilvie et al. (1995).

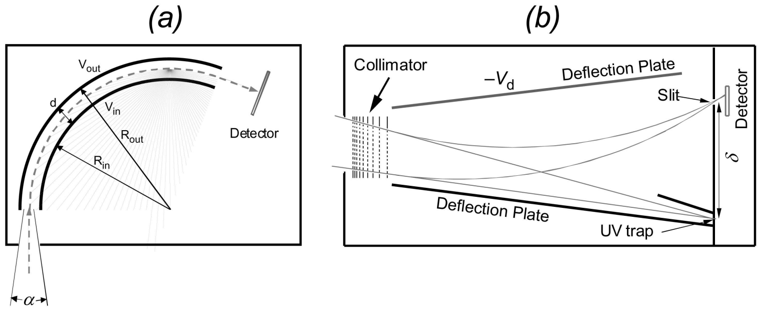

Fig. 3.16. Schematic representations of (a) a typical spherical or cylindrical section electrostatic deflection analyzer illustrating its principle of operation, and (b) the cross section of a typical small-angle deflection analyzer.

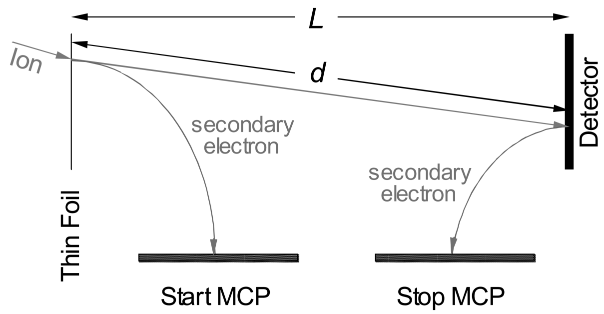

Fig. 3.17. Diagram of the cross section of a typical Time-of-Flight (TOF) telescope illustrating its principle of operation.

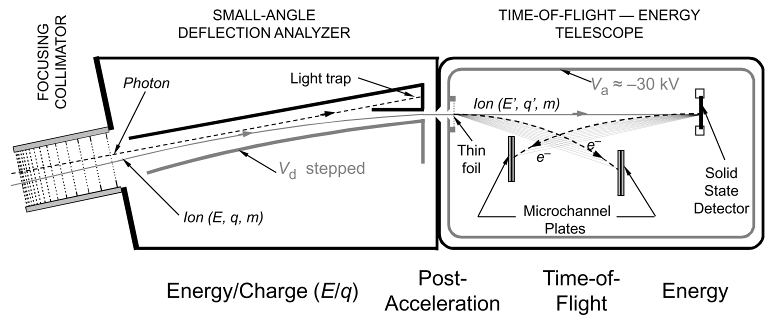

Fig. 3.18. Diagram of the measurement technique used in SWICS.

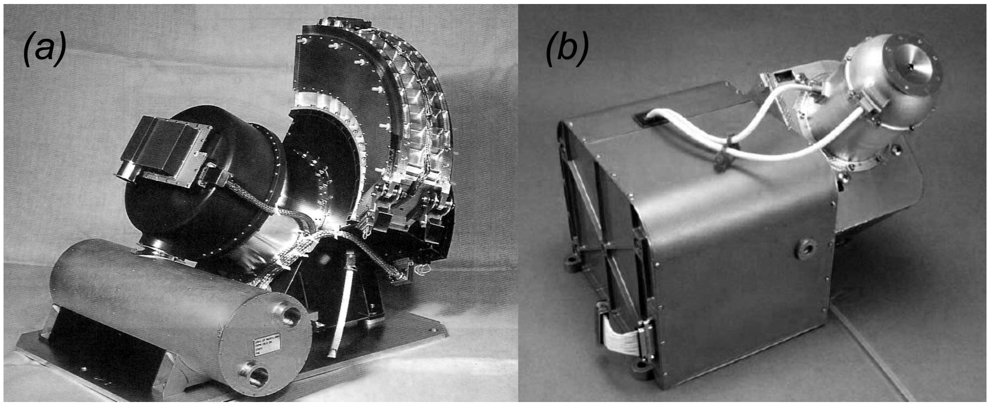

Fig. 3.19. Photographs of (a) the Solar Wind Ion Composition Spectrometer (SWICS) on Ulysses and ACE (from Gloeckler et al., 1992), and (b) of the Fast Imaging Plasma Spectrometer (FIPS) on MESSENGER (from Andrews et al., 2007).

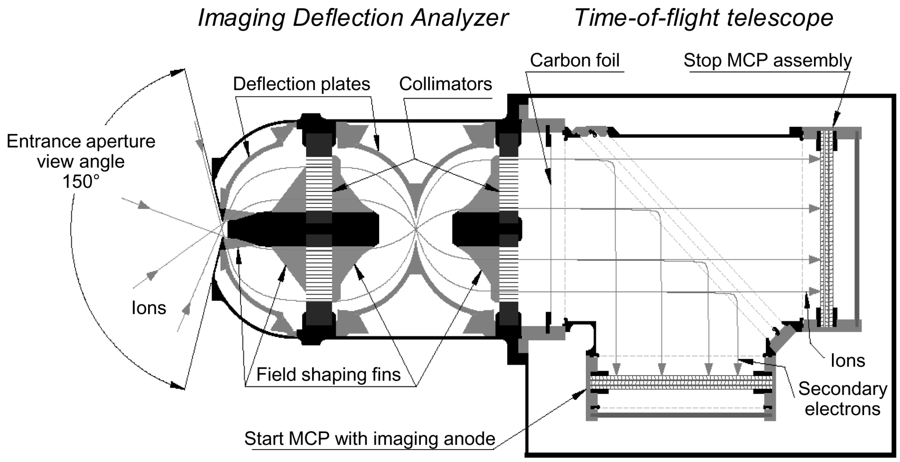

Fig. 3.20. Schematic cross section of the Fast Imaging Plasma Spectrometer (FIPS). The distance between the carbon foil and the Stop MCP is 7 cm. (from Andrews et al., 2007)

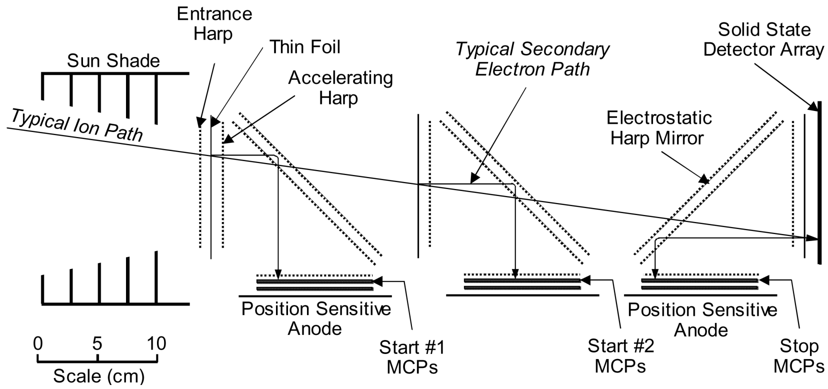

Fig. 3.21. Schematic cross section of the Ultra-Low-Energy Isotope Spectrometer. (from Mason et al., 1998)

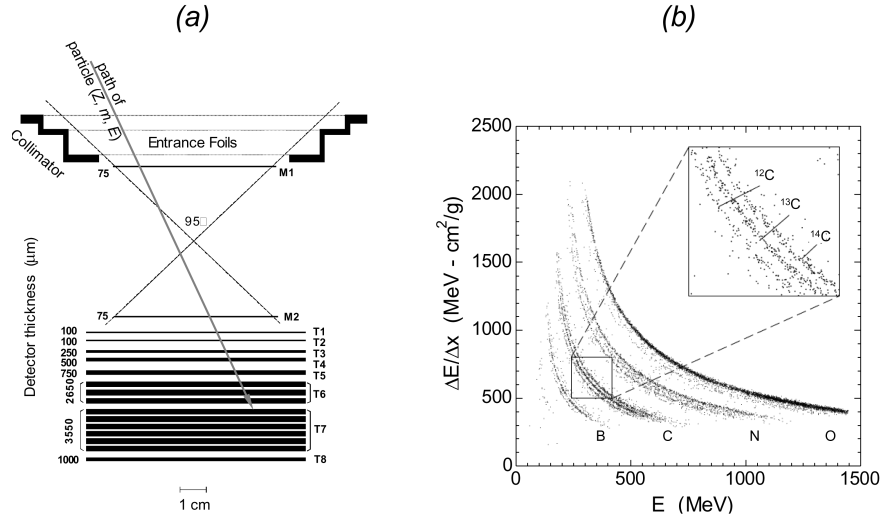

Fig. 3.22. (a) Schematic cross section of the Solar Isotope Spectrometer (SIS). (b) Illustration of the $\mathrm{d}E/\mathrm{d}x$ by E analysis technique using data acquired during an accelerator calibration of SIS.

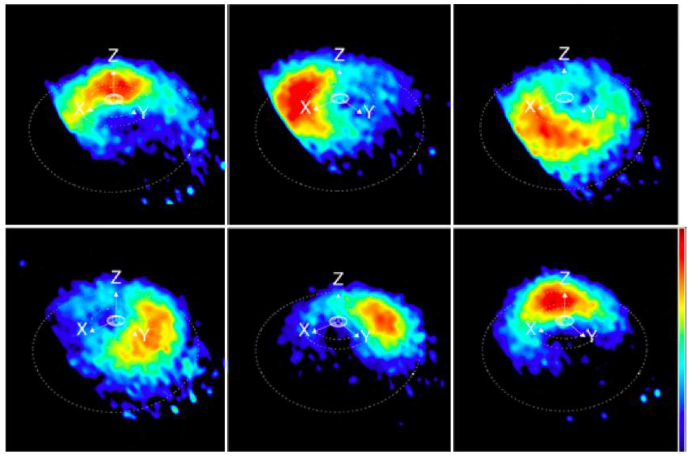

Fig. 3.23. Neutral-hydrogen ($20-50\,\mathrm{keV}$) images of Saturn's ring current taken with the INCA sensor on Cassini at 2.13 hour intervals showing counterclockwise rotation of the plasma. (Courtesy S. M. Krimigis)

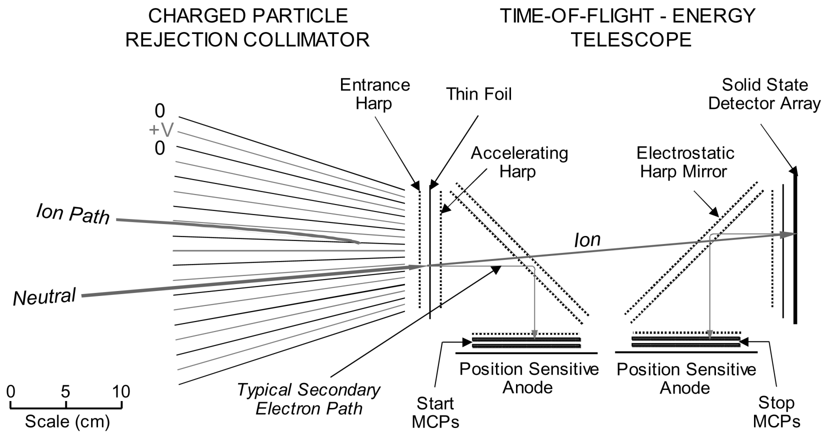

Fig. 3.24. Schematic cross section of a high-energy energetic neutral atom (ENA) composition spectrometer. (from Stone et al., 1998))

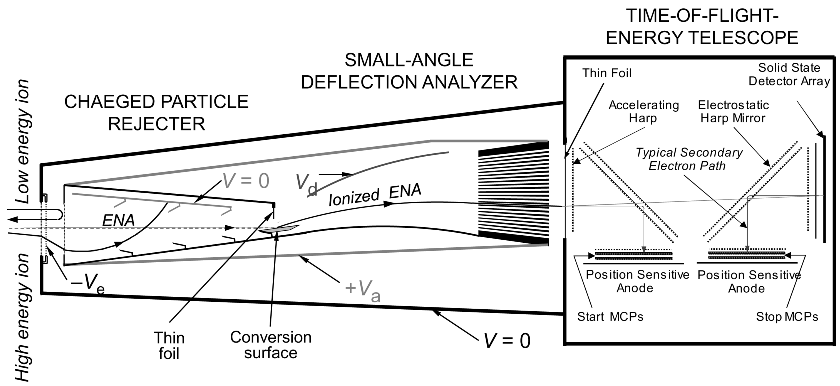

Fig. 3.25. Schematic cross section a low-energy ENA composition spectrometer. The Charged Particle Rejecter and the Small-angle Analyzer are at high positive potential.

4

Radiative signatures of energetic particles

by Tim Bastian

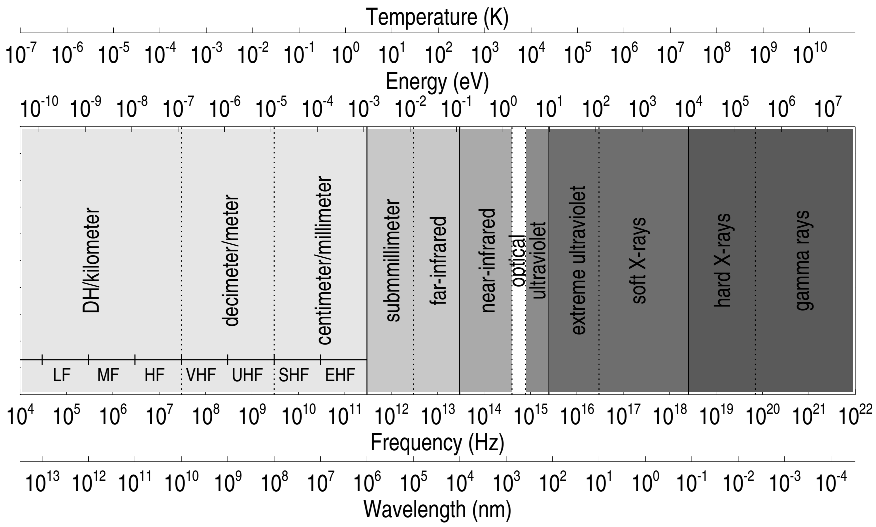

Fig. 4.1. Overview of the electromagnetic spectrum with energy in electron volts and the equivalent temperature in Kelvin (top axes), frequency in Hertz, and wavelength in nanometers (bottom axes). Note that the AM band lies in the low- and medium-frequency (LF-MF) range and the FM band in the very-high frequency (VHF) range.

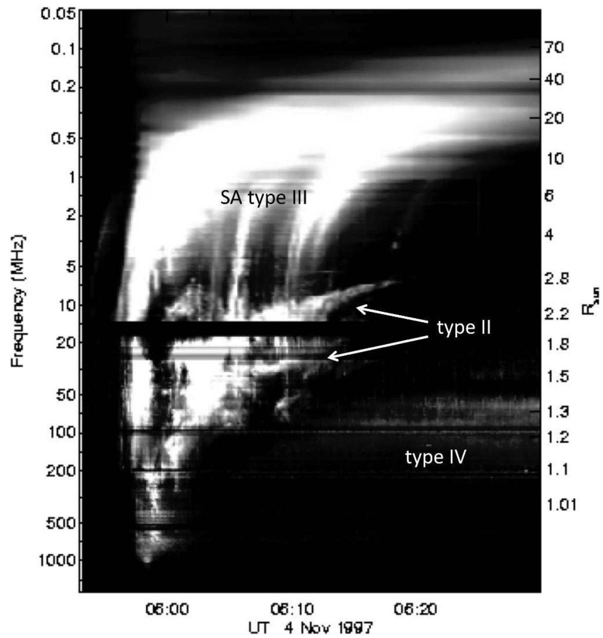

Fig. 4.2. An example of a dynamic radio spectrum formed from the Culgoora spectrographs on the ground and the WIND/WAVES spectrographs from space. The spectrum shows radio emission from a radial range spanning the low corona to ≈ 70 $R_{\odot}$. The spectrum shows the presence of interplanetary type III radio bursts (see Table 4.1 for descriptive definitions of radio burst types I–IV), coronal type II radio burst, and so-called "shock-associated" (SA) type III radio bursts. (After Dulk et al., 2000.)

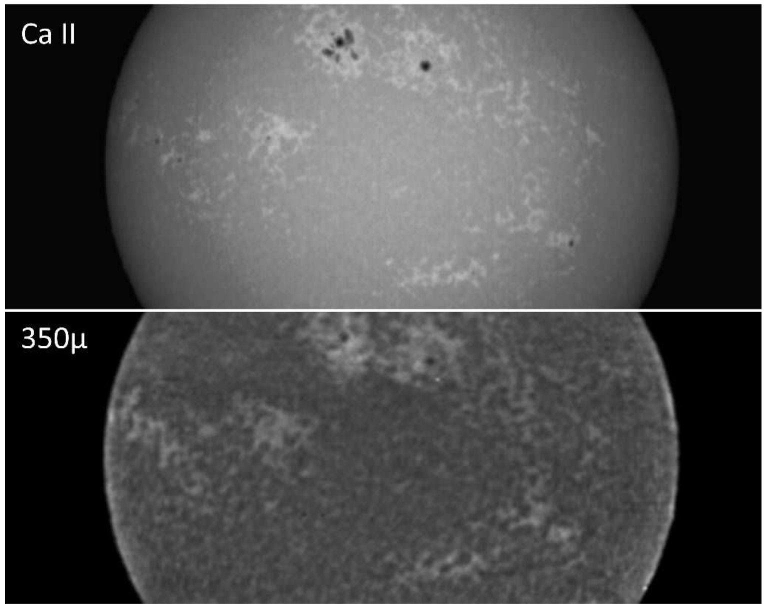

Fig. 4.3. *Top*: chromospheric emission in the Ca II K line at 393.2 nm. *Bottom*: the corresponding image at a wavelength of 350μ (850 GHz). This image was obtained by Lindsey et al. (1995) using the JCMT on 9 Feb 1991.

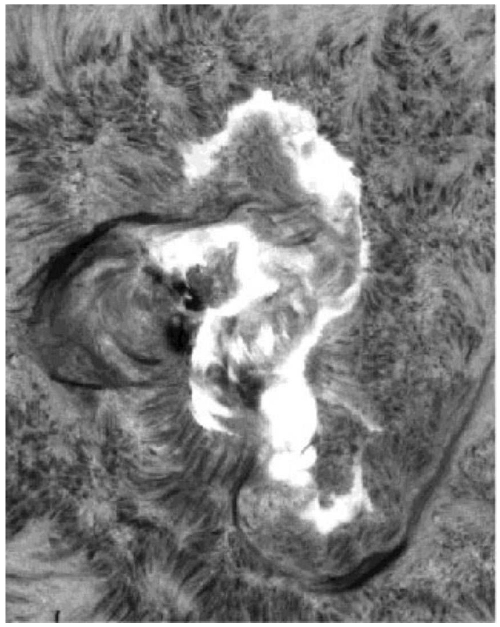

Fig. 4.4. A two-ribbon solar flare in the chromospheric Hα line at 656.28 nm.

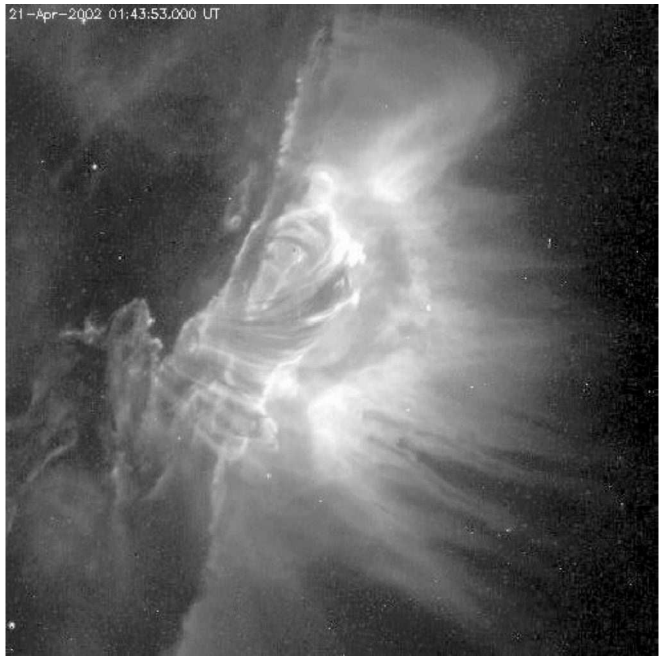

Fig. 4.5. A TRACE observation of the 171Å, or 17.1 nm, EUV emission from the X1.5 solar flare (see Table 5.1 for the flare magnitude scale) on 21 April 2002. From Gallagher et al. 2002.

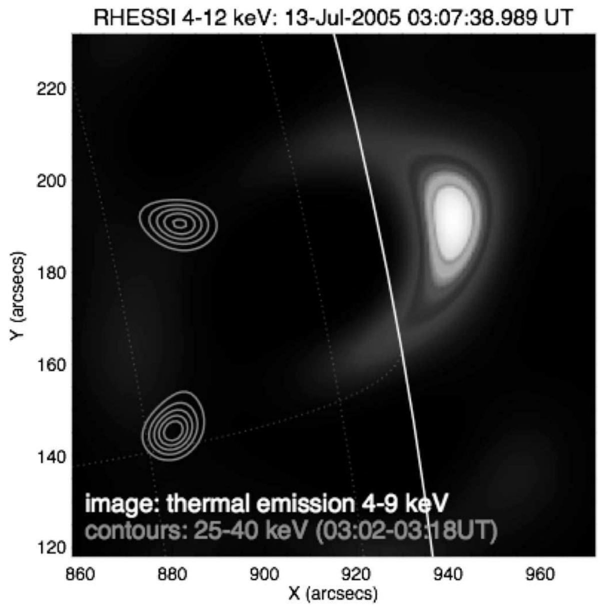

Fig. 4.6. An example of hard X-ray emissions from a solar flare from $4-9\,\mathrm{keV}$ (background image) and $25-40\,\mathrm{keV}$ (gray contours) by the RHESSI satellite. From Bastian et al. 2008

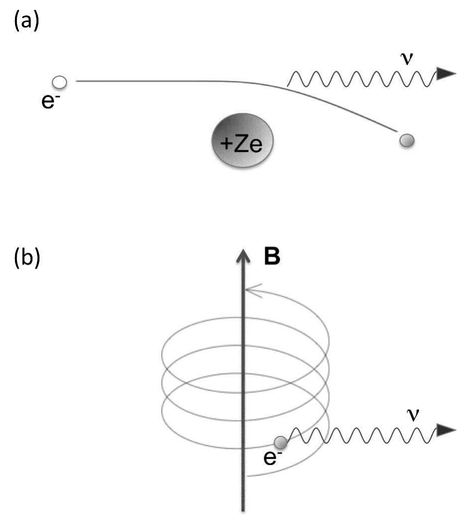

Fig. 4.7. (a) Schematic illustration of bremsstrahlung, or free-free, emission resulting from the collision of an electron with an ion; (b) schematic illustration of gyromagnetic emission resulting from the gyration of an electron in a magnetic field.

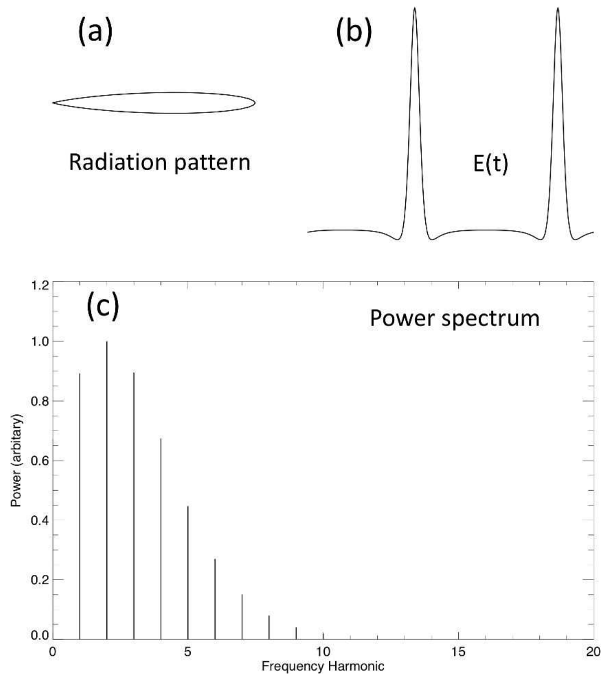

Fig. 4.8. (a) Schematic illustration of the radiation pattern of a mildly relativistic electron ($\gamma \sim 2$) gyrating in a magnetic field. The radiation is strongly beamed along the instantaneous velocity vector; (b) the time variation of the electric field measured by a distant observer; (c) the power spectrum of the free-free, emission resulting from the collision of an electron with an ion; (b) schematic illustration of gyromagnetic emission resulting from the gyration of an electron in a magnetic field.

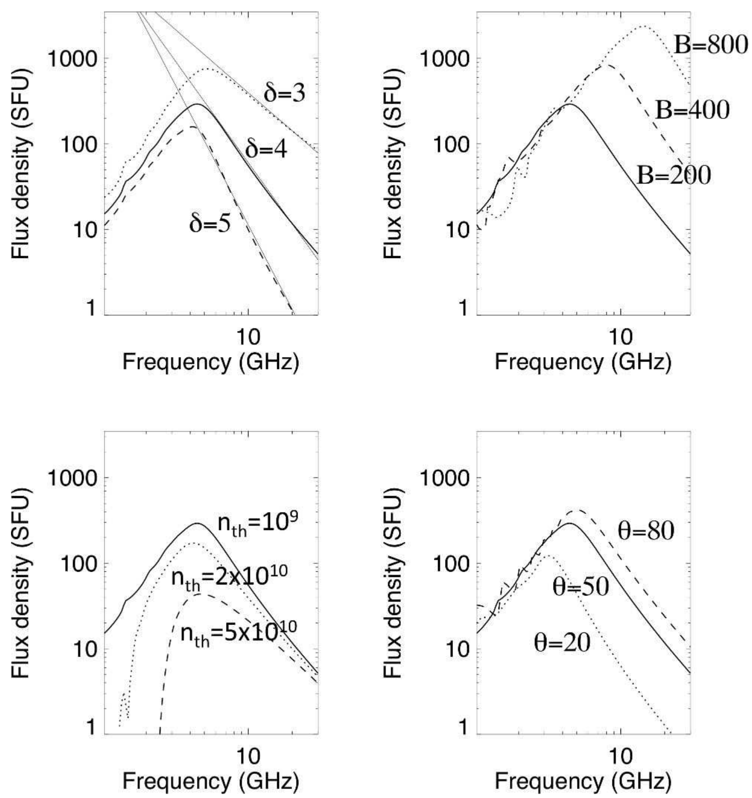

Fig. 4.9. The flux density spectrum of gyrosynchrotron emission from a power law distribution of electrons in an ambient thermal plasma. The source area and depth are held constant at 3×10^{18} cm^2 and 10^9 cm, respectively. The solid line represents the same reference spectrum in all panels, where the magnetic field is $B = 200$ G, the low-energy cutoff is $E_c = 100\,$keV, the spectral index is $\delta = 4$, the thermal number density is $n_{th} = 10^9$ cm^{-3}, and the number density of electrons with $E > E_c$ is $n_{rl} = 10^5$ cm^{-3}. Specific parameters are allowed to vary in panels (a-d) as shown.

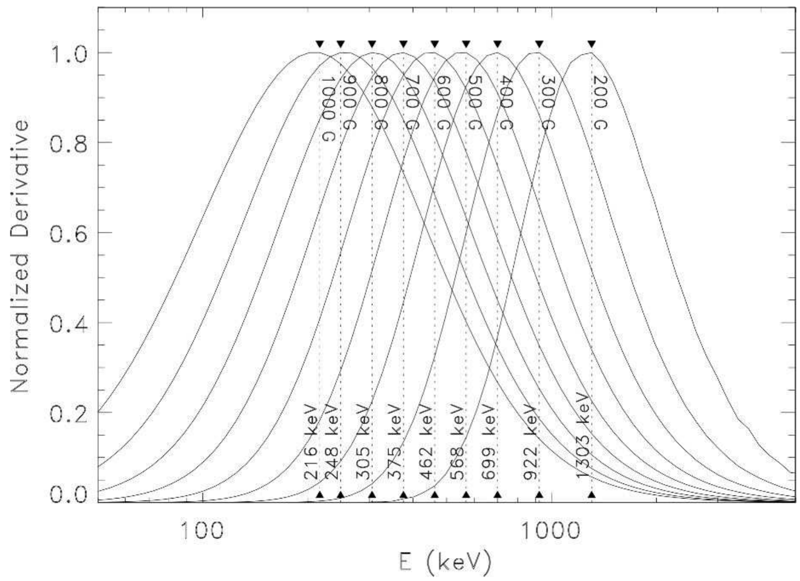

Fig. 4.10. The contribution function of a power law distribution of electrons to gyrosynchrotron radiation at a fixed frequency of 17 GHz for values of the magnetic field varying from 200 G to 1000 G.

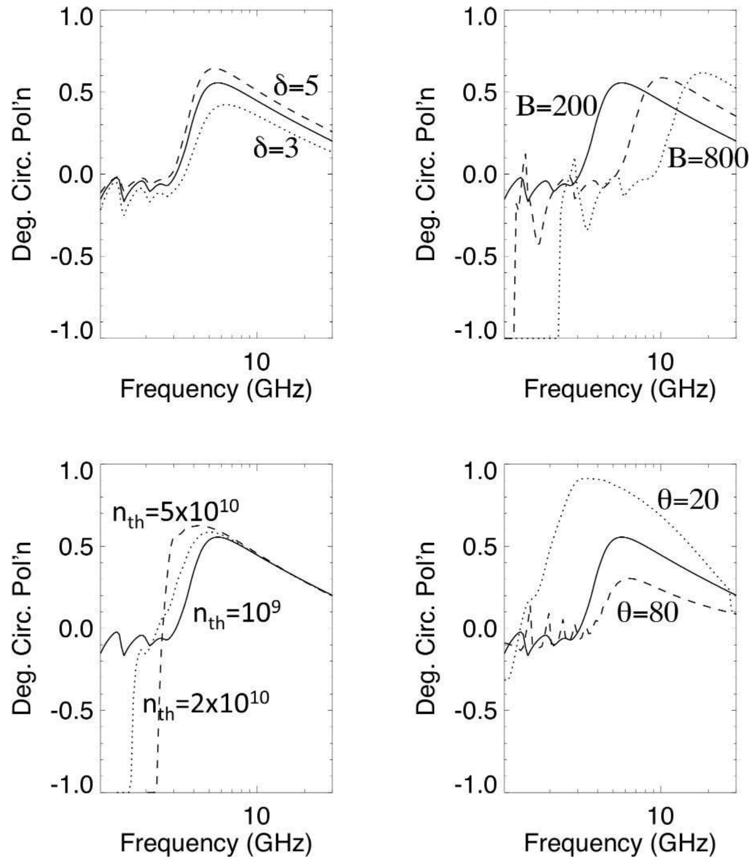

Fig. 4.11. The degree of polarization (Stokes I/V) for the cases shown in Fig. 4.9.

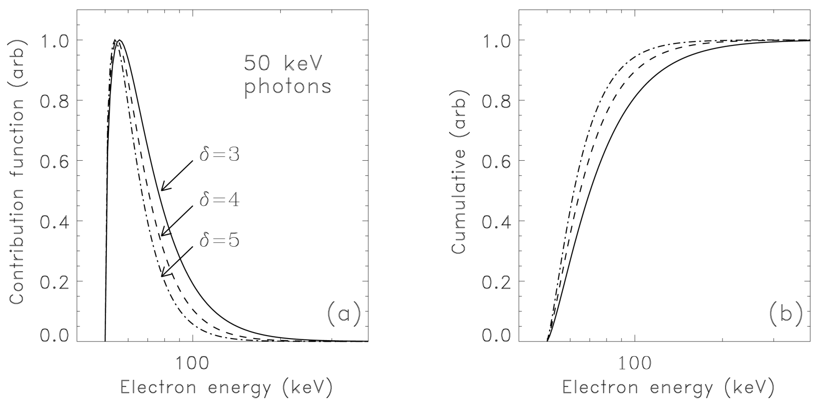

Fig. 4.12. (a) Normalized contribution function of a power-law distribution of electrons to 50 keV hard X-ray *thin*-target photon emission for spectral indices $\delta = 3, 4$ and 5. (b) The normalized cumulative energy distribution function for the same.

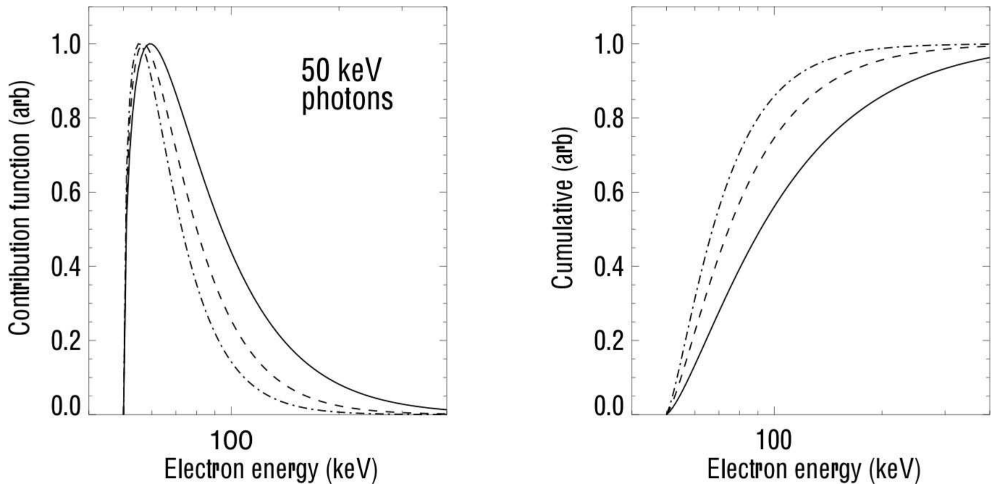

Fig. 4.13. (a) Normalized contribution function of a power-law distribution of electrons to 50 keV hard X-ray *thick*-target photon emission for spectral indices $\delta = 3, 4$, and 5. (b) The normalized cumulative energy distribution function for the same.

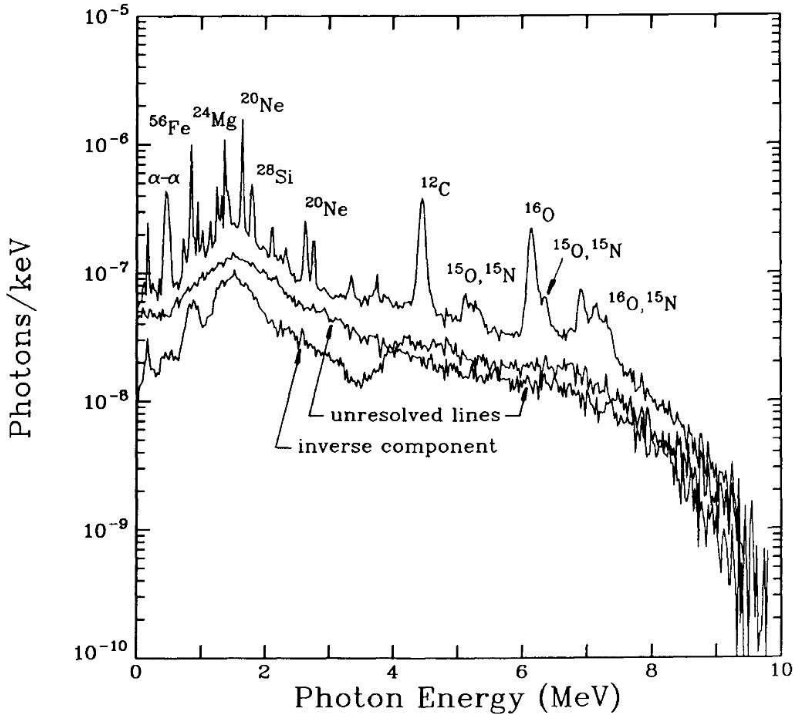

Fig. 4.14. A theoretical spectrum of nuclear de-excitation emission showing the prominent narrow line emission and components corresponding to unresolved lines and broad lines emitted by heavy ions colliding with the target medium. From Murphy et al. (1990).

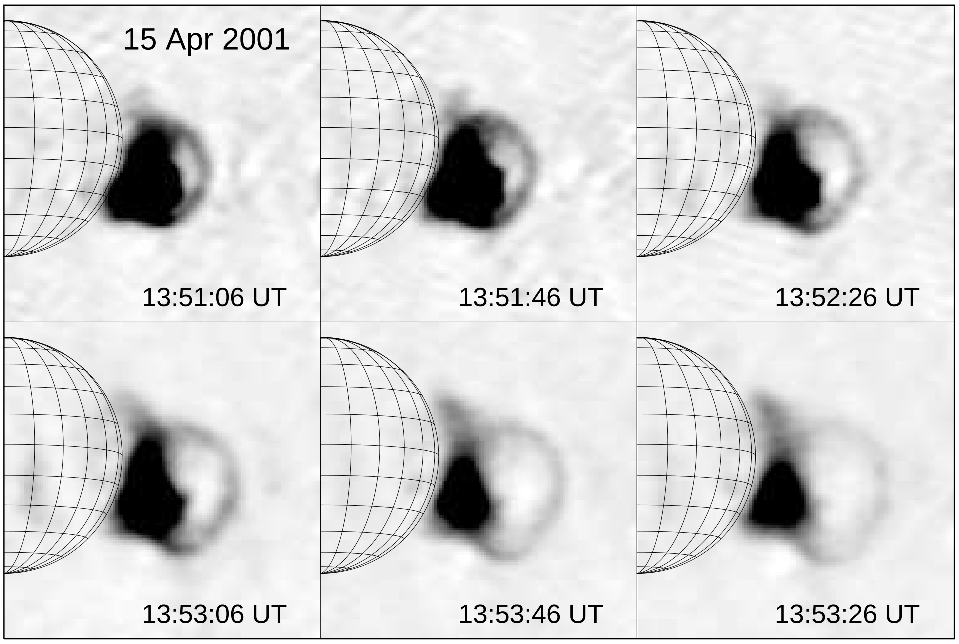

Fig. 4.15. A sequence of images of the fast CME of 15 April 2001 made by the NRH at a frequency of 421 MHz. After Maia et al. 2007.

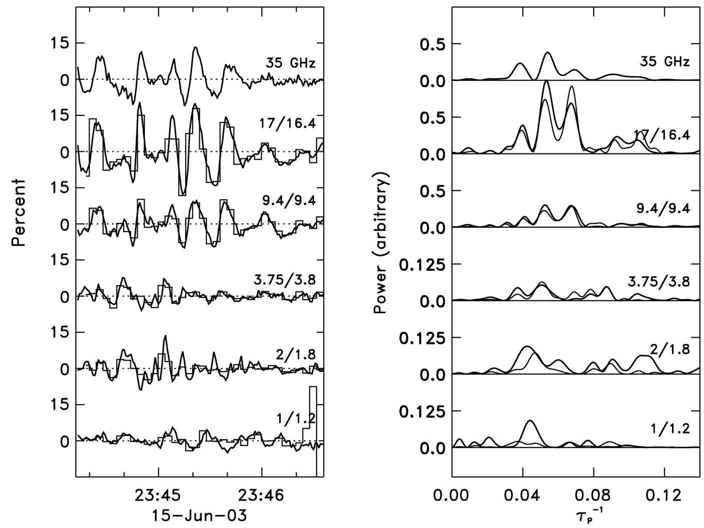

Fig. 4.16. A comparison of quasi-periodic oscillations observed in 17 GHz and hard X-ray radiation in various energy bands. The radio and hard X-ray emissions are correlated, in agreement with expectations for a model in which the electron acceleration and injection is modulated. A model wherein the oscillations result from MHD oscillations in a magnetic loop would yield an anti-correlation between the radio and hard X-ray emissions. From Fleishman et al. (2008).

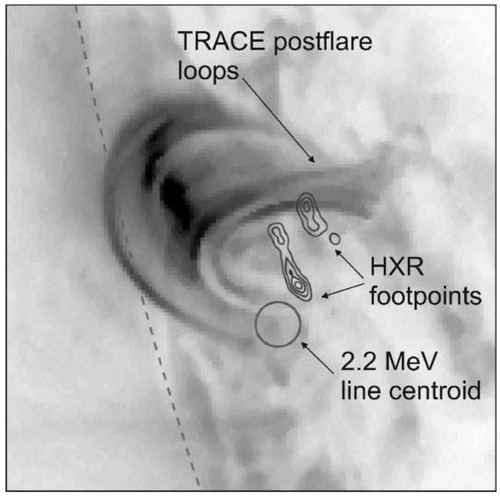

Fig. 4.17. Energetic emissions from the X4.8 flare on 23 July 2002. The 2.223 MeV neutron capture line and the 50-100 keV hard X-ray emission is compared with the EUV loops observed by TRACE (background negative image). From Brown et al. (2006), based on results from Hurford et al. (2003).

5

Observations of solar and stellar eruptions, flares, and jets

by Hugh Hudson

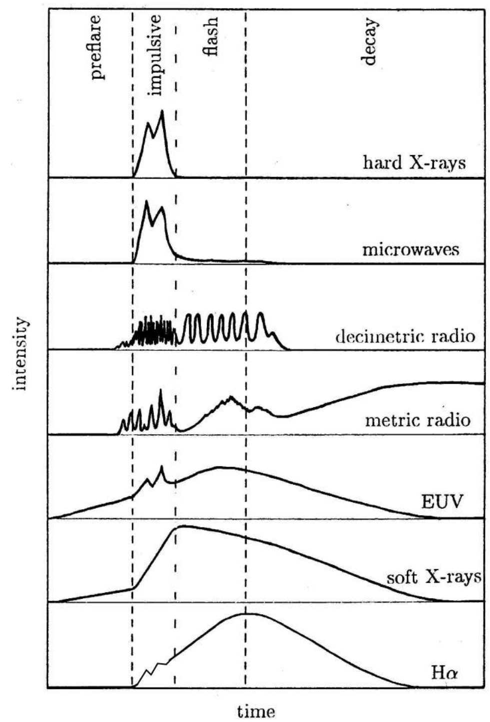

Fig. 5.1. Schematic view of the evolution of flare emissions in different wavelengths, showing the intermingling of impulsive-phase and gradual-phase signatures across the spectrum (from Benz, 2002). Note the wide variety of radio signatures.

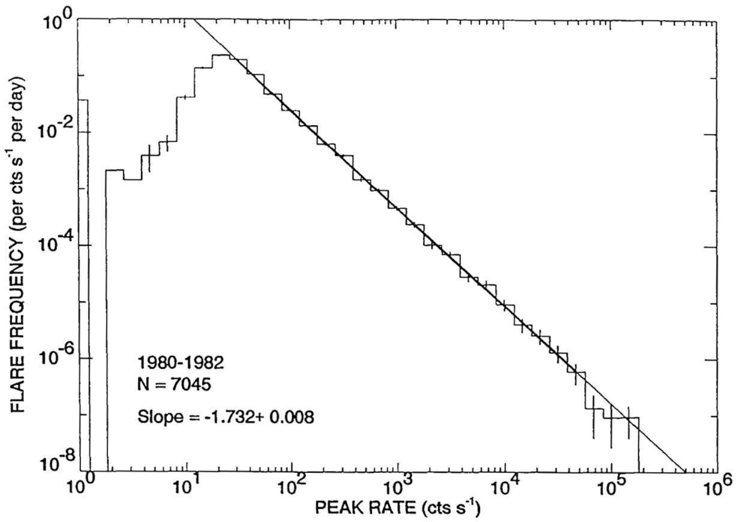

Fig. 5.2. Distribution of peak counting rates of 7,045 hard X-ray bursts observed over 1980-1982 by the HXRBS instrument on board the Solar Maximum Mission (Crosby et al., 1993). Note the fidelity of the power law, down to a low-rate rolloff due to selection effects; also note the lack of a high-rate rolloff in this range of observations.

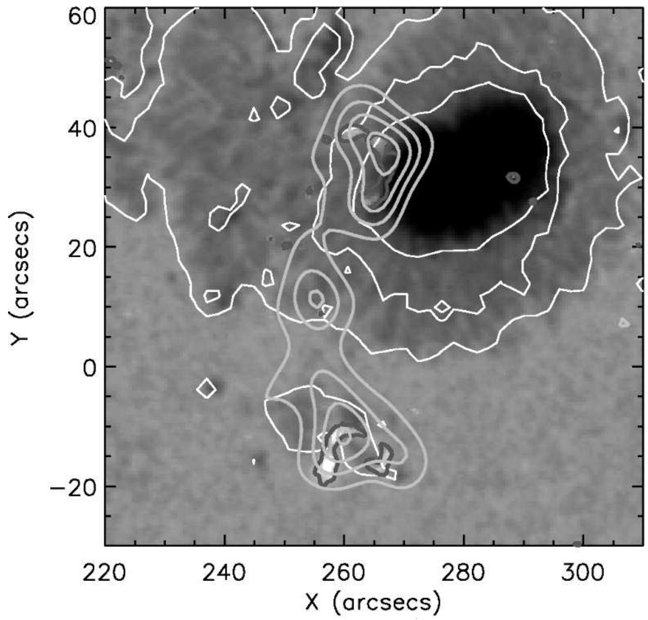

Fig. 5.3. TRACE white light (dark grey contours) and RHESSI hard X-ray (light grey contours; 25-50 keV) observations of a flare of 2002 July 24 (Fletcher et al., 2007). Note the extremely compact (arc sec), and temporally unresolved (∼10 s), white-light patches in the north and south footpoint regions. The RHESSI source in between the footpoint regions is not associated with the white-light emission.

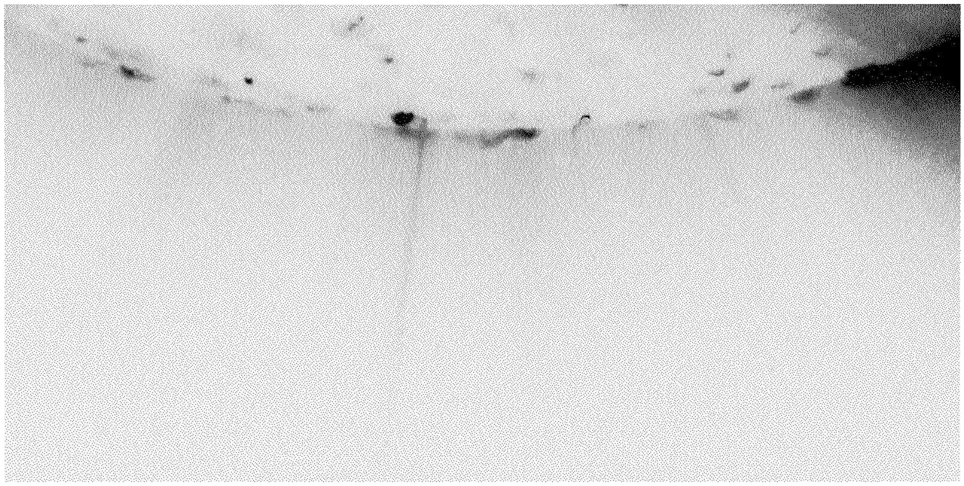

Fig. 5.4. Soft X-ray image of the Sun's south polar region, with an inverted grey scale, showing a highly collimated polar jet structure (Courtesy P. Grigis). Note that this is a coronal-hole jet, but that similar features often occur in active regions in association with microflares (see Section 5.2.5).

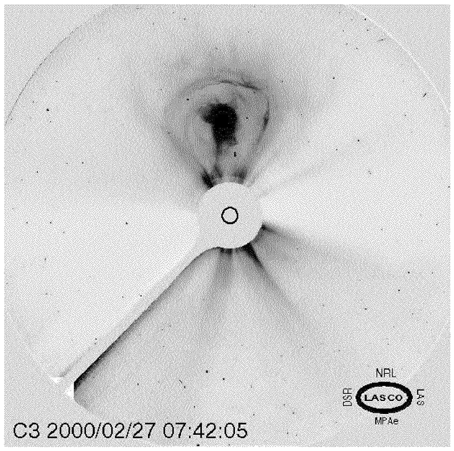

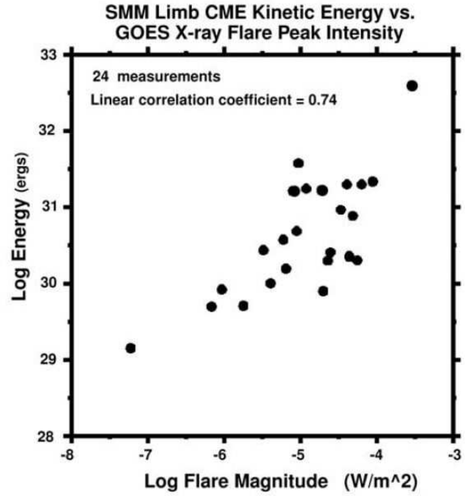

Fig. 5.5. *Left:* Coronagraph observation of a CME that nicely shows the three-part structure: front, cavity, and (the bright core) filament (this is a file image taken from the LASCO database, presented in a reverse grey scale). *Right:* Correlation between inferred CME kinetic energy and peak GOES soft X-ray flux (Burkepile et al., 2004).

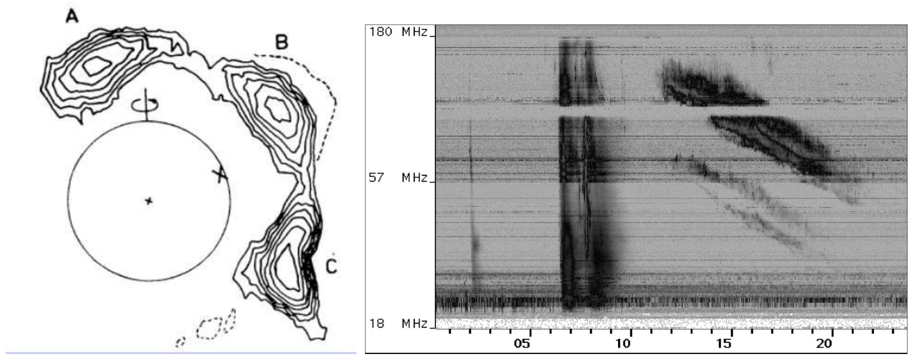

Fig. 5.6. *Left:* Culgoora image of a type II burst associated with a major flare (Palmer & Smerd, 1972). Note how this plasma-frequency radiation appears to wrap around a concentric spherical surface, presumably at the right mean density. *Right:* Radio spectrogram (frequency versus time in minutes) of a different major flare, illustrating type III bursts (fast drift, produced by streams of energetic electrons) and a type II burst (slow drift, fundamental/harmonic structure produced during the propagation of a large-scale shock wave), also from Culgoora.

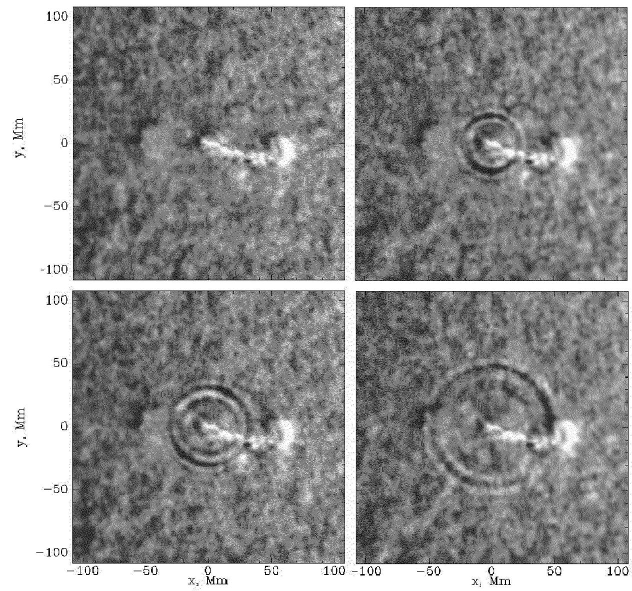

Fig. 5.7. The original helioseismic wave observed from the singular solar-minimum flare of 1996 July 7 (Kosovichev & Zharkova, 1998), from the "last best active region" of that solar cycle (Hudson et al., 1995). The figure shows an amplified wave via Doppler images, with the wave representation based on the observed Fourier components. More recent helioseismic waves are directly visible in the filtered images.

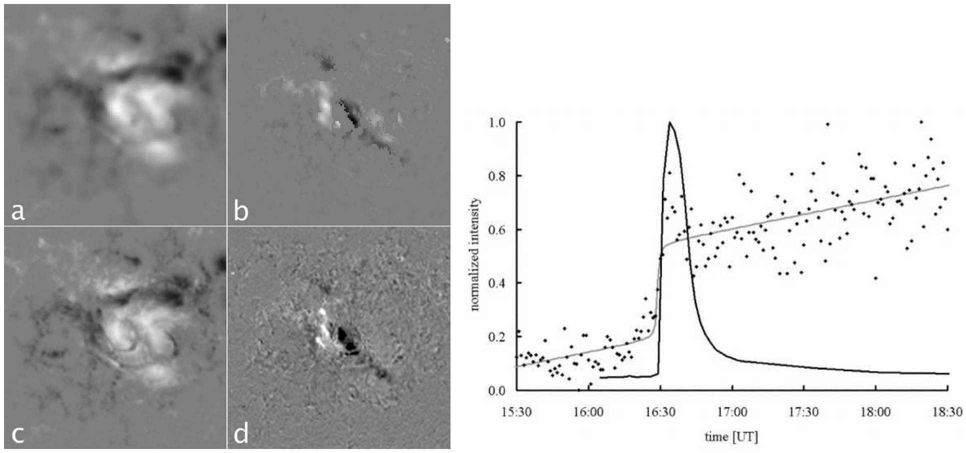

Fig. 5.8. *Left:* Map of the stepwise photospheric field changes in the flare of 2003 October 29. Panels (a) and (c) show the GONG and MDI magnetograms; panels (b) and (d) show their before/after changes, respectively. *Right:* Time variations for the flare of 2001 August 25, showing the GOES light curve as a smooth line and the GONG data as points. The fluctuations are large and there is a background trend, as in many events, but the stepwise change is clear. It (typically) coincides with the impulsive phase of the flare. Both illustrations taken from Sudol & Harvey (2005).

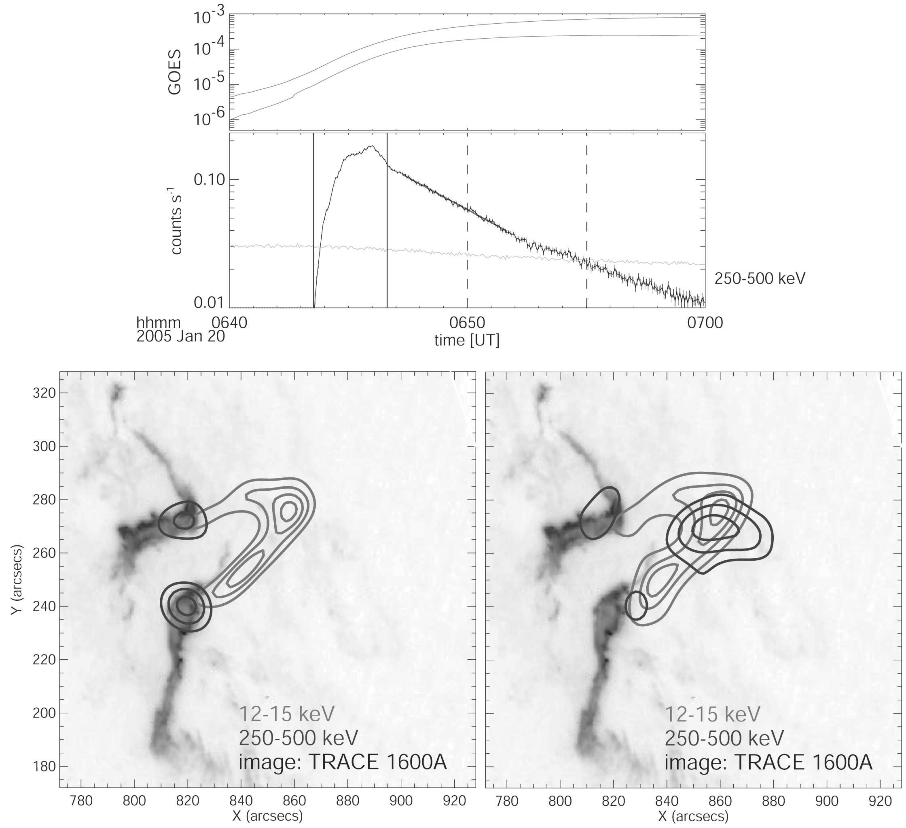

Fig. 5.9. Hard X-ray sources from the 2005 January 20 event. *Upper:* GOES and RHESSI light curves. *Lower:* Early image showing well-developed footpoints at 250-500 keV (dark contours), and a later image showing the persistent coronal hard X-ray coronal source. The light contours show large-scale loop structures with thermal spectra.

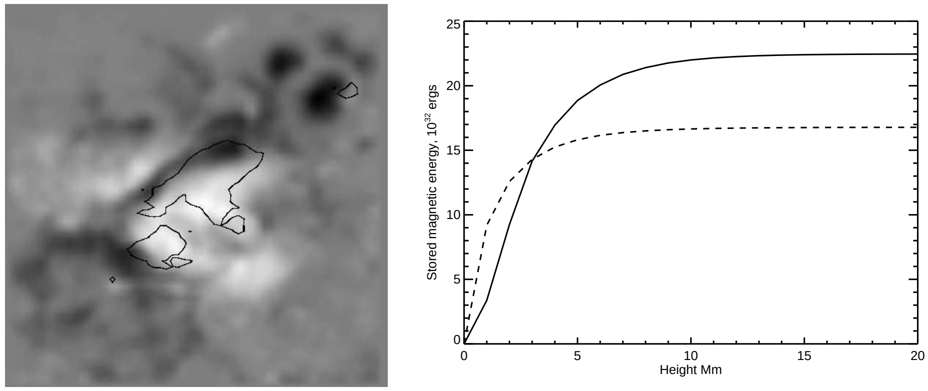

Fig. 5.10. The stored magnetic energy in a nonlinear force-free field extrapolation for Active Region 10486 computed by J. McTiernan using the technique of Wheatland et al. (2000). *Left:* The B_z component of a chromospheric vector magnetogram for Active Region 10486, 2004 October 29 18:46 UT. The contour shows the 50% level of the excess over the energy content of the corresponding potential field, at an altitude of 6 Mm. *Right:* Increase of total energy with height in the data cube of the extrapolation (dimension 65^3 arcsec). The dashed and solid lines show the integrated energies for a potential field model and for the non-potential field model, respectively. The 50% level gives a rough idea about the location of stored magnetic energy; it is higher for the non-potential field but still located close to the base of the corona.

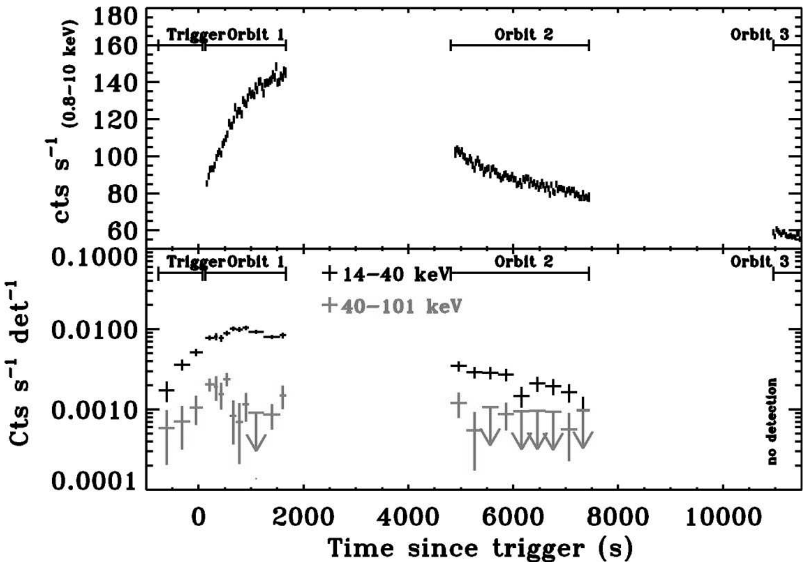

Fig. 5.11. Powerful stellar flare observed 2005 December 16 on the active binary system II Pegasi (Osten et al., 2007). The upper curve shows 0.8-10 keV counting rate from the XRT instrument on board SWIFT (Burrows et al., 2005), and the lower curves show two hard X-ray channels (14-40 keV and 40-101 keV) from the BAT instrument. One can see the clear progression of a Neupert-effect analogy, with the highest-energy channel (lighter shading) showing an impulsive-phase excess in the first ksec of the observation.

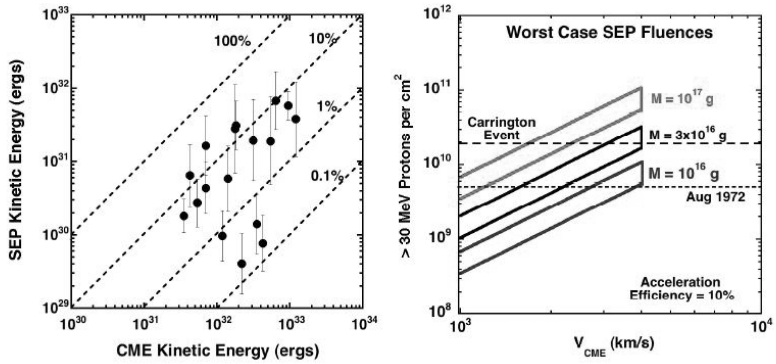

Fig. 5.12. *Left:* Energy converted by interplanetary (CME-driven) shock waves into solar energetic particles (SEPs). The efficiency of conversion can exceed 10%. *Right:* Comparison of particle fluences for model CME masses and speeds, relating the Carrington event to better-observed recent examples (Mewaldt et al., 2007).

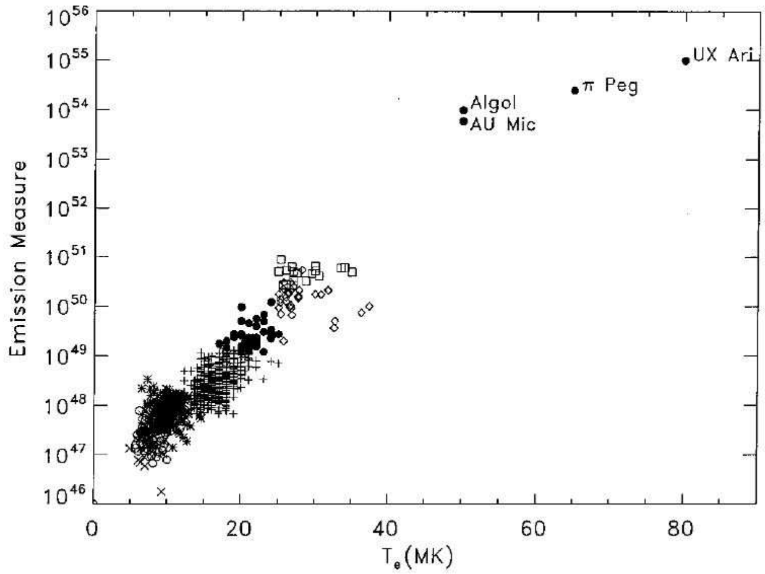

Fig. 5.13. Correlation of temperature and emission measure for solar and stellar flares. The various symbols refer to the original publications, as identified in the paper by Feldman et al. (1995) from which this figure is taken.

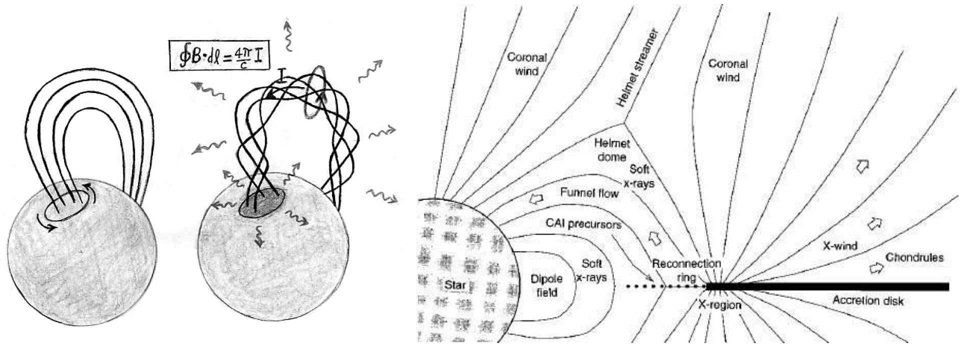

Fig. 5.14. *Left:* Cartoon showing energy storage in the "corona" of a magnetar, a neutron star magnetized to $\sim 10^{15}$ G and capable of giant flares (Duncan, 2005; Duncan et al., 2005). *Right* Cartoon showing "X-wind" model of magnetic fields involved in the accretion of matter onto a young star (Shu et al., 1997).

Fig. 5.15. Mapping of separatrices to the photosphere (heavy lines) compared with hard X-ray footpoint locations (crosses) for the flare of 2001 August 25 (Metcalf et al. 2003), also the subect of Fig. 5.8b. The image dimensions are 120 × 150 arc sec in x and y, respectively. The main flare ribbons are at the upper part of the figure, but note how faithfully the remote brightenings follow the projected separatrix at the bottom of the figure as well.

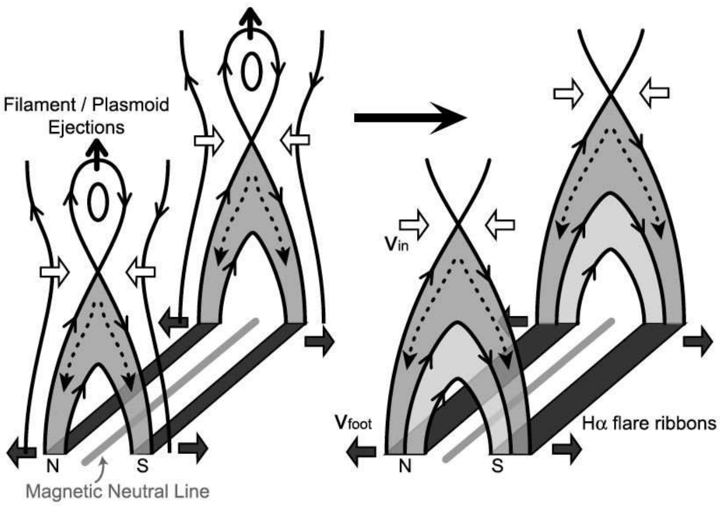

Fig. 5.16. How the ribbon motion sweeps out magnetic field during the reconnection process in the standard model (from Asai et al., 2004a; cf., Fig. 6.10).

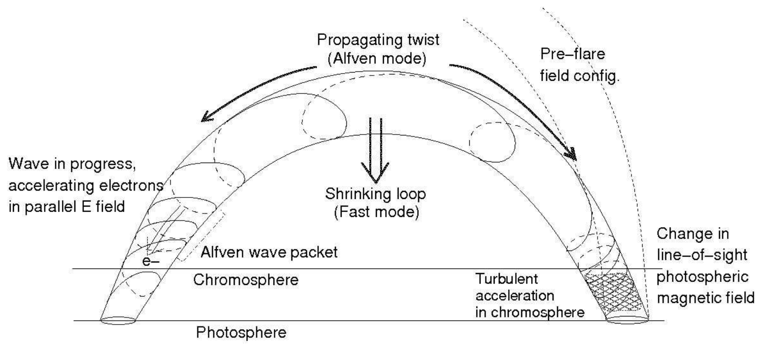

Fig. 5.17. Model put forth by Fletcher & Hudson (2008), showing the extraction of stored coronal magnetic energy via the Poynting flux of waves excited by the restructuring that produces the flare. Particle acceleration in this picture, as in other pictures, remains problematic.

6

Models of coronal mass ejections and flares

by Terry Forbes

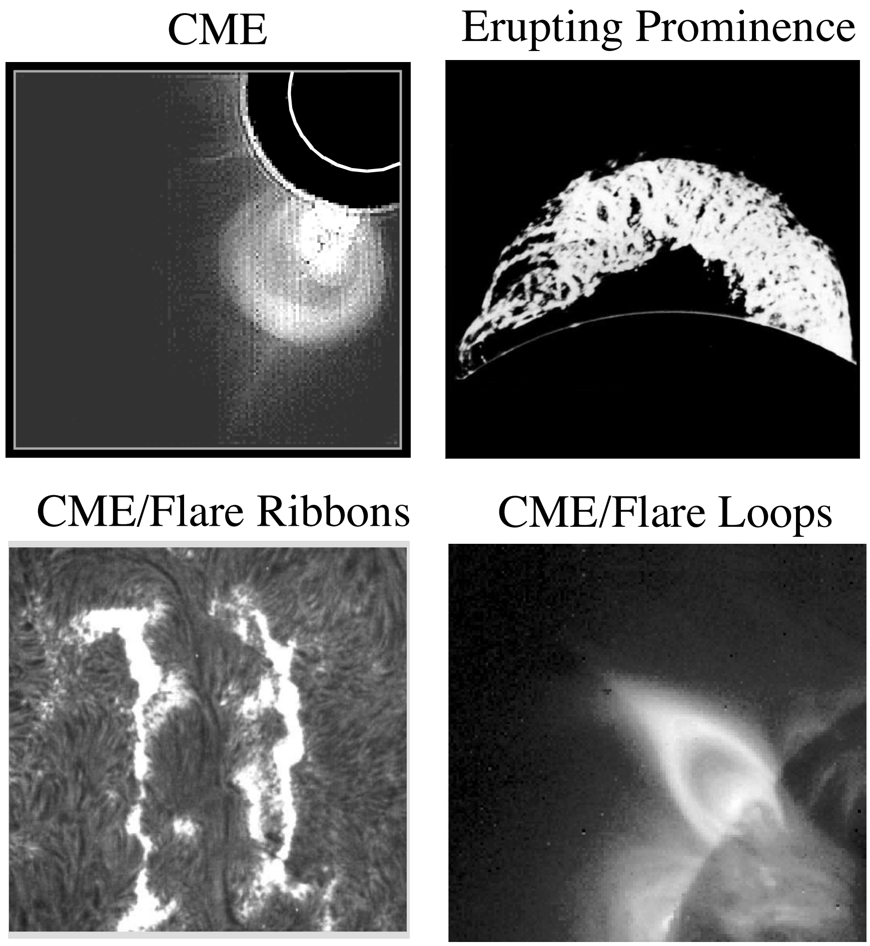

Fig. 6.1. Four different images of solar eruptions obtained by different types of telescopes. The upper left panel shows a coronagraph image from the Solar Maximum Mission satellite, while the upper right panel shows an Hα image of an eruption at the limb of the Sun (both images courtesy of the High Altitude Observatory). The lower left panel shows an Hα image of an eruption seen at disk center (courtesy of the Big Bear Solar Observatory), while the lower right panel shows a soft X-ray image of an eruption at the limb of the Sun (courtesy of the Institute of Space and Astronautical Sciences of Japan).

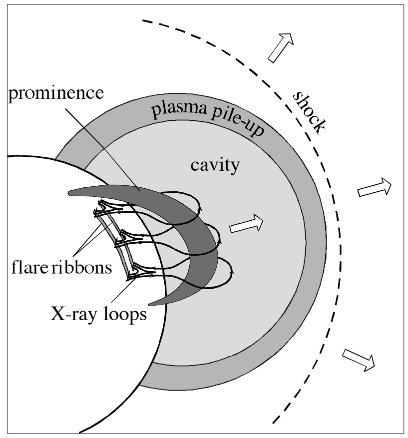

Fig. 6.2. Idealized diagram showing the relation between the flare ribbons, flare loops, the CME shock, the CME shell (plasma pile-up region), the CME cavity, and the filament contained within the cavity.

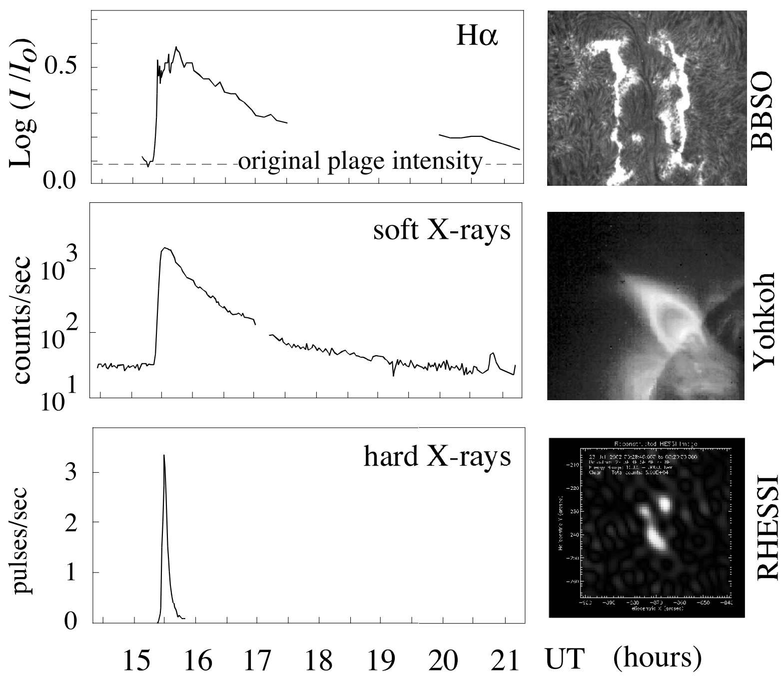

Fig. 6.3. *Top*: Hα (1.902 eV); middle: soft X-ray (1.0-6.3 keV); and bottom: hard X-ray (10-50 keV) emissions for the large, two-ribbon flare of 28 August 1966 (from Forbes 2003). The Hα light-curve data are from the McMath-Hulbert Observatory and show the logarithm of the intensity of one of the Hα ribbons in units of the undisturbed Hα background intensity (Dodson and Hedeman 1968). The soft X-ray data are from Explorer 33 (Van Allen and Krimigis, as published in Zirin and Lackner, 1969). The hard X-rays were measured by an ion chamber on the ATS-6 satellite (Arnoldy *et al.*, 1968). Also shown are images (for different events) of the flare features which give rise to these types of emissions.

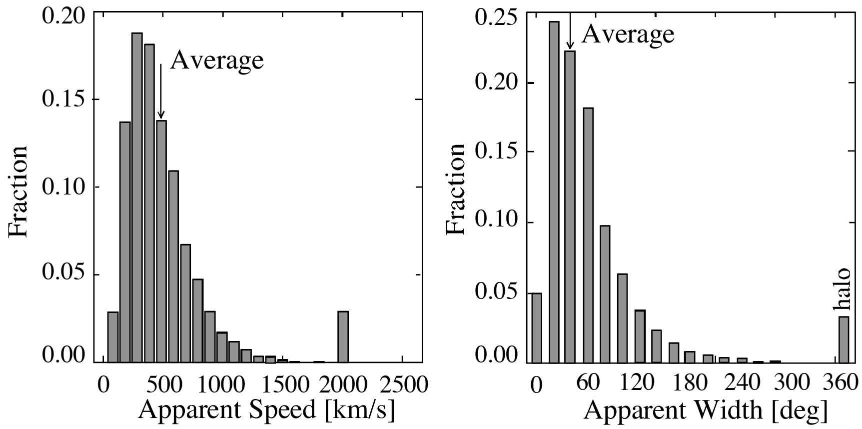

Fig. 6.4. Distribution of the apparent speeds (left panel) and widths (right panel) of CMEs observed by the SOHO coronagraph (LASCO) between 1996 and 2004. The bar in the right panel labeled "halo" refers to CMEs traveling directly toward or away from the Earth. For such events the apparent angular width tends to be near 360 degrees regardless of the actual angular width (from Schwenn *et al.* 2006).

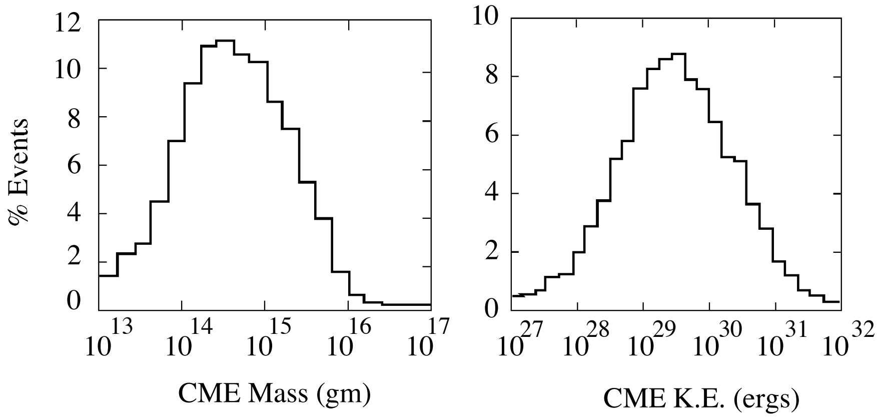

Fig. 6.5. Distribution of mass (left panel) and kinetic energy (right panel) of CMEs observed by the SOHO coronagraph (LASCO) between 1996 and 2004. The decrease in the number of events at low mass and energy is at least partly due to the difficulties encountered in observing small events (after Schwenn *et al.* 2006).

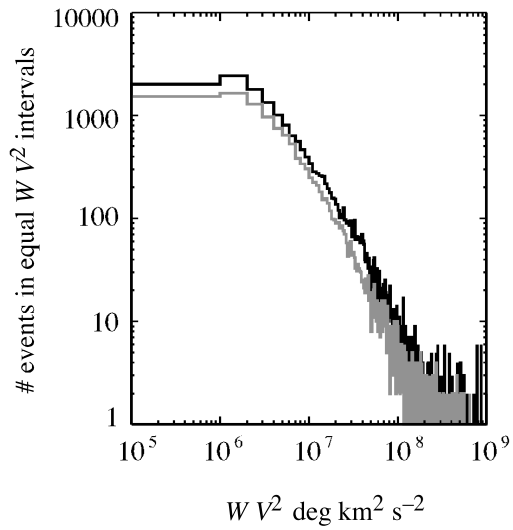

Fig. 6.6. Kinetic energy distribution of CMEs estimated by Yashiro*et al.* 2008 using the CME angular width, W, times the CME velocity, v, squared as a proxy. The black shaded region uses values obtained by hand from the SOHO (LASCO) data base, while the gray shaded region uses values from an automated process (CACTus) of the same data base. The approximately straight-line shape of the curve between 10^6 and 10^9 in $\log(Wv^2)$ implies a power-law distribution for CME kinetic energy (from Yashiro *et al.* 2008).

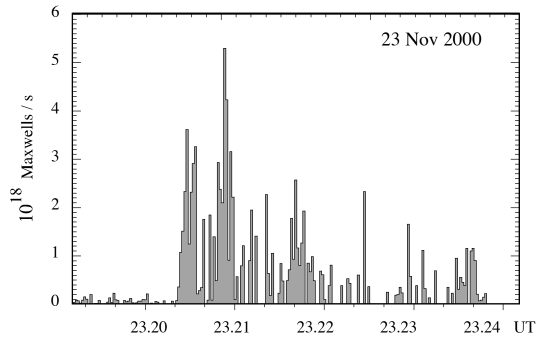

Fig. 6.7. Reconnection rate as a function of time for an M1 class flare observed on 23 November 2000. The rate is determined by calculating the rate at which the line-of-sight magnetic flux measured by the Michelson Doppler Interferometer on SOHO passes through the outer edges of the chromospheric flare ribbons observed by TRACE. A flux rate of 10^{18} Maxwells/s (gauss cm^2/s) corresponds to a potential drop of 10^{10} Volts (from Saba *et al.* (2006).

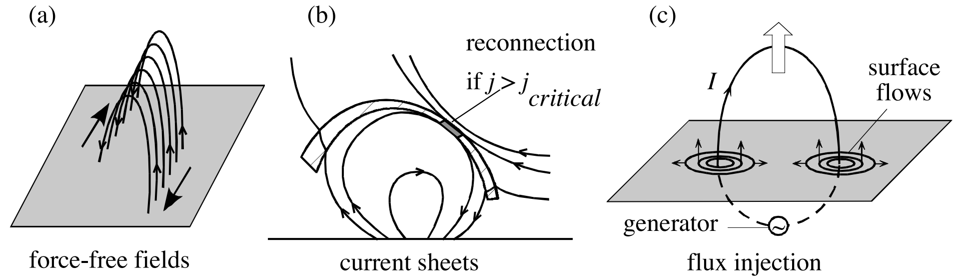

Fig. 6.8. Schematic illustration of three different types of models that use magnetic energy to power a flare or CME. Panel (a): Magnetic energy is stored in the corona in the form of field-aligned currents that eventually become unstable. Panel (b): Magnetic energy is stored in the corona in the form of a thin current sheet that is suddenly dissipated when a micro-instability is triggered within the sheet. Panel (c): An example of a directly driven flare model. Here magnetic flux is suddenly injected from the convection zone into the corona at the onset of the flare or CME. Such a model produces a well-organized flow pattern during the impulsive phase (small arrows at surface in panel *c*).

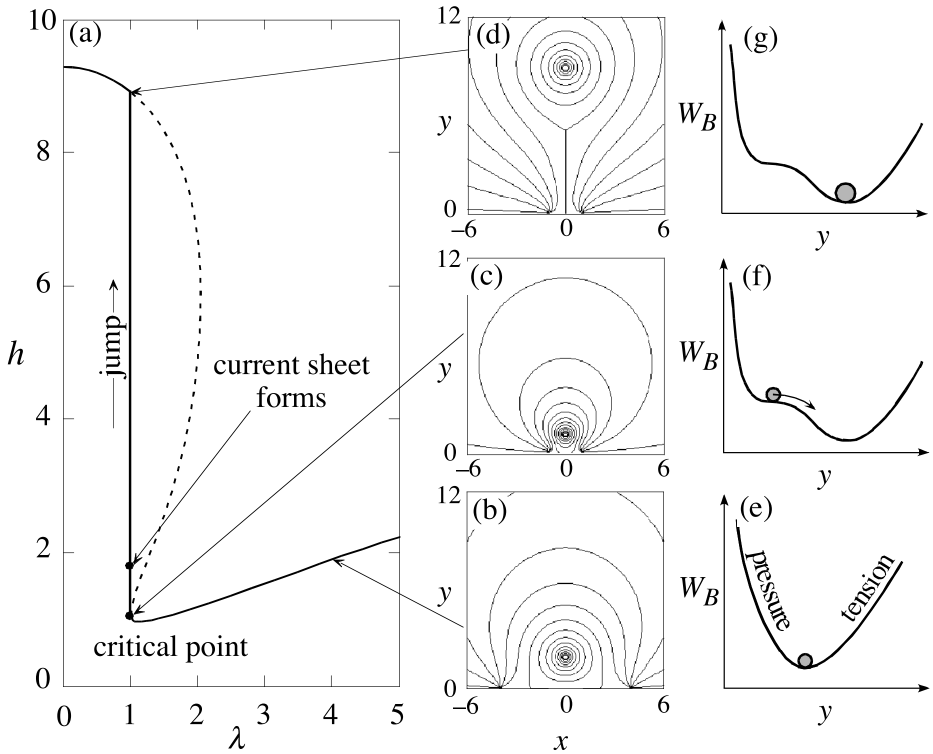

Fig. 6.9. Ideal-MHD evolution of a two-dimensional arcade containing a magnetic flux rope. Panel *a* shows the equilibrium curve for the flux rope height, h, in normalized units, as function of the source separation half-distance λ. Panels *b, c*, and *d* show the magnetic field configuration at three different locations on the equilibrium curve, and panels *e, f* and *g* show the corresponding energy schematic for each configuration. The case shown is for a flux rope radius of 0.1 in normalized units (after Forbes and Priest 1995).

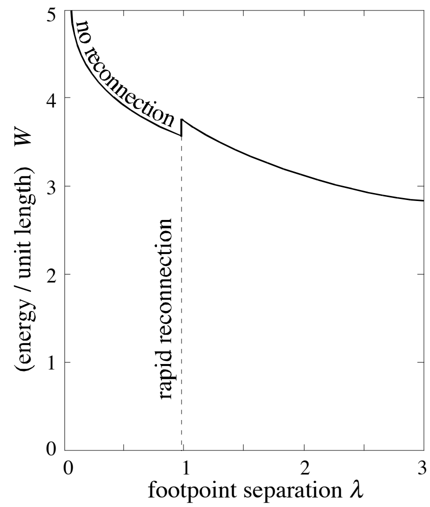

Fig. 6.10. Free magnetic energy released by the loss of equilibrium in the two-dimensional flux-rope model. The solid curve is the ideal-MHD case, and the dashed vertical line is the rapid-reconnection case.

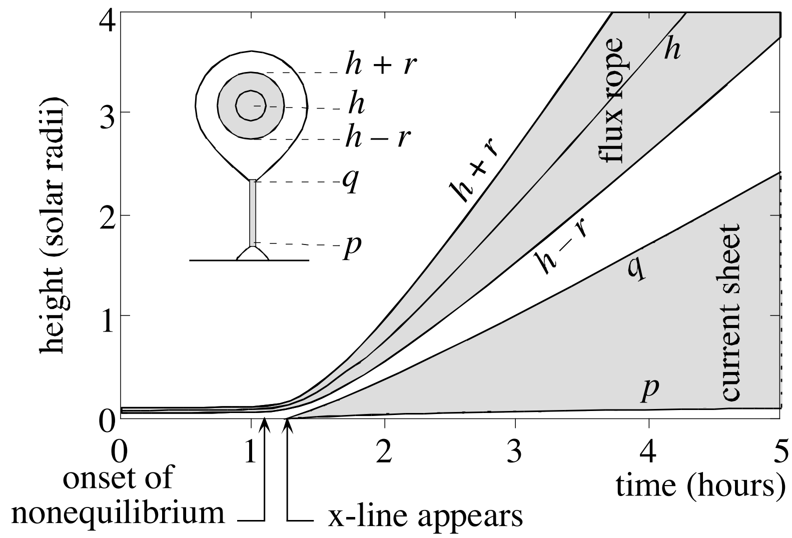

Fig. 6.11. Flux rope and current sheet trajectories obtained from the model in Fig. 6.10 by assuming a constant inflow Alfvén Mach number of 0.1 in the inflow region at the midpoint of the current sheet. The parameters h, r, q, and p are the flux rope's height and radius and the current sheet's upper and lower tips, respectively. The ambient Alfvén speed is calculated from the model magnetic field and the empirical coronal density model of Sittler and Guhathakurta (1999).

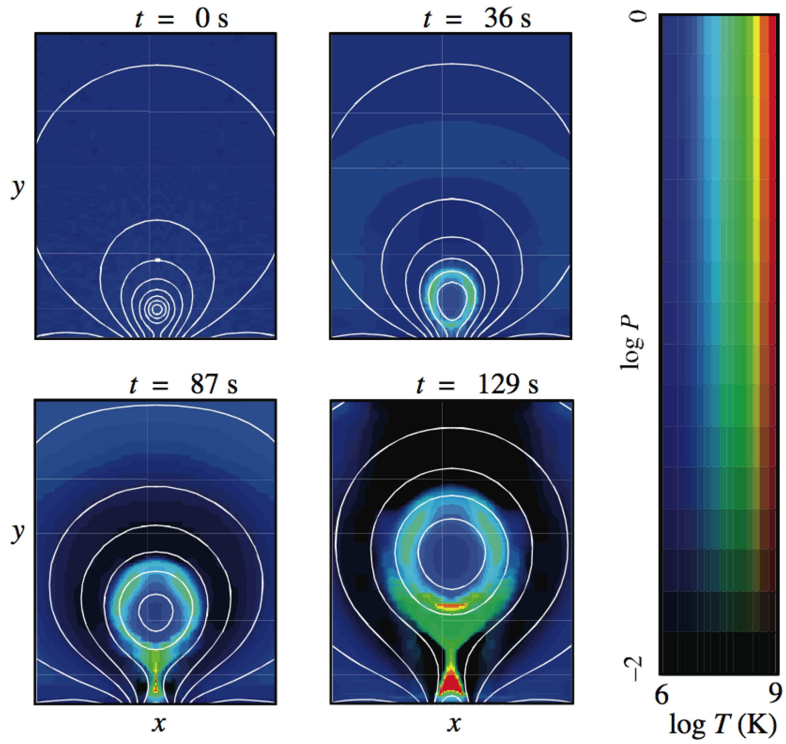

Fig. 6.12. Numerical simulation of an erupting flux rope. The color hue indicates the temperature, while the color intensity indicates the pressure. The white lines are contours of the flux function.

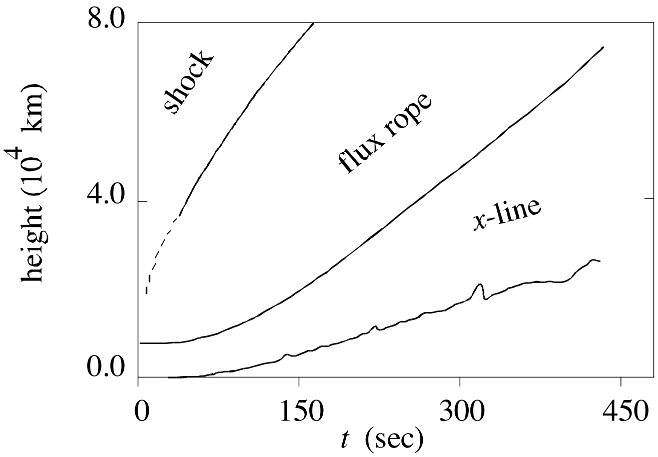

Fig. 6.13. The height of the shock, flux-rope, and x-line as a function of time for the numerical simulation shown in Fig. 6.12. The dashed line indicates the compressive wave that eventually steepens into the shock.

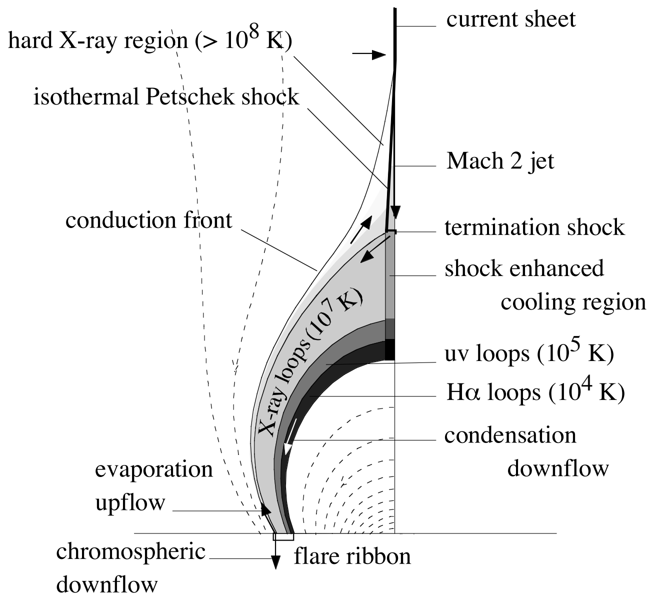

Fig. 6.14. Diagram of the temperature structure and flows predicted by a reconnection model of flare loops. Strong thermal conduction channels the energy released by reconnection to the chromosphere where it heats the plasma. The high pressure thereby created drives plasma upwards into the corona and downwards into the lower corona. (Compare with Fig. 5.16)

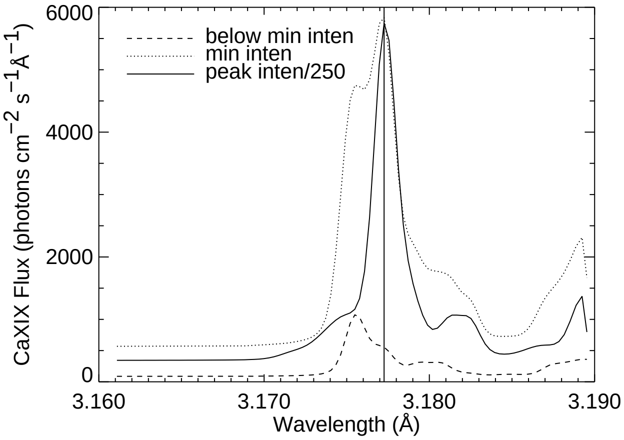

Fig. 6.15. The Ca XIX line profile predicted by the two-dimensional flux rope model for typical coronal values. Three different times are shown corresponding to the peak intensity (re-scaled solid line), an earlier time when the intensity would first be observed by the Yohkoh BCS (dotted line), and an even earlier time when the intensity would be too low to be observed (dashed line). The vertical line marks the rest wavelength of the resonance line (from Reeves *et al.* 2007).

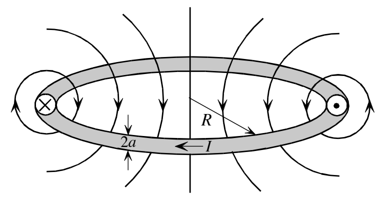

Fig. 6.16. An isolated toroidal flux rope. The flux rope has a major radius, R, a minor radius, a, and carries a net toroidal current I. The anti-parallel orientation of the current flowing on the opposite sides of the torus creates an outward force in the radial direction.

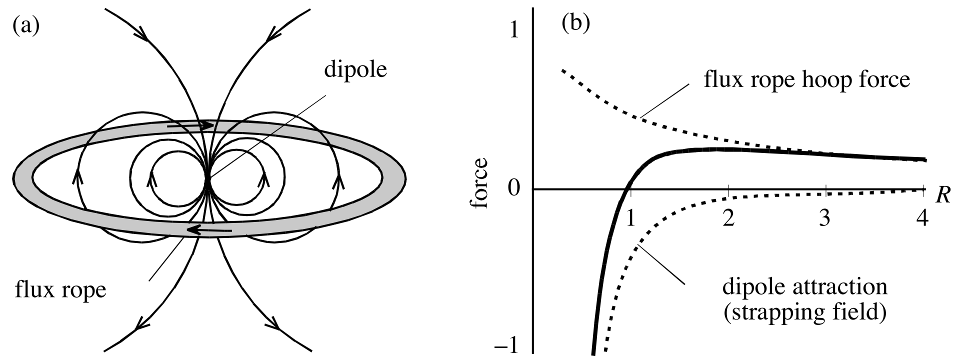

Fig. 6.17. An unstable toroidal equilibrium. (a) The outward force of the curved flux rope is balanced by a properly oriented dipole magnetic field. (b) Schematic diagram showing the forces acting on the flux rope as a function of radial distance. The single equilibrium that exists is unstable because displacements away from it produce forces that act to increase the displacement.

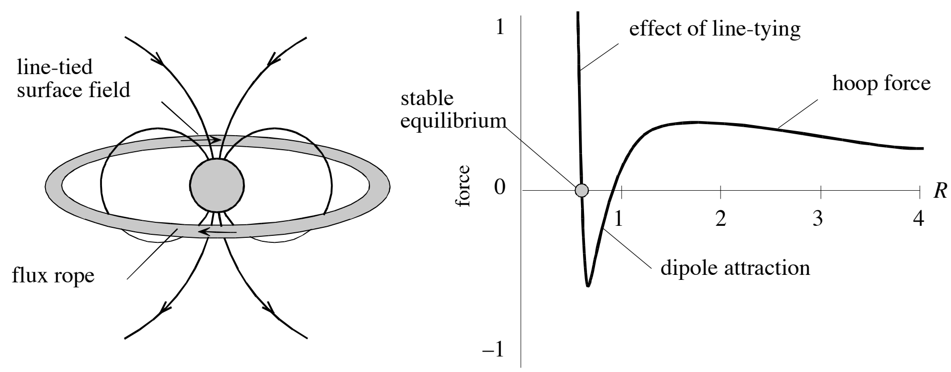

Fig. 6.18. A stable toroidal equilibrium. *a* The addition of a line-tying surface representing the surface of the Sun creates the possibility of a stable equilibrium. Surface currents (which can be modeled using an image current) create an additional magnetic field component that gives rise to a second equilibrium position as shown in *b*. The new equilibrium is stable because displacements away from it produce a restoring force.

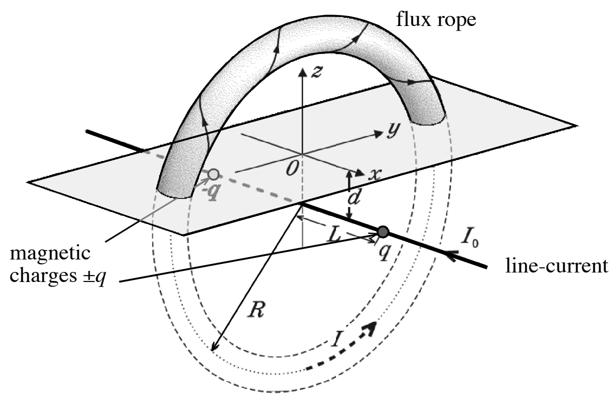

Fig. 6.19. The three-dimensional flux-rope model of Titov and Démoulin (1999). The coronal magnetic field is produced by three different sources consisting of a flux rope current, a pair of magnetic charges, and a line current. The source regions located below the surface are fictitious constructs used to create the coronal field. The model does not prescribe the form of the subsurface field.

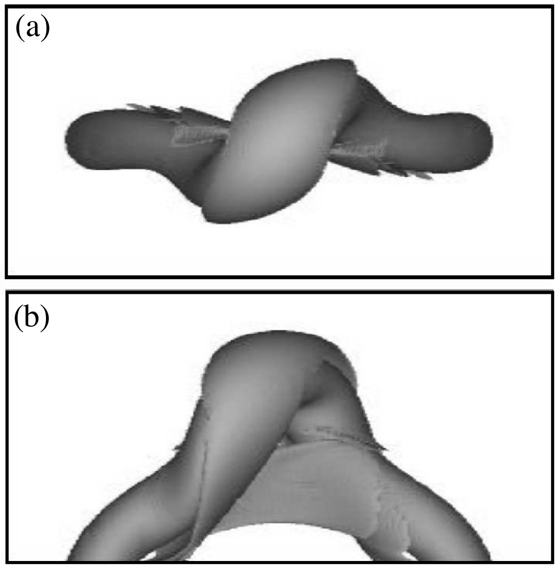

Fig. 6.20. Top view (a) and side view (b) of constant current density surfaces from the simulation by Török *et al.* (2004) for an unstable Titov and Démoulin equilibrium.

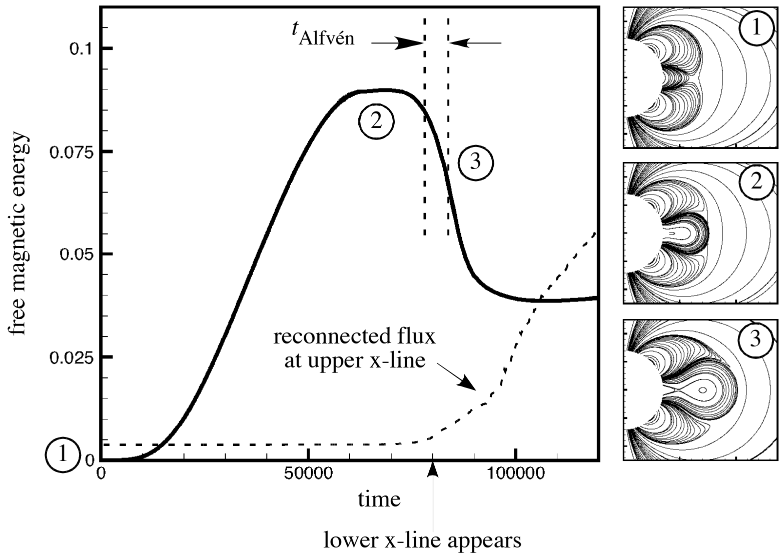

Fig. 6.21. Numerical simulation of a storage model proposed by Antiochos *et al.* (1999). The panel at left shows the free magnetic energy as a function time, while the three panels at right show contours of the magnetic flux surfaces at three different times (after MacNeice *et al.* 2004).

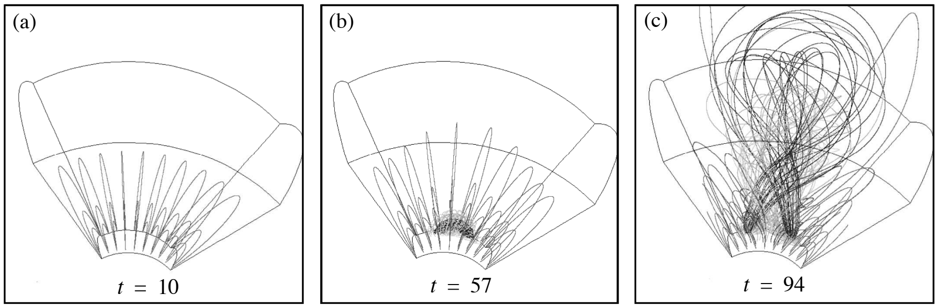

Fig. 6.22. Numerical simulation of a CME occurring in an emerging flux region (from Fan and Gibson (2004, 2007). Panel *a* shows the early coronal magnetic field at $t = 10$, prior to the emergence of any flux. Panel *b* shows a stable, quasi-equilibrium configuration at $t = 57$, after some flux has slowly emerged into the corona. Panel *c* shows a dynamic, nonequilibrium configuration at $t = 94$ after a loss of equilibrium has occurred due to continued slow emergence of flux. Time is is in units of the Alfvén scale time of system.

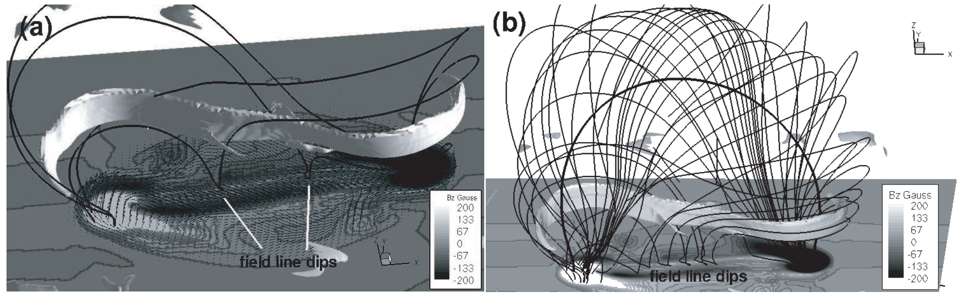

Fig. 6.23. Two views of the magnetic field configuration and current density distribution at $t = 72.8$ in the simulation of Manchester *et al.* 2004. Panel (a) shows the view from above, while panel (b) shows the view from an angle. The base surface is shaded according to the value of the normal magnetic field component. The black and gray curves show two magnetic field lines. The bright gray, ribbon like structure shows the position of the current sheet that develops during the slow emergence of the flux into the corona. This sheet occurs prior to any eruption and plays a critical role in allowing mass to drain along field lines (after Manchester *et al.* 2004).

7
Shocks in heliophysics

by Merav Opher

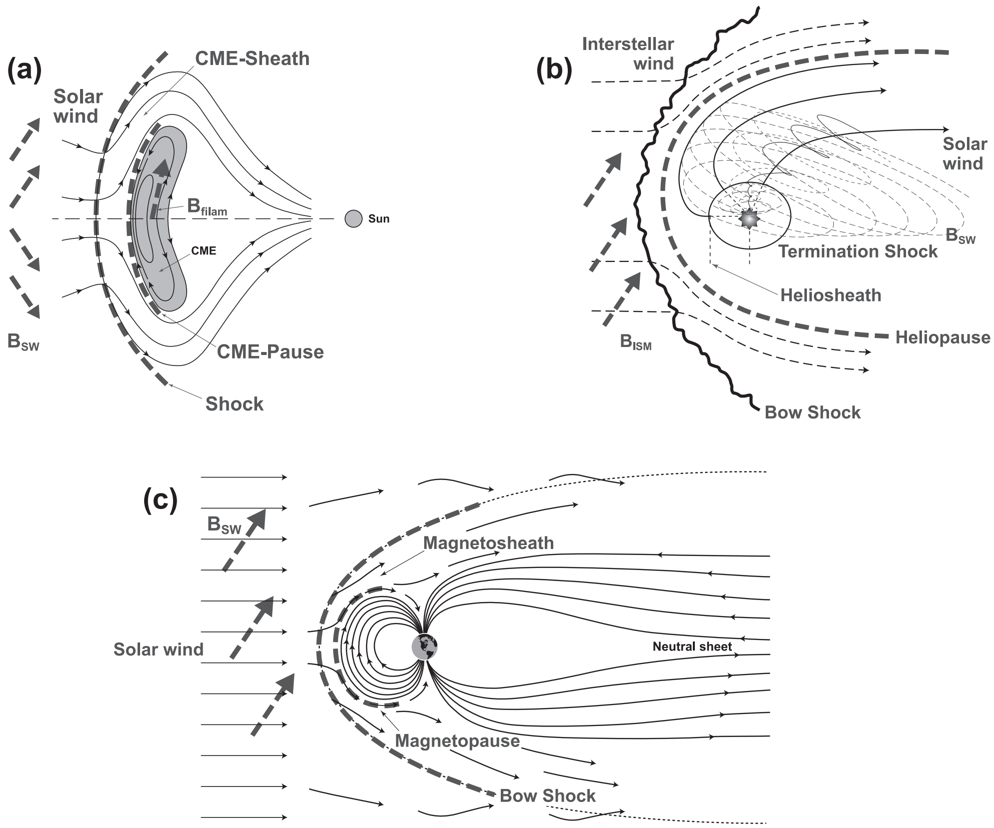

Fig. 7.1. Schematic comparison of shocks around CMEs, the heliosphere, and the magnetosphere. The figure shows some of the types of shocks and sheaths that exist in the heliosphere and their universal basic structures: (a) a CME; (b) the outer heliosphere, and (c) Earth's magnetosphere. The same basic structures appear: shocks where the solar wind becomes subsonic; the sheaths that separate the subsonic solar wind from the obstacle ahead; and the "pause" where there is a pressure equilibrium between the subsonic solar wind and the obstacle's environment. In the case of a CME these three structures are the shock, CME-sheath, CME-pause and the obstacle is the magnetic filament that drives the CME. In the case of the outer heliosphere the structures are the termination shock, heliosheath, and heliopause. The obstacle is the interstellar wind and the magnetic field it is carrying. If the interstellar wind is supersonic there is an additional shock, the bow shock. In the case of the Earth's magnetosphere the structures are the shock, the magnetosheath, the magnetopause and the obstacle is the Earth's dipolar magnetic field.

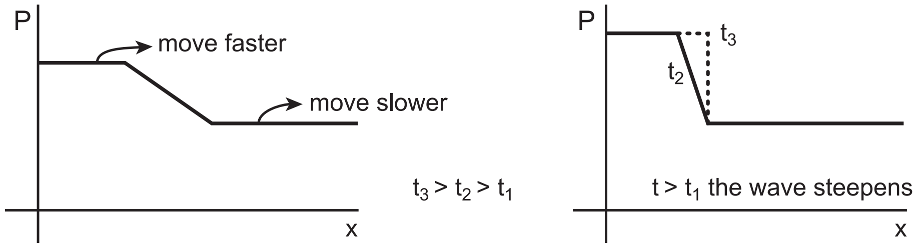

Fig. 7.2. Diagram of the steepening of a wave. Three phases are shown: t_1 in the left panel, and $t_{2,3}$ in the right panel, with $t_3 > t_2 > t_1$.

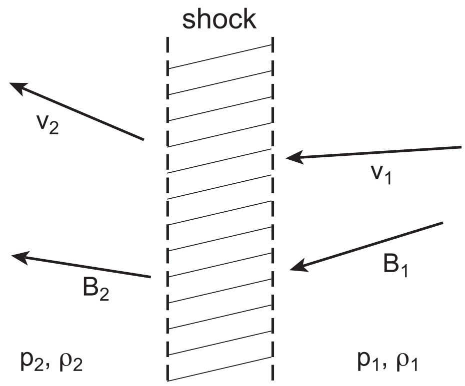

Fig. 7.3. Diagram showing the region upstream (left) and downstream of a shock.

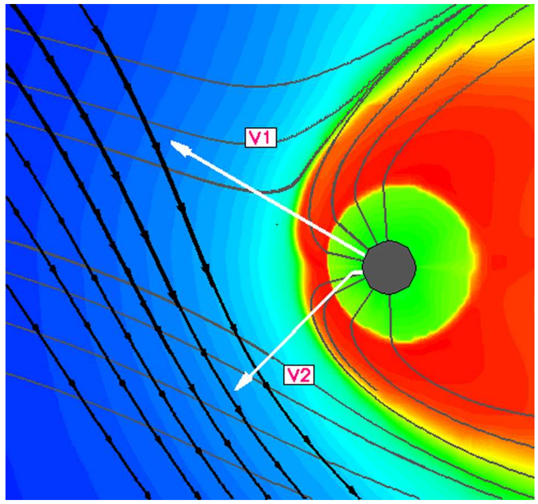

Fig. 7.4. Meridional cut from a heliosphere simulation including the plasma and the neutral H atoms (Opher, 2009). The contours are the plasma temperature. The blue region is the region beyond the heliopause; the red the heliosheath and the green the region upstream the termination shock. The black lines are the interstellar magnetic field; and the grey lines are the plasma streamlines. The (projected) trajectories of the Voyager spacecraft 1 and 2 are also indicated.

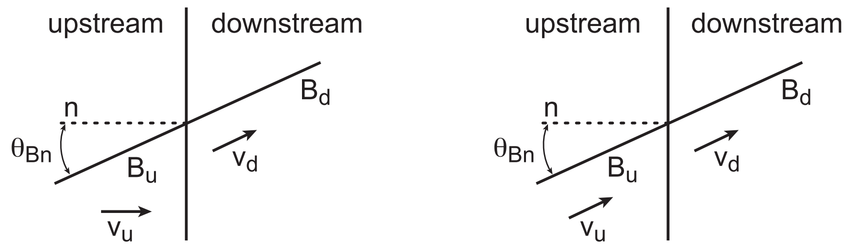

Fig. 7.5. Shock reference frames: a) normal-incident and b) de Hoffman-Teller frame.

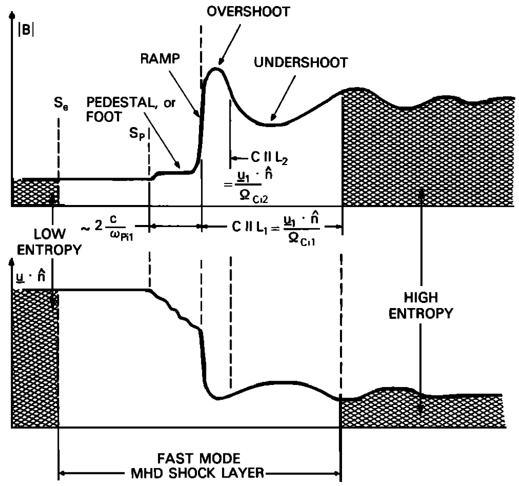

Fig. 7.6. Substructure terminology of supercritical, fast mode, collisionless shock layer (from Scudder et al., 1986).

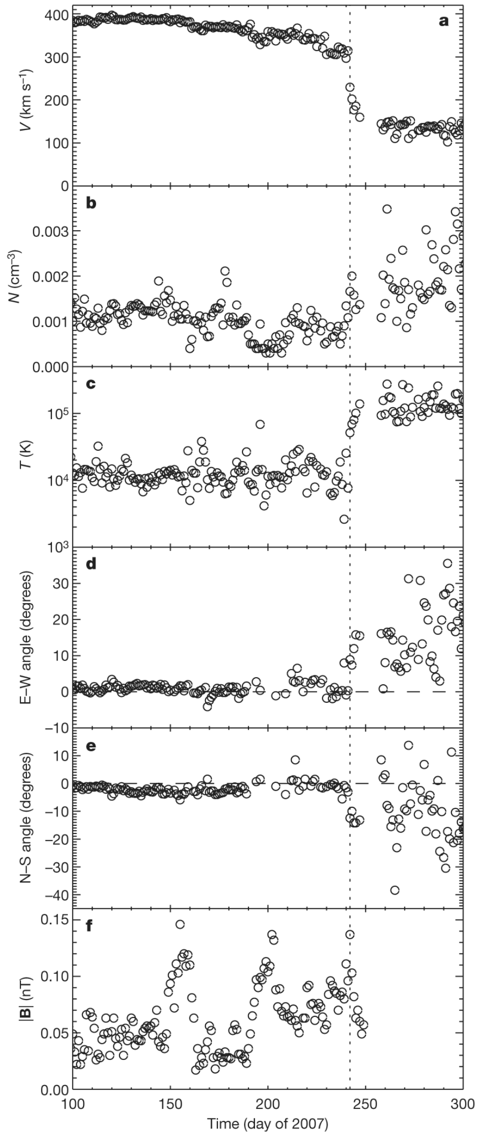

Fig. 7.7. Crossing of the termination shock by Voyager 2. Daily averages of solar wind speed V (a), density N (b), temperature T (c), east-west flow angle (d), north-south flow angle (e) and magnetic field magnitude (f). Flow angles are in the RTN coordinate system, where R is radially outwards, T is parallel to the plane of the solar equator and positive in the direction of the Sun's rotation, and N completes a right-handed system. The east-west angle is the angle in the R-T plane and the north-south angle is the angle out of the R-T plane. The dashed line shows the termination shock crossing, where the speed decreases by a factor of about two, the density increases by a factor of two, the proton temperature increases to near 100,000 K, and the flow is deflected consistent with flow away from the nose direction of the heliosphere, that is, the direction toward the local interstellar medium flow. (From Richardson et al., 2008)

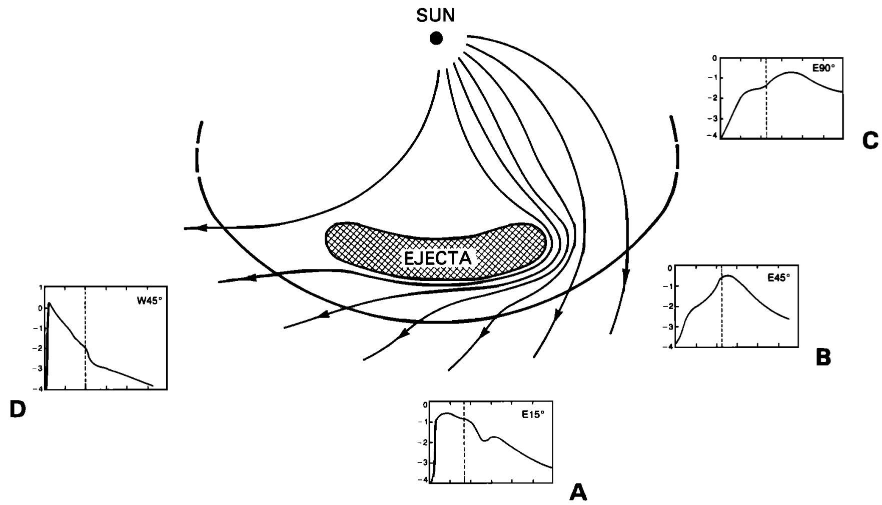

Fig. 7.8. Representative profiles of 20 MeV proton events for different positions of the observatory with respect to a shock. The draping of the field lines around the ejecta is only a suggestion. From Cane et al. (1988).

8
Particle acceleration in shocks

by Dietmar Krauss-Varban

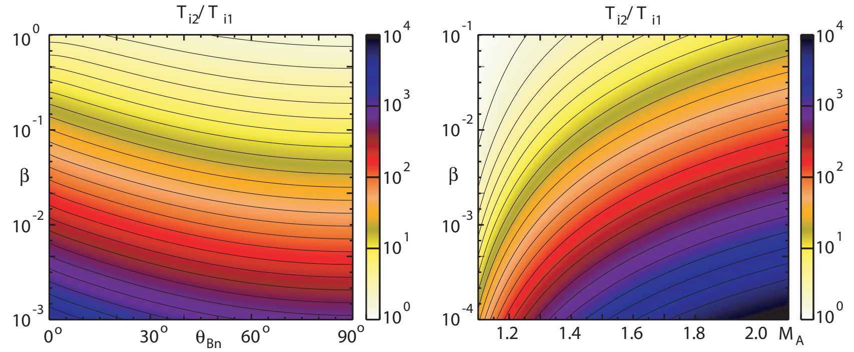

Fig. 8.1. Iso-contours of shock heating, expressed as the ratio between downstream to upstream ion temperature T_{i2}/T_{i1}, as a function of shock-normal angle θ_{Bn} (fixed $M_{\mathrm{A}} = 2$) and Alfvén Mach number M_{A} (fixed $\theta_{\mathrm{Bn}} = 45°$) for low β plasmas. Derived from standard Rankine-Hugoniot conditions for fast shocks, assuming a specific heat ratio $\gamma = 5/3$. The graphs show that for a wide range of angles, there can be very substantial downstream heating at sufficiently low plasma β, as present in much of the solar corona. Such extreme heating may help form a seed population for further acceleration.

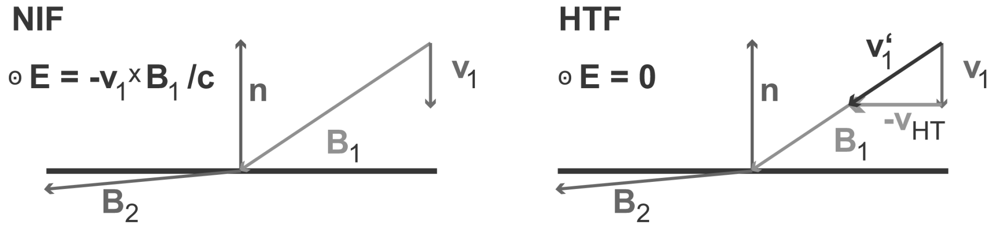

Fig. 8.2. Difference between normal-incidence frame (NIF) and de Hoffman-Teller frame (HTF) at fast-mode shocks. The NIF is the shock frame in which the upstream flow is aligned with the shock normal. As a consequence, the upstream out-of-plane motional electric field is non-zero and, from Maxwells equations in steady state, actually the same downstream. Transformation to the HTF is along the plane shock surface until the upstream flow vector coincides with the magnetic field. Therefore, the motional electric field vanishes, and the description of particle motion simplifies to energy and magnetic moment conservation. When back-transforming to the NIF, one discovers that reflected particles have attained a speed close to twice the transformation velocity VHT, which evidently becomes very large for nearly perpendicular shocks.

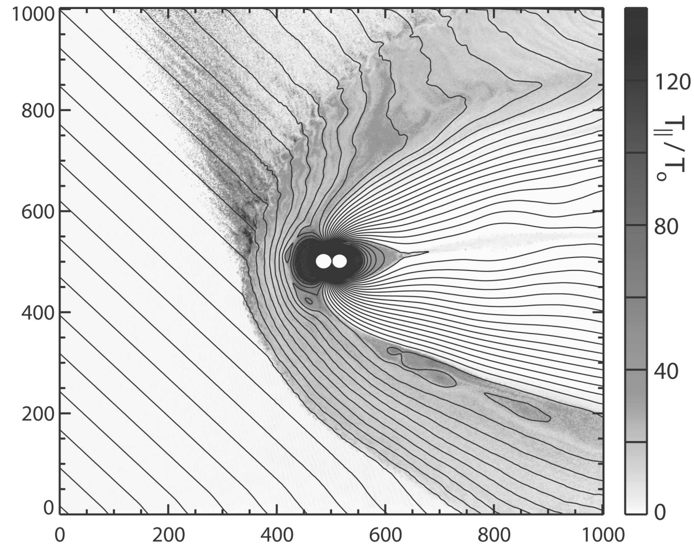

Fig. 8.3. Example of a two-dimensional (2-D) hybrid simulation of the solar wind – magnetosphere interaction (from Krauss-Varban et al., 2008). Shown are contours of the magnetic field lines (upstream IMF angle $\theta = 45°$) and the normalized parallel ion temperature $T_{\|}$, as a proxy of ion acceleration. As well-documented in many observations of the Earth's bow shock, the ion foreshock starts close to $\theta_{\mathrm{Bn}} = 45°$ with energized and backstreaming ions, and simultaneous excitation of waves (visible in the field line undulations). Conversely, at this scale, and with the number of pseudo-particles used in the simulation, there are virtually no upstream ions at larger shock-normal angles.

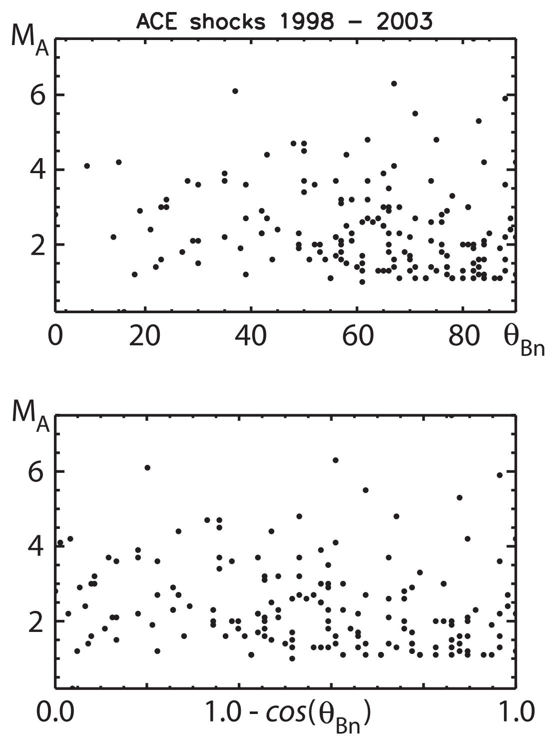

Fig. 8.4. Scatter-plot of all interplanetary, forward-propagating fast-mode shocks observed with the ACE satellite and in the ACE magnetometer database, in the period 1998 to 2003 (M_{A} and θ_{Bn} as reported from the ACE magnetometer team database). Top: ordering with shock-normal angle θ_{Bn}. Bottom: ordering with $1.0 - \cos(\theta_{\mathrm{Bn}})$, which takes into account the solid angle viewing statistics. Even in this corrected plot, one can see a slight preference for oblique angles, as expected from the solar wind Parker spiral. More importantly, it is evident that most IP shocks are rather slow. And, while they typically will have a detectable energetic particle environment, the associated energy range and fluxes are of little interest in the context of detrimental Space Weather effects, except for the rare, higher M_{A} cases. (from Gosling et al., 1984)

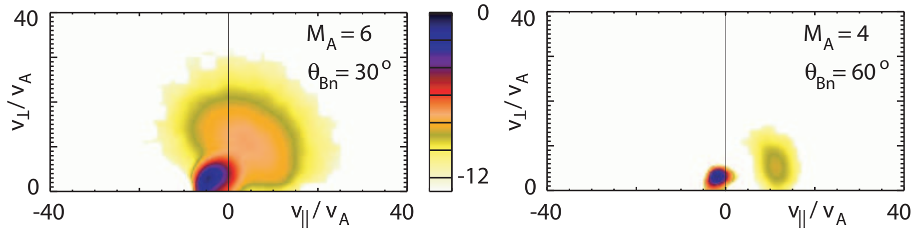

Fig. 8.5. Sketch of upstream proton distributions (perpendicular and parallel to the ambient magnetic field) in the shock frame from planar, 2-D hybrid shock simulations at quasi-parallel ($\theta = 30$) and oblique ($\theta = 60°$) angles. As in many documented observations of the Earths bow shock and at sufficiently high Mach number IP shocks, at quasi-parallel shock-normal angles, protons cannot only easily travel upstream and generate waves, but they also easily scatter in these self-generated waves to form a diffuse distribution that forms a contiguous cloud of both upstream ($v_{\|} > 0$) and downstream-directed ($v_{\|} < 0$) particles. Conversely, at oblique shocks, only a highly-dilute upstream-propagating beam with enhanced perpendicular energy is found, and even that can only be seen with very good particle statistics, in simulations. Unlike the quasi-parallel shock, a higher Mach number does not help initially, but typically makes it more difficult for ions to make it upstream, in the first place.

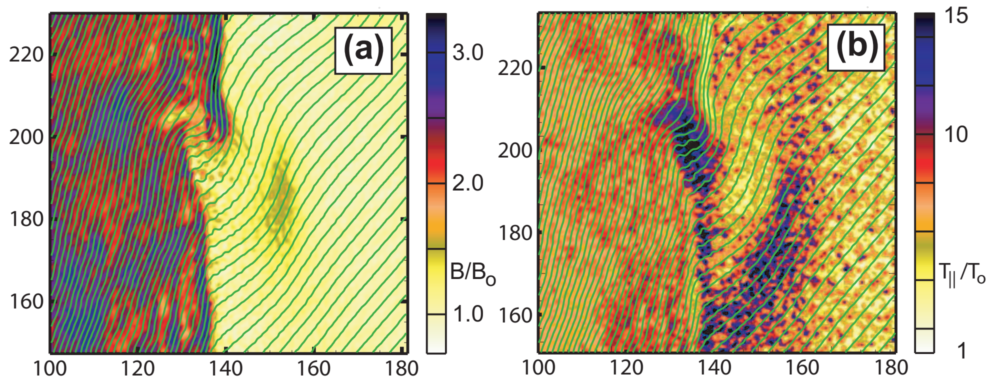

Fig. 8.6. Magnetic field line contours and (a) total magnetic field, and (b) parallel temperature $T_{\|}$ normalized to upstream in a subset of a 2-D hybrid simulation of an oblique shock ($\theta = 50°$; from Krauss-Varban et al., 2008). It can be seen how compressional waves generated by dilute beams disrupt the shock and change the local $\theta_{\rm Bn}$, in turn allowing more upstream wave and particle production than expected at the oblique shock. This process appears to enhance upstream energetic proton fluxes by two to three orders of magnitude.

9

Energetic particle transport

by Joe Giacalone

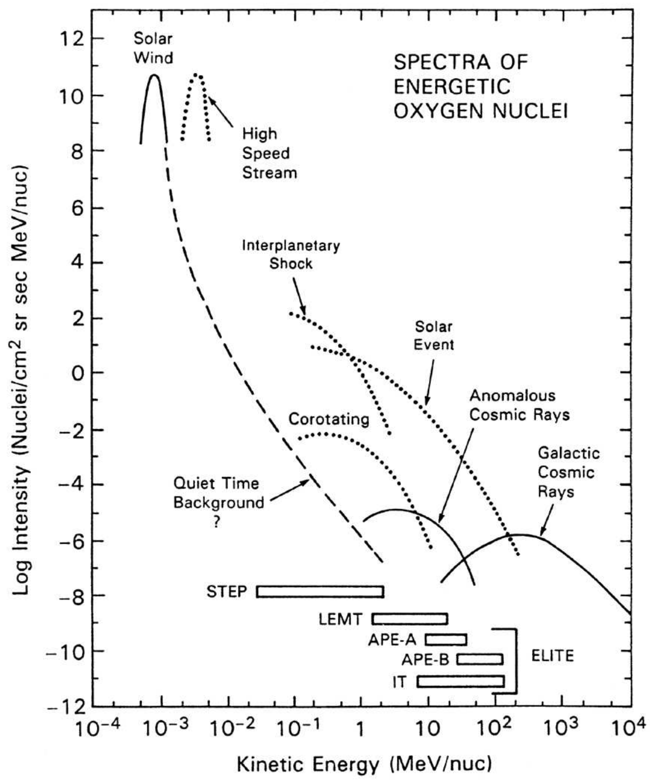

Fig. 9.1. An illustration of the energy spectrum of cosmic rays in the heliosphere based on spacecraft observations. A phenomenological description of the various types of energetic particles indicated in this figure is given in Section 9.1 (see also Fig. 3.1).

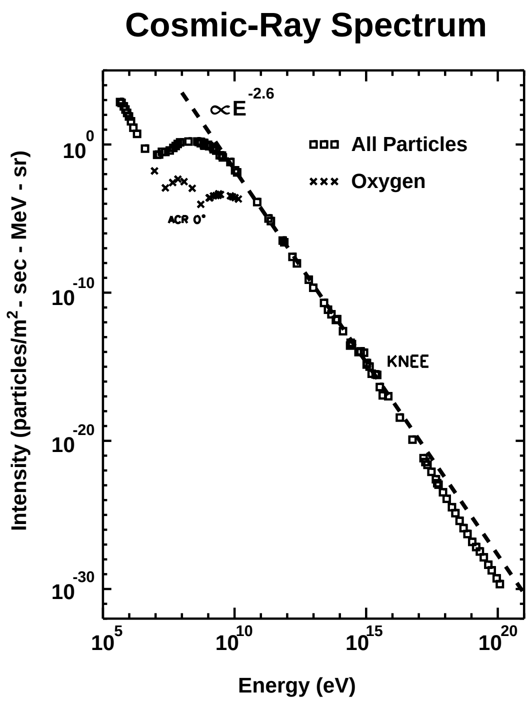

Fig. 9.2. The cosmic-ray spectrum observed at Earth's orbit.

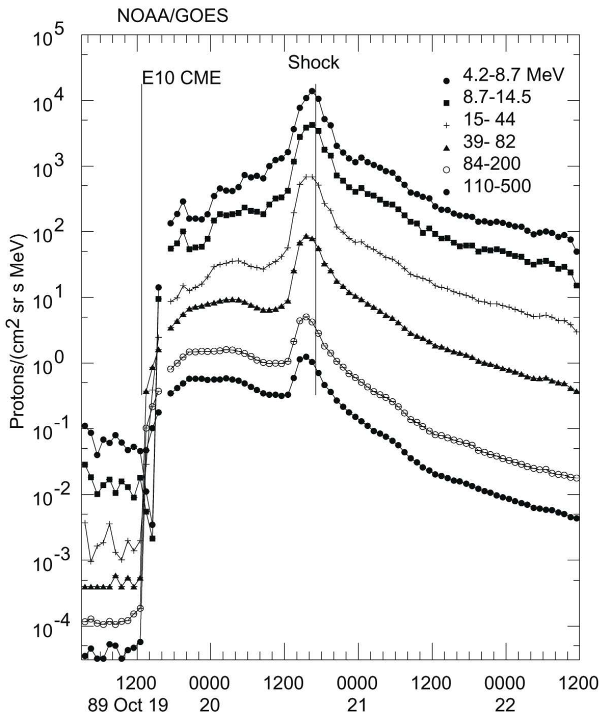

Fig. 9.3. The intensity of energetic protons as a function of time for a solar-energetic particle event associated with a coronal mass ejection on 10/19/1989.

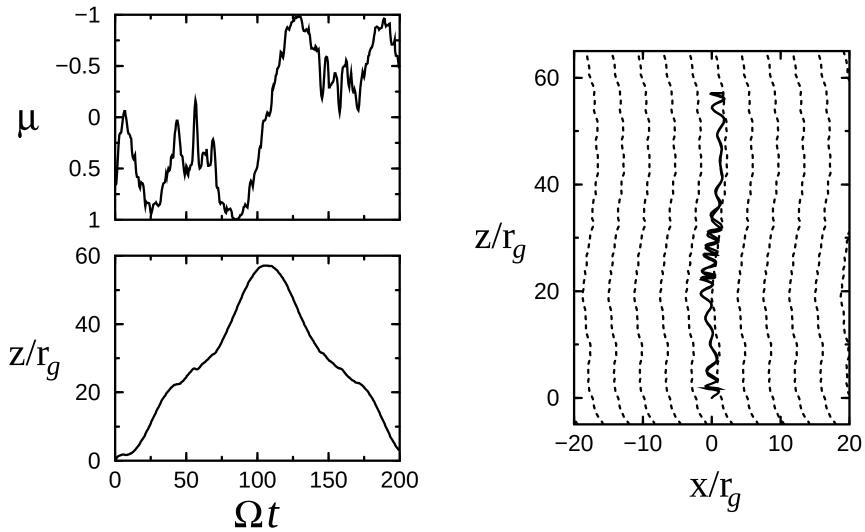

Fig. 9.4. Various representations of the orbit of a single proton moving in an irregular magnetic field, that contains a variety of scales, including those that are comparable to the gyroradius of the proton. The upper left plot shows the cosine of the pitch angle as a function of time, and the lower left plot shows the position along the direction of the average magnetic field (z direction), as a function of time. The right plot shows the position of the particle as projected onto the x-z plane.

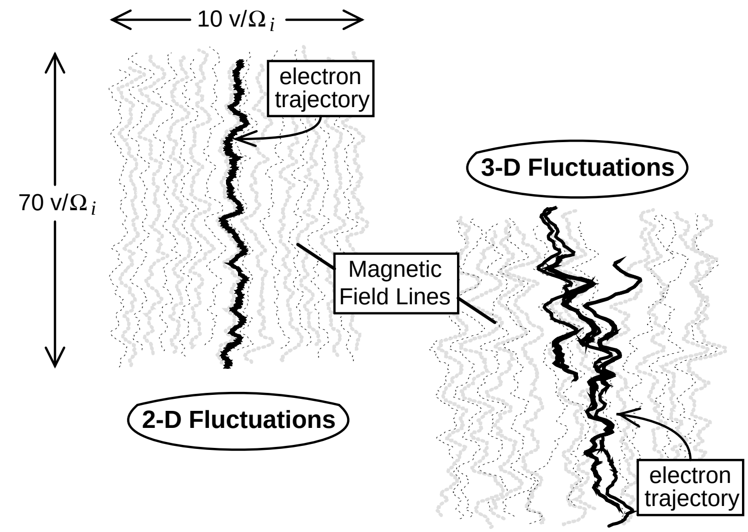

Fig. 9.5. The trajectories of two electrons moving in a spatially irregular (but static in time) magnetic field. In the upper left plot, the magnetic field depends on only two spatial coordinates, in which case theory requires that the particle remains within one gyroradius of a particular field line, which is the case. In the right panel, the field depends on all three spatial coordinates and the electron is not strictly tied to the same magnetic line of force.

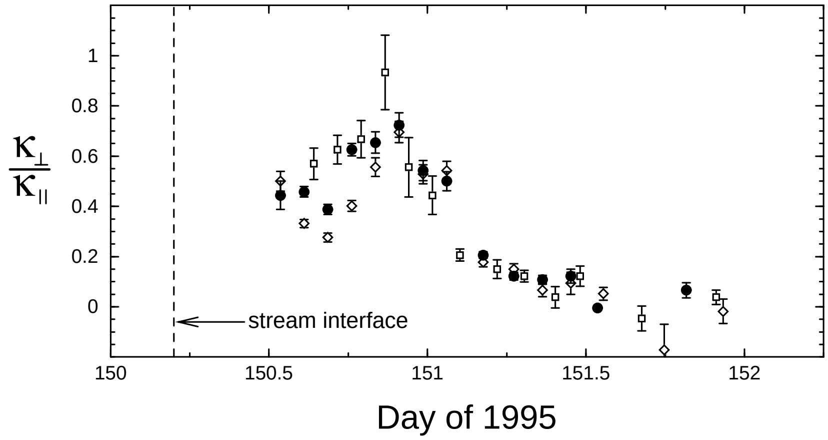

Fig. 9.6. The inferred value of the ratio of perpendicular to parallel diffusion coefficients for energetic ions, based on the observed particle streaming direction and magnetic field, during the passage of a corotating interaction region as seen by the Wind spacecraft at 1 AU (adapted from Dwyer et al., 1997).

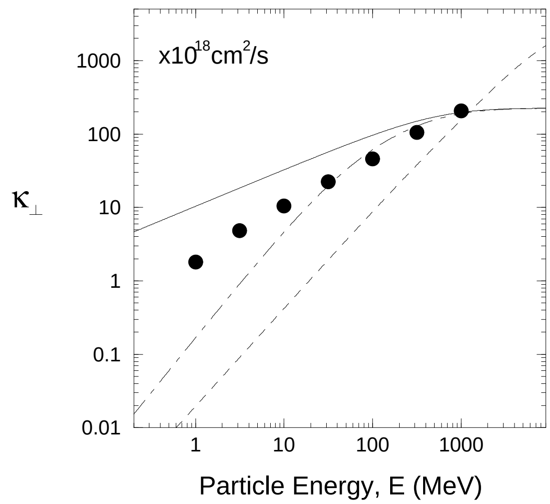

Fig. 9.7. The cross-field diffusion coefficient based on three different analytical approximations (curves) and numerical simulations (filled-in circle symbols).

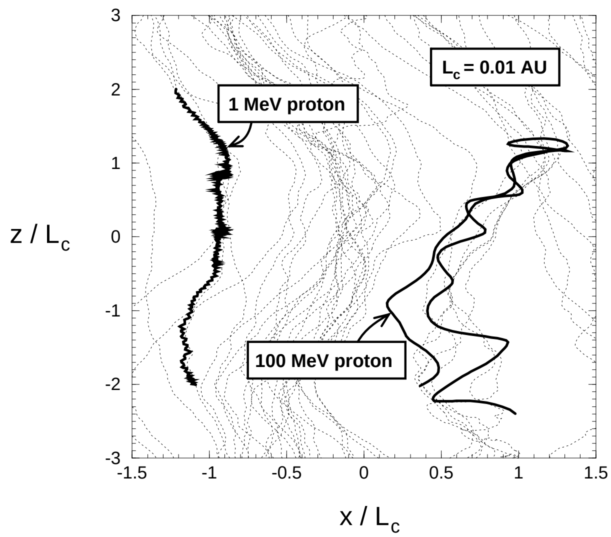

Fig. 9.8. Individual charged particles with different energies (as indicated) moving in an irregular magnetic field (grey lines). This figure is from Giacalone and Jokipii (1999).

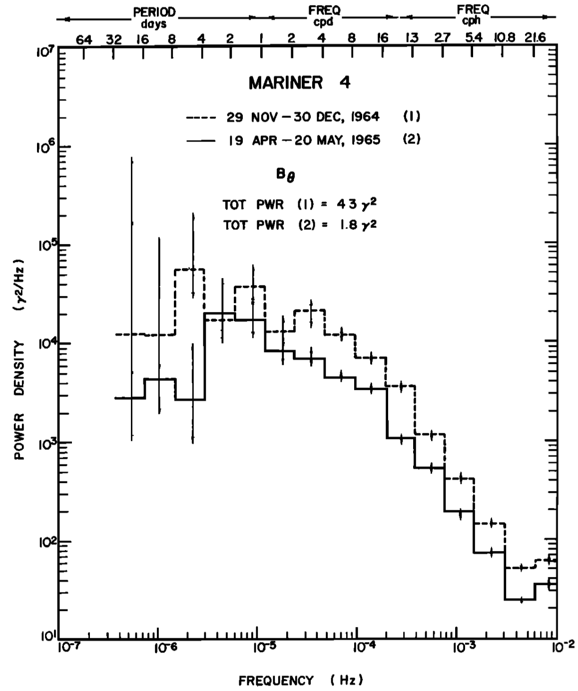

Fig. 9.9. The observed power spectrum of the latitudinal component of the interplanetary magnetic field (from Jokipii and Coleman, 1968).

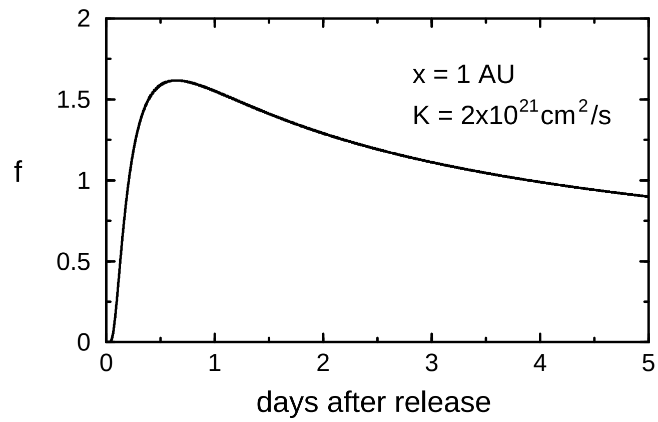

Fig. 9.10. Solution to the one-dimensional diffusion equation for a point-source release at a position 1 AU away from an observer: $f(1,t)$ from Eq. (9.25)..

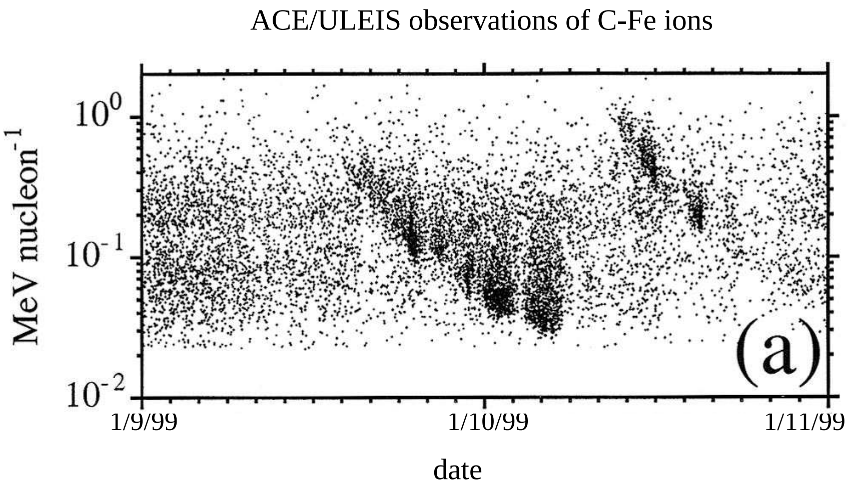

Fig. 9.11. A solar energetic particle (SEP) event, associated with an impulsive solar flare, seen by ACE/ULEIS. Each dot represents the detection of a particle by the detector. Two distinct events are shown. Figure adapted from Mazur *et al.* (2000).

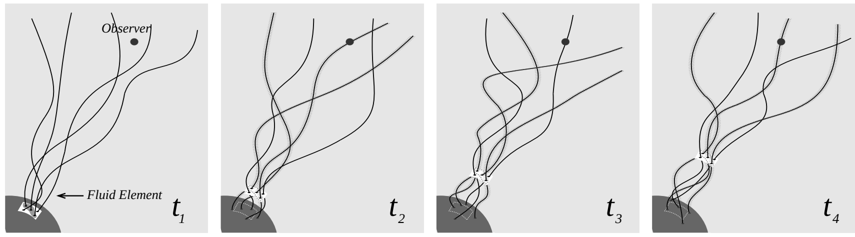

Fig. 9.12. An illustration a possible interpretation of the intermittent intensity variations seen within the events shown in Fig. 9.11. The plots show 5 magnetic field lines, 3 of which are populated with field lines at $t = 0$ (far left panel), and the other 2 are not. An observer is indicated towards the upper part of each plot. As the observer moves passed various field lines which are advected with the solar wind flow, it sometimes sees energetic particles and sometimes not, depending on whether the field lines it is presently seeing is connected to the source.

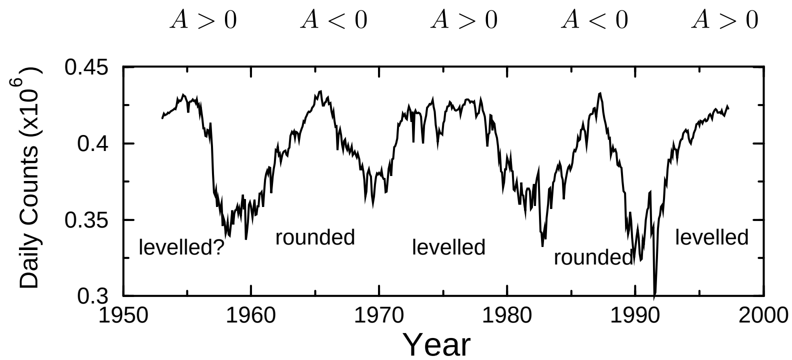

Fig. 9.13. Climax neutron monitor daily count rate of neutrons produced by the interaction of a primary cosmic ray with Earth's atmosphere. The meaning of A is defined in Fig. 9.14.

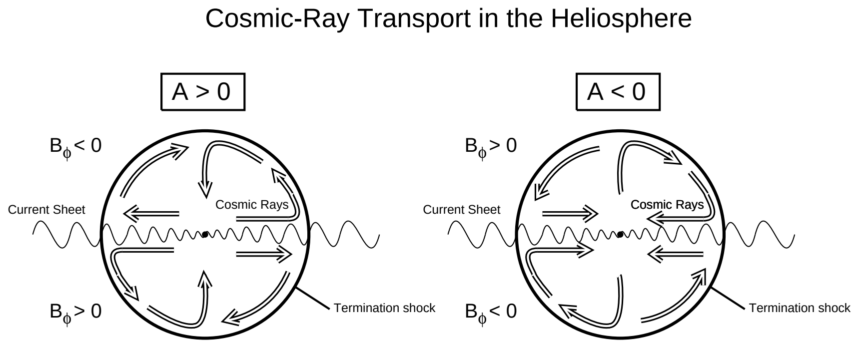

Fig. 9.14. Drift motion of cosmic rays in the heliosphere for two different solar magnetic-polarity cycles. The two polarities of the solar magnetic field are separated by the heliospheric current sheet. The value of $A > 0$ during the period in which the solar magnetic field is outward in the north and inward in the south. The termination of the solar wind is also shown.

10

Energy conversion in planetary magnetospheres

by Vytenis Vasyliūnas

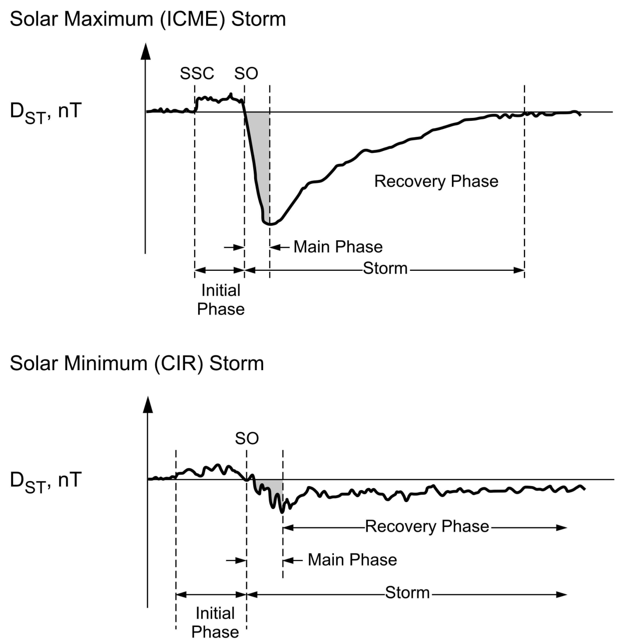

Fig. 10.1. Schematic time history of geomagnetic field variation for two characteristic magnetic storms. Time range: several days. Vertical variation range: $\sim 100 - 200\,\mathrm{nT}$. SSC: storm sudden commencement. SO: storm onset. The top panel shows the storm development in response to a characteristic interplanetary coronal mass ejection (ICME), and the bottom panel that for the passage of a corotating interaction region (CIR). (Figure adapted from Tsurutani *et al.*, 2006)

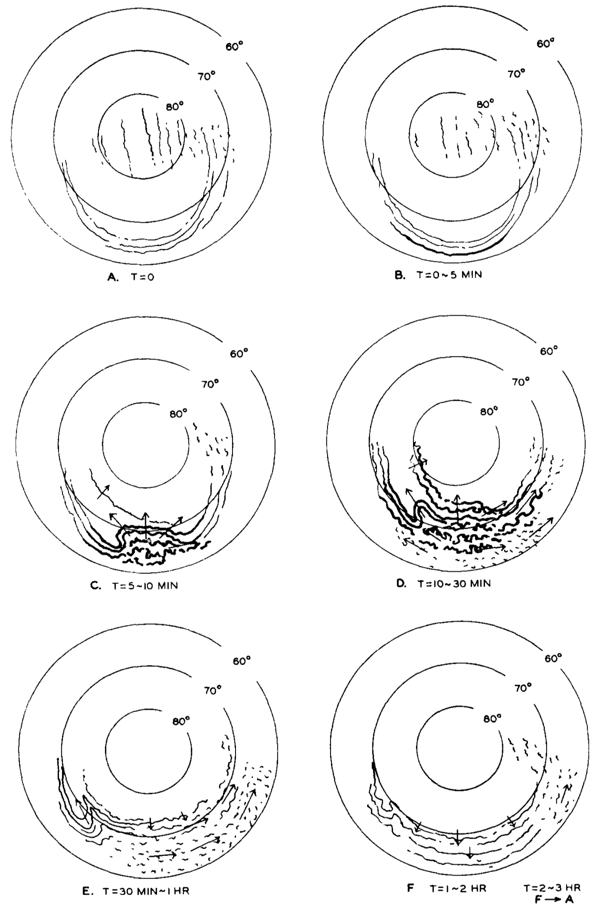

Fig. 10.2. Schematic diagram of an auroral substorm. View from above the north pole, circles of constant geomagnetic latitude, Sun toward the top (Akasofu, 1964)

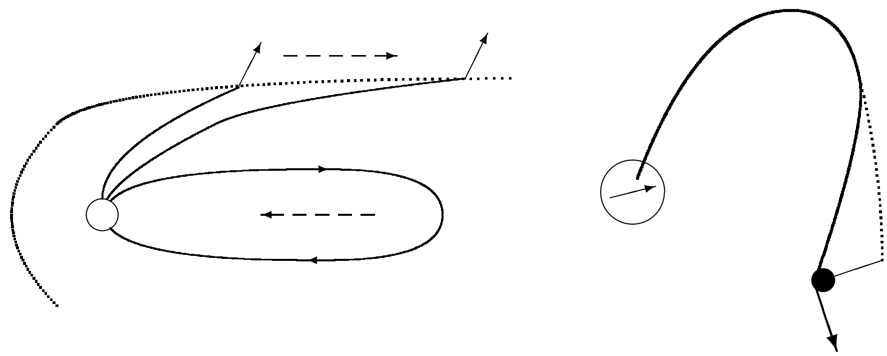

Fig. 10.3. (a) Left: deformation of magnetotail field by external plasma flow. Solid lines: magnetic field lines. Dashed arrows: plasma flow direction. Dotted line: magnetopause. (b) Right: deformation of planetary magnetic field by torque from magnetospheric plasma element (black sphere). Solid line: actual magnetic field line. Dashed line: undistorted magnetic field line. Arrow on planet's surface: direction of rotational motion.

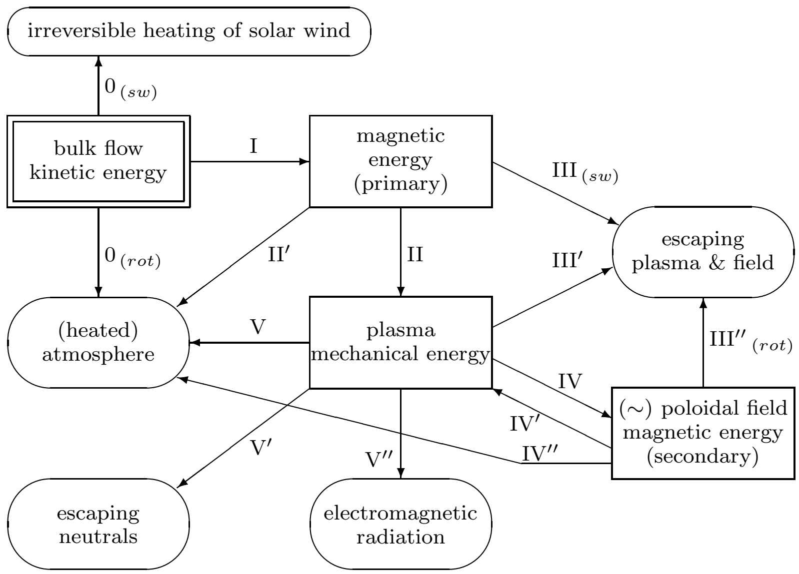

Fig. 10.4. (Simplified) general energy flow chart for planetary magnetospheres and ionospheres. Rectangular boxes: energy reservoirs. Rounded boxes: energy sinks. Lines: energy flow/conversion processes. (Note: only the energy-flow paths are shown, not the mass-flow paths.)

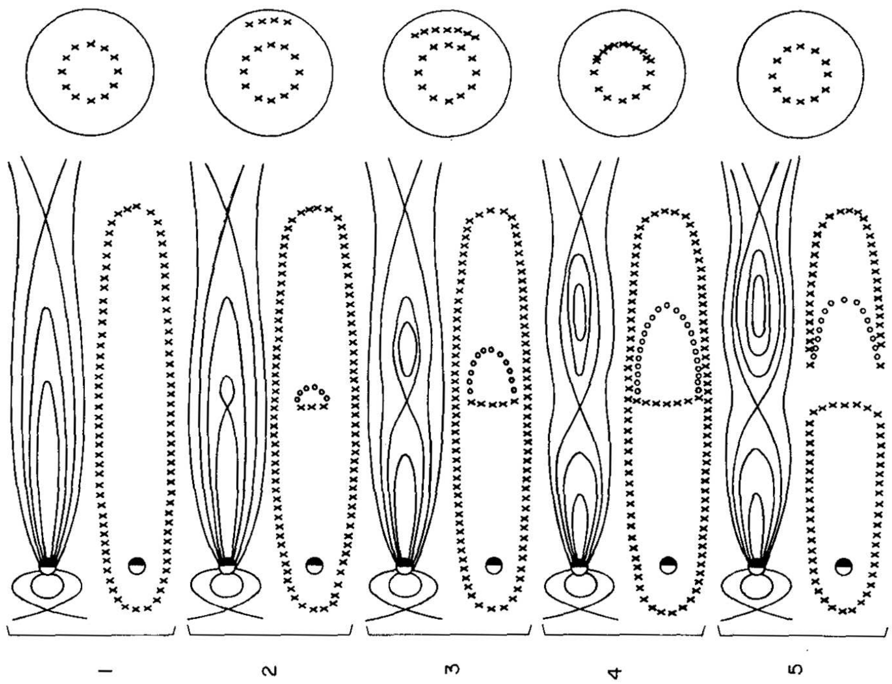

Fig. 10.5. Possible changes of the magnetic field topology in the magnetotail of a solar-wind-dominated magnetosphere. The diagram (from Vasyliūnas, 1976) is shown rotated to facilitate comparisons with diagrams of filament eruptions in, e.g., Chapter 6: the solar wind here blows from bottom to top, rather than from left to right as in the original and in the analogous figures of Chapter 10 in Vol. I. Each panel in the sequence shows a side view of the magnetic field (left), the outline of the X lines seen from above the north pole (right), and a top-down view of the mapping of the reconnection region onto the Earth (top)

11
Energization of trapped particles

by Janet Green

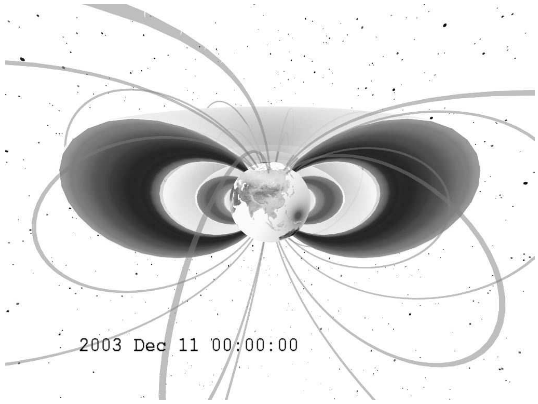

Fig. 11.1. Schematic depiction of Earth's electron radiation belts courtesy of the NASA/Goddard Space Flight Center Scientific Visualization Studio.

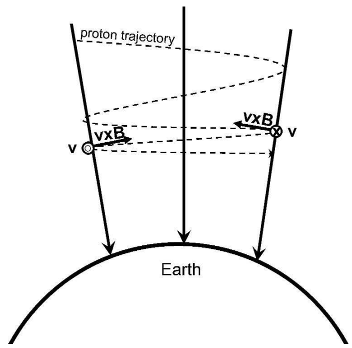

Fig. 11.2. Schematic diagram showing the Lorentz force as a particle moves into the magnetic field gradient at Earth's poles.

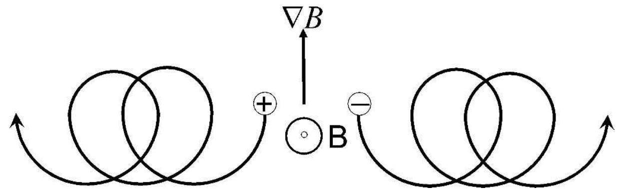

Fig. 11.3. Schematic diagram for the gradient-B drift.

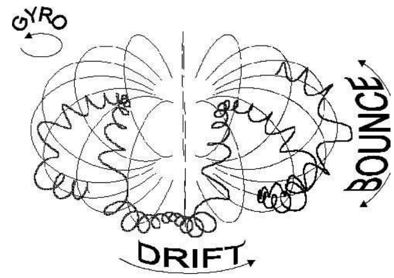

Fig. 11.4. Schematic diagram of particle motion in a dipole magnetic field.

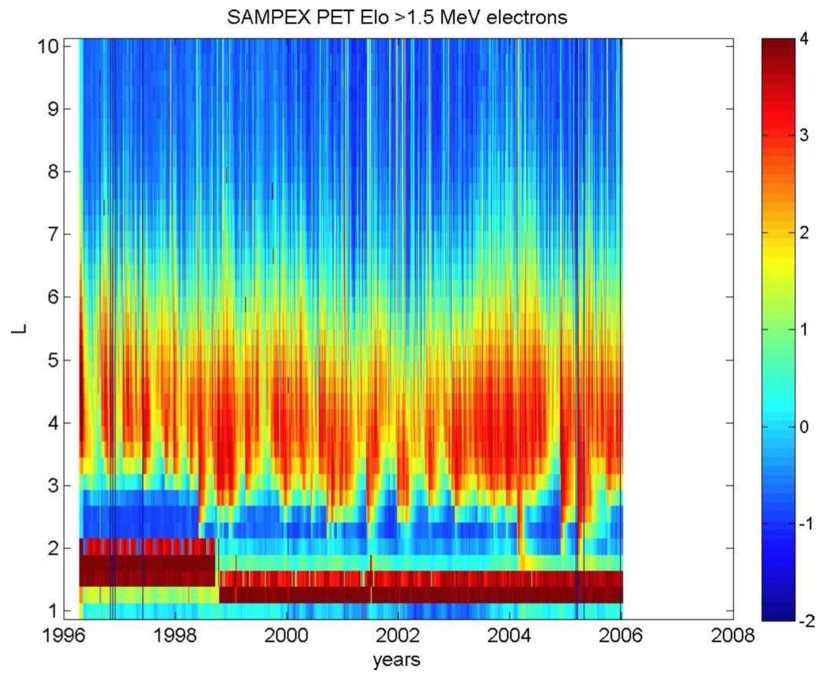

Fig. 11.5. Radiation-belt electron flux ($^{10}\log$(counts/sec)) as measured by the Proton Electron Telescope (PET) Elo channel that measures electrons with energies $> 1.5\,\mathrm{MeV}$ on the SAMPEX satellite. The data are averaged in 0.25 L and 1 day bins.

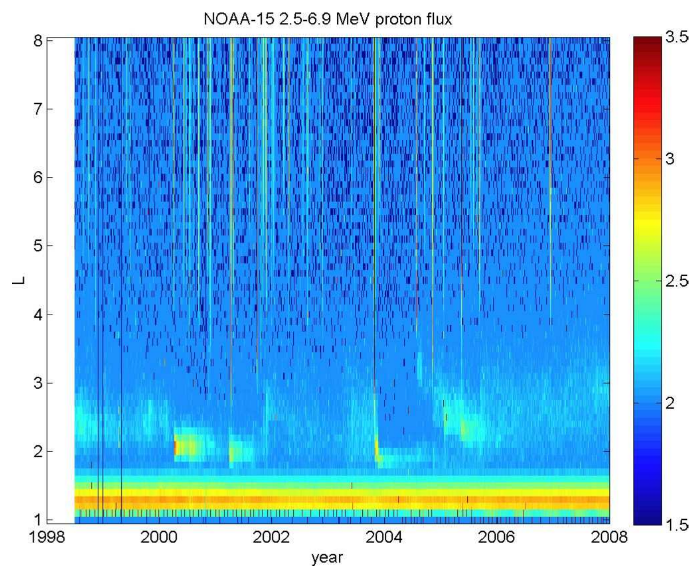

Fig. 11.6. Radiation-belt proton flux (number per cm^2-s-str on a logarithmic scale) from the SEM-2 instrument that measures protons with energies between 2.5 and 6.9 MeV on the NOAA-15 satellite. The data are averaged in 0.2 L and 1 day bins.

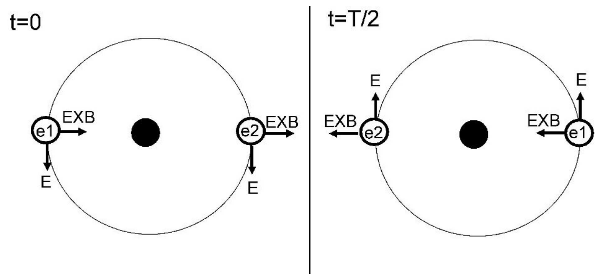

Fig. 11.7. Schematic diagram of an electron in drift resonance with a ULF wave. The left panel shows two electrons labeled e1 and e2, the direction of the wave electric field, and the direction of the particles EXB drift at time t=0. The right panel shows the same properties half a wave period and electron drift period later.

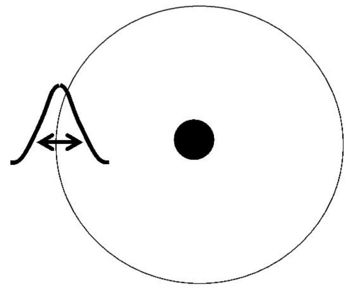

Fig. 11.8. Schematic diagram showing how a distribution of electron spreads in L where the black circle represents Earth and the light circle represents the drift path about Earth. Electrons spread uniformly towards and away from Earth.

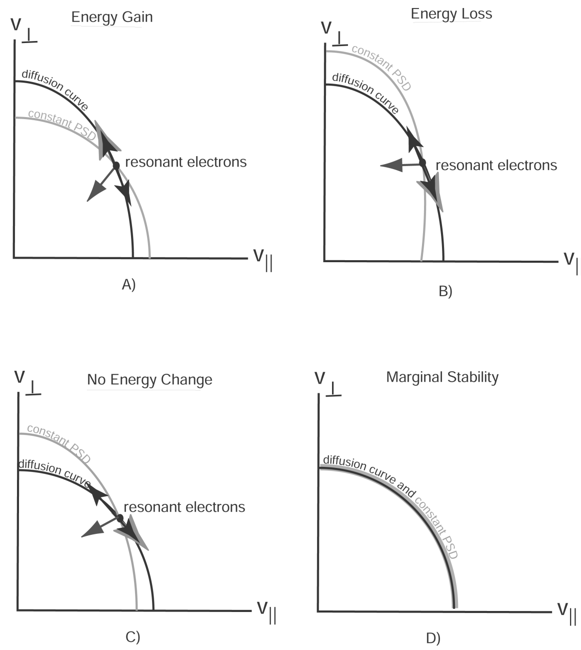

Fig. 11.9. Schematic diagram showing how a distribution diffuses in pitch angle and energy while interacting with a VLF wave.

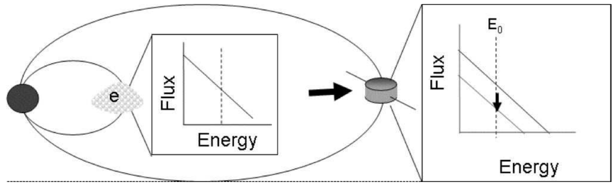

Fig. 11.10. Schematic diagram showing the adiabatic motion and flux decrease observed by a satellite caused by the "Dst effect." The blue circle represents Earth. The left most box represents the spectrum of electron flux versus energy at a position initially Earthward of the satellite. The right most box shows how that spectrum appears after the electrons move outward to the position of the satellite. The entire spectrum shifts to lower energy generally resulting in a measured flux decrease at constant energy.

12

Flares, CMEs, and atmospheric responses

by Tim Fuller-Rowell and Stanley C. Solomon

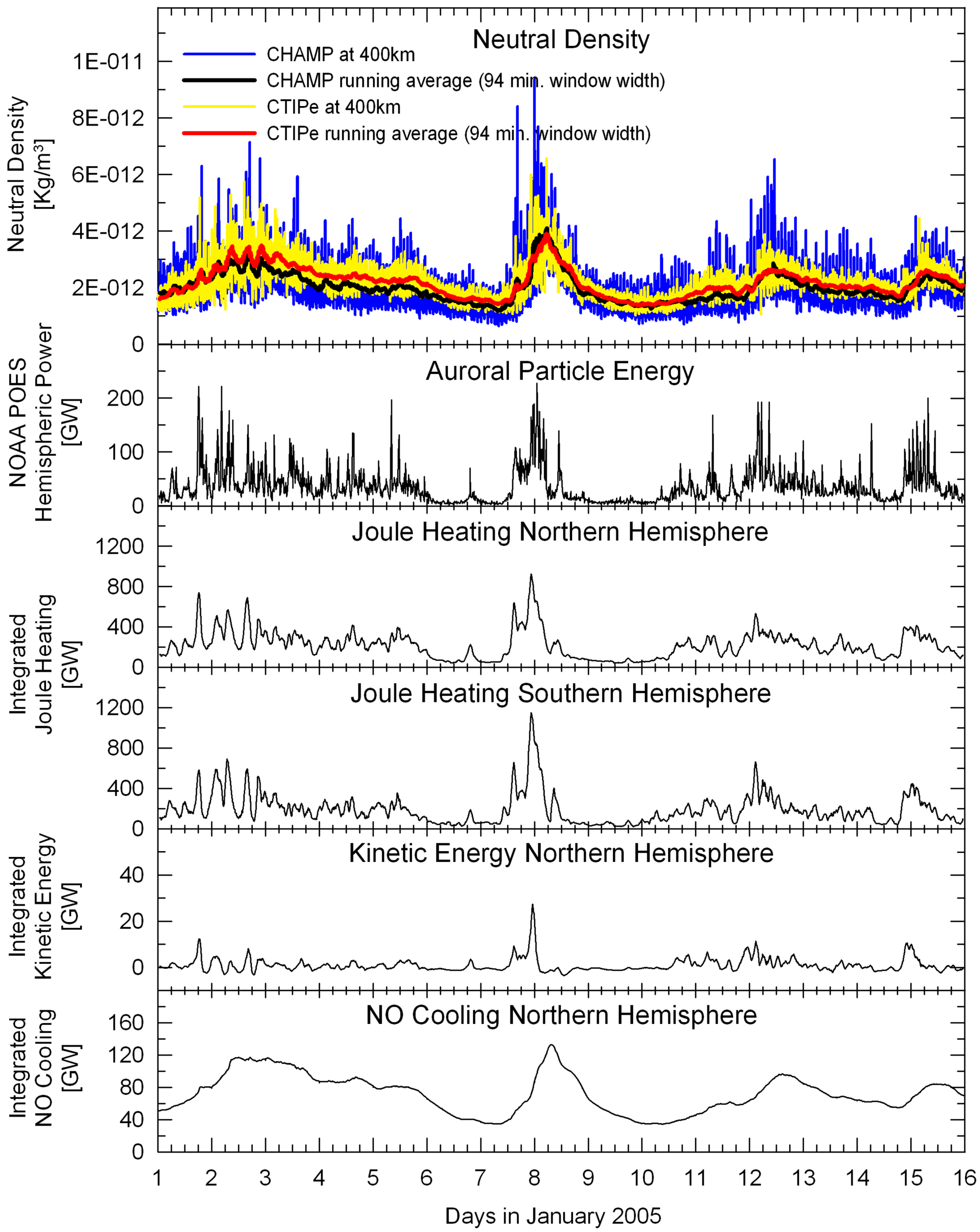

Fig. 12.1. Ionospheric properties during a geomagnetic storm. The upper panel shows a comparison of CHAMP neutral density measurements at 400 km altitude with a numerical simulation, for a stormy period in January 2005. The lower panels show, from top to bottom, estimates of auroral power, Joule heating in the Northern and Southern hemispheres, kinetic energy deposition, and nitric oxide infrared cooling rates (courtesy of M. Fedrizzi).

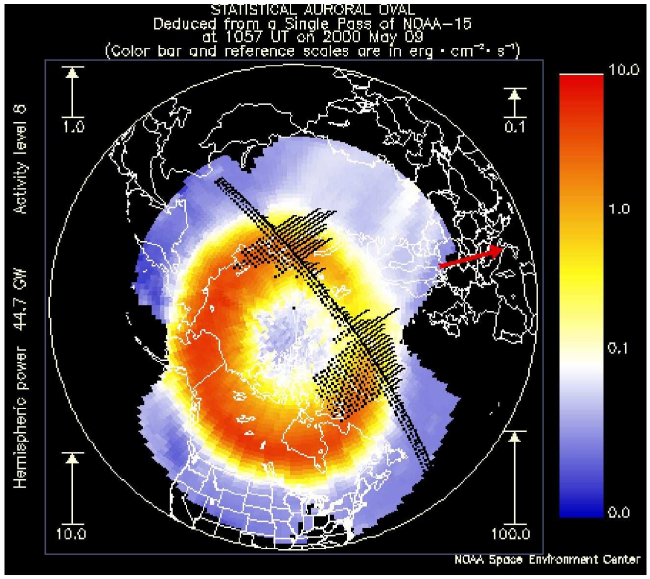

Fig. 12.2. Statistical pattern of auroral energy input derived from TIROS/NOAA satellite data during a single transit of the polar region (from Evans et al., 1988).

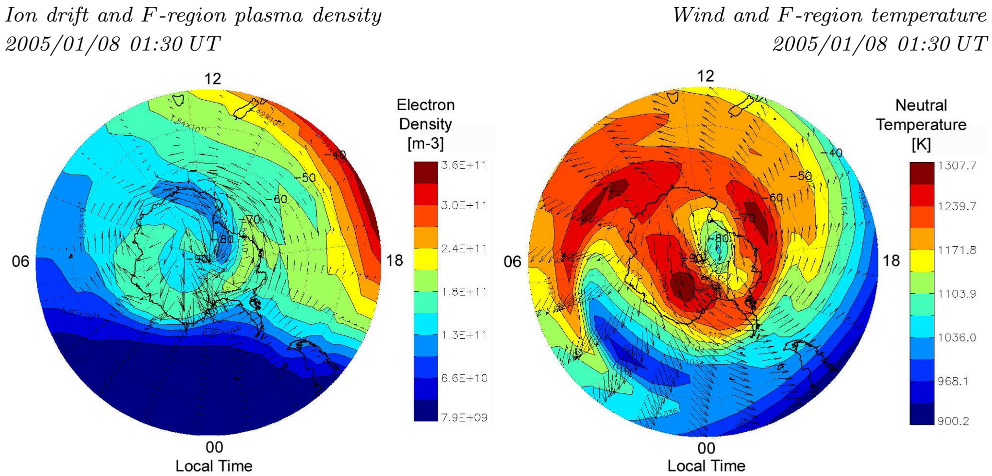

Fig. 12.3. Simulated response of the F-region plasma densities (left) and neutral winds and temperature (right) at the peak of the storm event at 1:30 UT on 2005/01/08 in the Southern hemisphere. Both represent the response in the upper thermosphere and ionosphere at about 300 km altitude. Peak neutral winds are in excess of 800 m/s (courtesy of M. Fedrizzi).

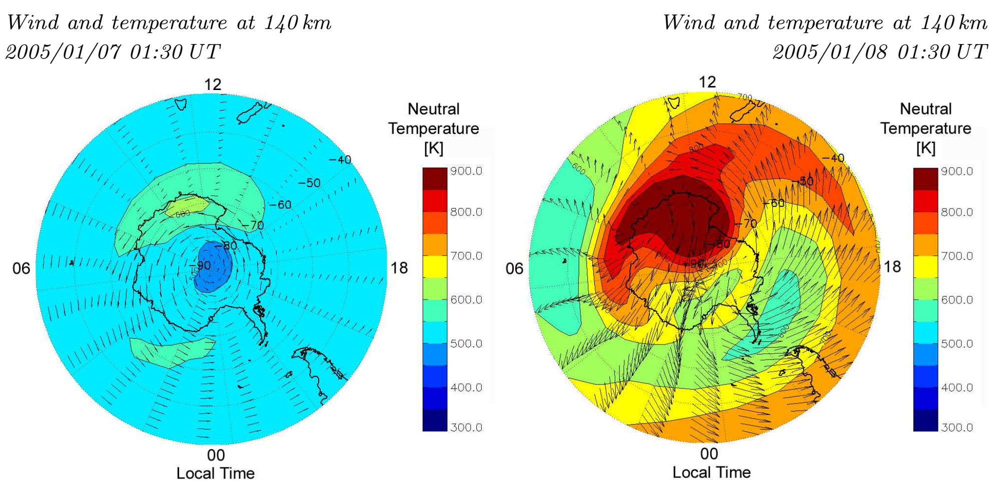

Fig. 12.4. Neutral winds in the lower thermosphere at around 140 km altitude at the peak of the storm at 1:30 UT on 2005/01/08 in the Southern hemisphere (right), and at the same UT on the quiet day preceding the storm (left). Winds in the lower thermosphere increase dramatically in response to the storm, but peak magnitudes are about half those at 300 km. Lower thermosphere winds driven by the storm also tend to be slower to dissipate, sometimes acting as a "flywheel" driving Poynting flux upward from the thermosphere/ionosphere to the magnetosphere (courtesy of M. Fedrizzi).

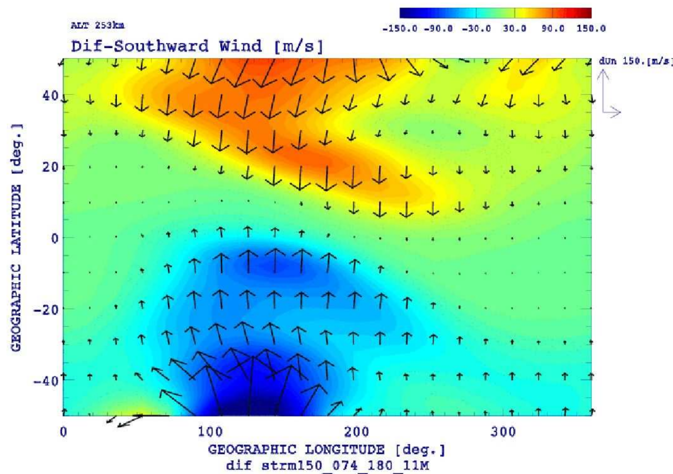

Fig. 12.5. Simulation of the response of the neutral winds at mid and low latitudes at 250 km altitude, shortly after a sudden increase in high-latitude Joule heating. The region within 50° of the geographic equator is shown at 15UT, three hours after the increase in high-latitude magnetospheric forcing, equivalent to a $K_p \sim 7$. Wind surges of ~ 150 m/s are produced, mainly on the night side.

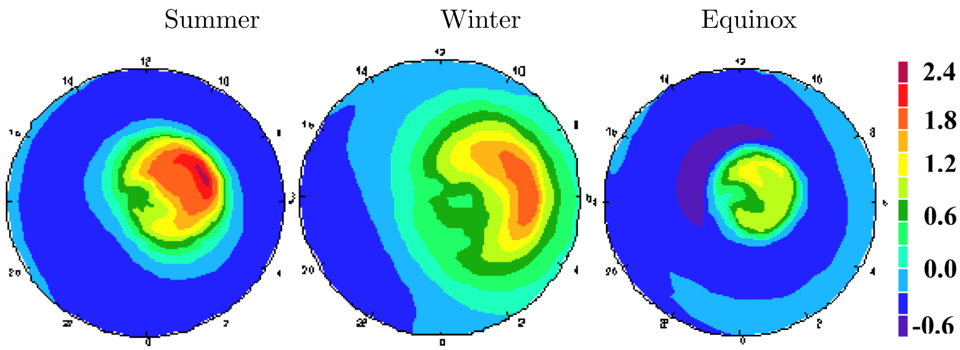

Fig. 12.6. Numerical simulations of the equatorward extent of the "composition bulge" at 12:00 UT, for equivalent storms in the Northern hemisphere for summer (left), winter (middle), and equinox (right). The seasonal circulation assists the transport to low latitudes in the summer hemisphere and inhibits the transport in winter.

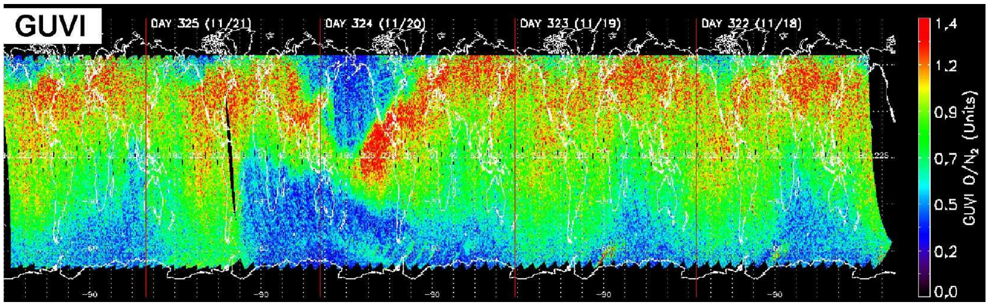

Fig. 12.7. Changes in the column-integrated O/N_2 ratio during the November 2003 Halloween storm (from review by Crowley et al., 2008; after Meier et al., 2005). The data are from the GUVI instrument on the TIMED satellite (Paxton et al., 1999). Five days of GUVI data are plotted as individual dayside orbits and assembled as a montage, time runs from right to left. The storm event on day 324 causes a decrease in the column integrated O/N_2 in both hemispheres. The Southern hemisphere depletion penetrates further equatorward as expected from the transport effect of the global seasonal circulation.

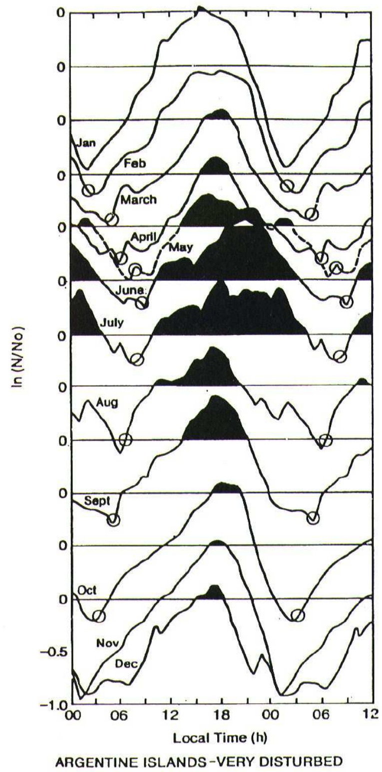

Fig. 12.8. The storm-time response of the ionosphere reveals both seasonal and local-time (LT) dependencies. The figure shows the diurnal variation of the natural logarithm of the ratio of the storm-to-quiet peak F-region plasma density, $NmF2$, at Argentine Islands (65°S) for 1971-1981. For reference, a decrease of 0.5 indicates a decrease in the plasma density by 40% (from Rodger et al., 1989).

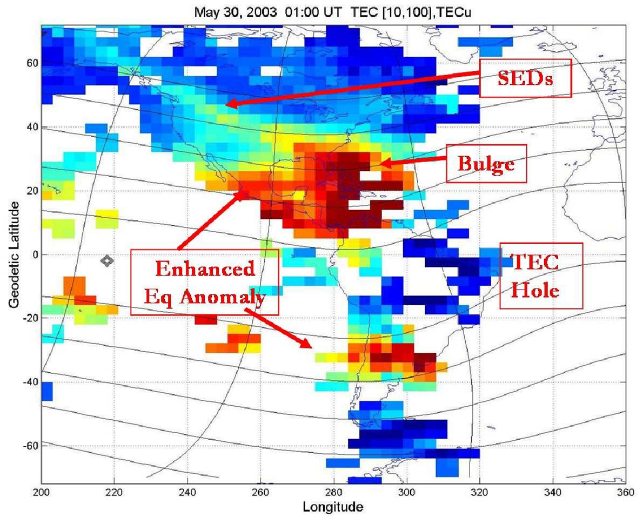

Fig. 12.9. Illustration of the large enhancement "bulge" in TEC at mid latitudes during a geomagnetic storm, and showing the plume of plasma (storm-enhanced density, or SED) connecting the bulge to the high latitudes (courtesy of J. Foster).

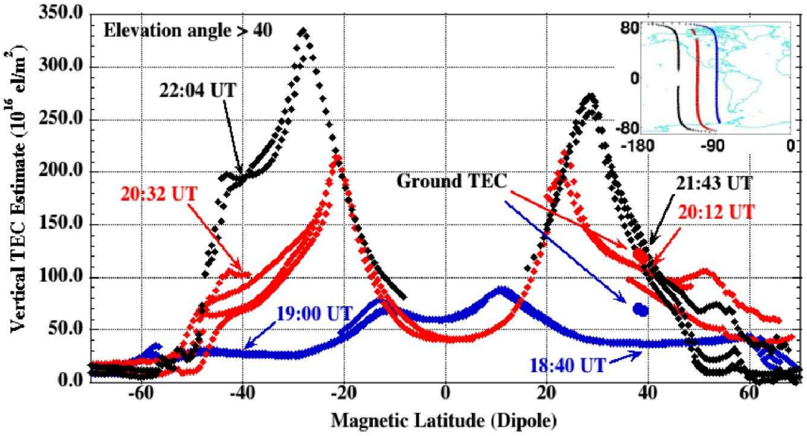

Fig. 12.10. Order of magnitude increases in over-the-satellite electron content (OSEC) above 400 km during the Halloween storm of 28 October 2003 as measured by the CHAMP satellite (from Mannucci et al., 2005).

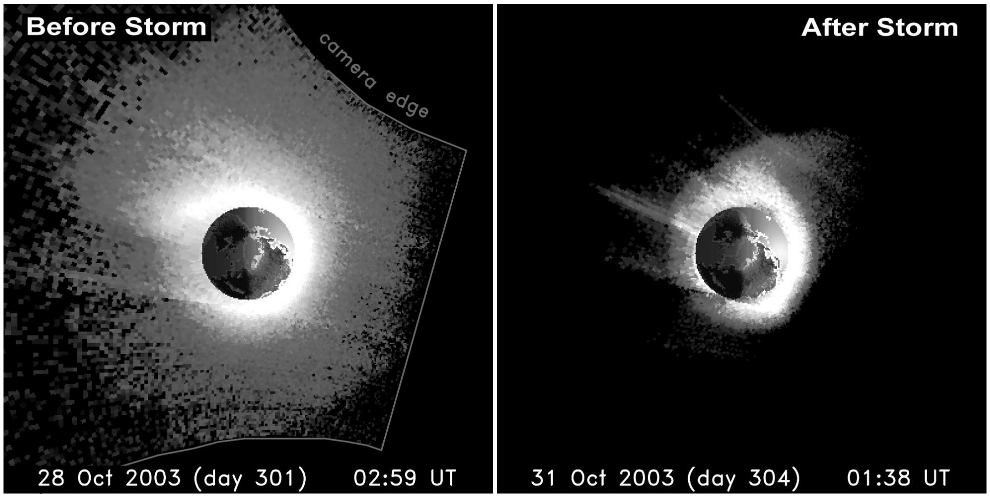

Fig. 12.11. Satellite observations of the erosion of the plasmasphere during a storm, from observations by the IMAGE satellite before and after the Halloween storm of 28 October 2003 (courtesy of J. Goldstein). The plasmaspheric tail, or plume, can be seen in the dusk section during the storm event.

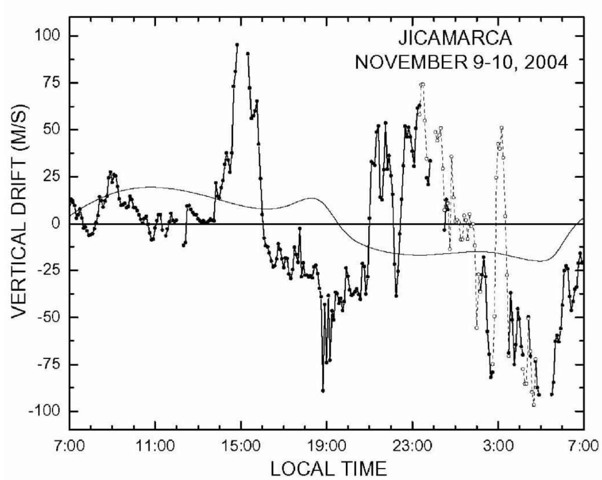

Fig. 12.12. Vertical plasma drift measured at the Jicamarca incoherent scatter radar facility in Peru on the magnetic equator (from Fejer et al., 2007) for a storm in November 2004. The thin line is the quiet day climatological drift.

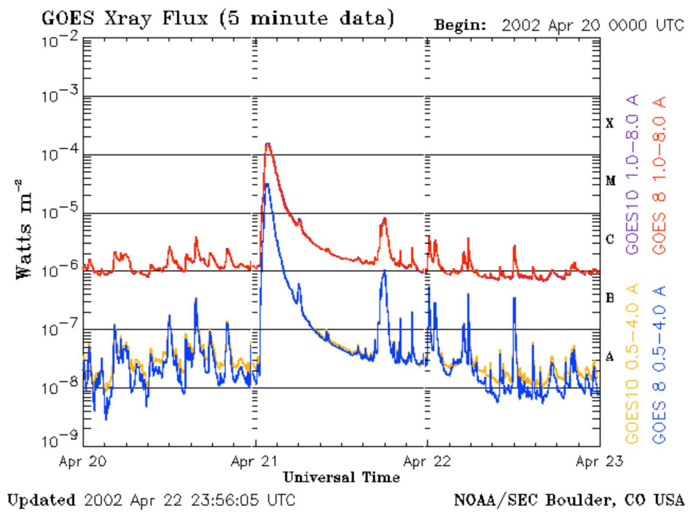

Fig. 12.13. Example of GOES XRS measurements during a large (X1.5) solar flare.

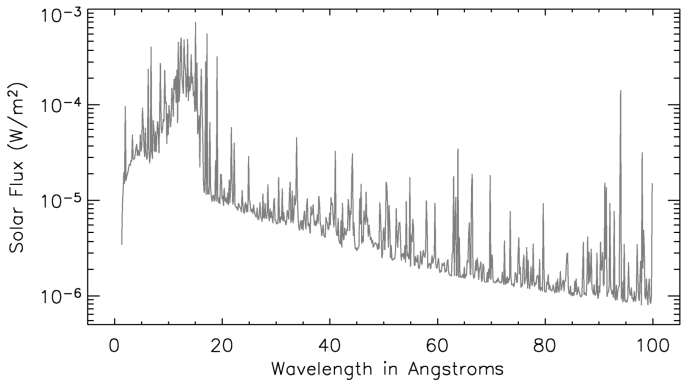

Fig. 12.14. Inferred flare enhancement spectrum in the soft X-ray region during the major flare on 28 October 2003, from Rodgers et al. (2006). This is an estimate of the amount of solar photon flux produced by the flare alone, i.e., the underlying pre-flare spectrum has been subtracted.

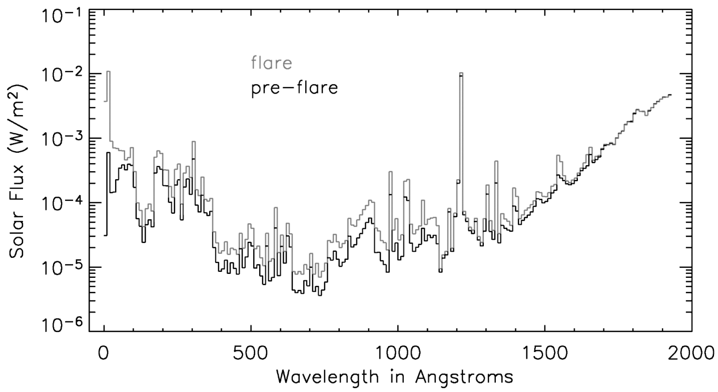

Fig. 12.15. Solar emission spectrum near the peak of the 28 October 2003 flare obtained from measurements by the TIMED/SEE instrument, compared to a spectrum obtained shortly before the event.

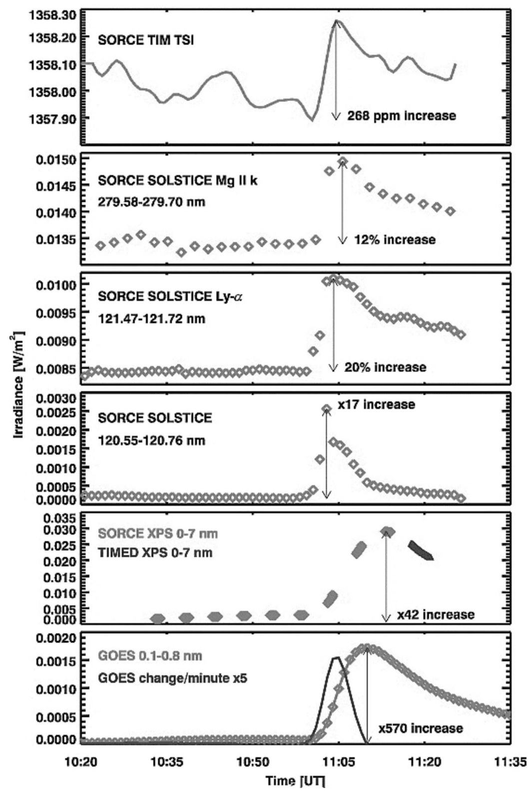

Fig. 12.16. Measurements from instruments on the SORCE satellite (Woods et al., 2004, 2008) showing the time dependence of flare enhancements in various spectral regions (from Woods et al. 2008).

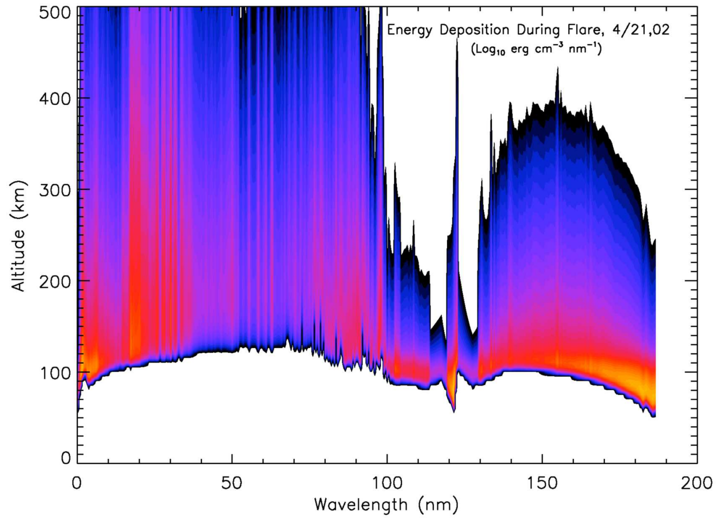

Fig. 12.17. Energy deposition in the upper atmosphere as a function of wavelength and altitude during a solar flare.

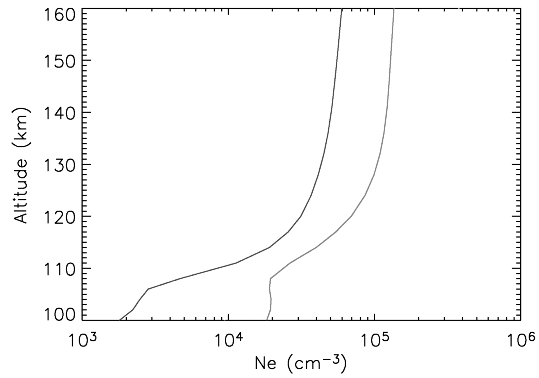

Fig. 12.18. Model calculation of electron density enhancement in the E region at high solar zenith angle (at the Sondrestrom radar site in Greenland) for the 28 October 2003 flare, using the spectrum shown in Figure 12.15 as input to a photo-ionization/photo-electron model. Black, lower-desity curve: pre-flare; grey, higher-density curve: flare. The enhancements seen are commensurate with radar observations of the flare effect.

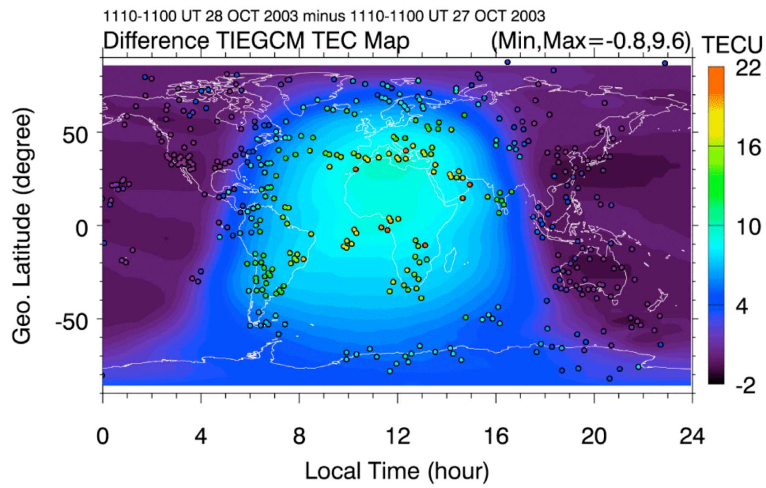

Fig. 12.19. Comparison of total electron content enhancements during the 28 October 2003 flare, observed by the global network of differential GPS stations, and modeled using the NCAR Thermosphere-Ionosphere-Electrodynamics General Circulation Model (TIE-GCM). Total electron content is the vertically-integrated column electron content in units of $10^{16}\,\mathrm{m}^{-2}$.

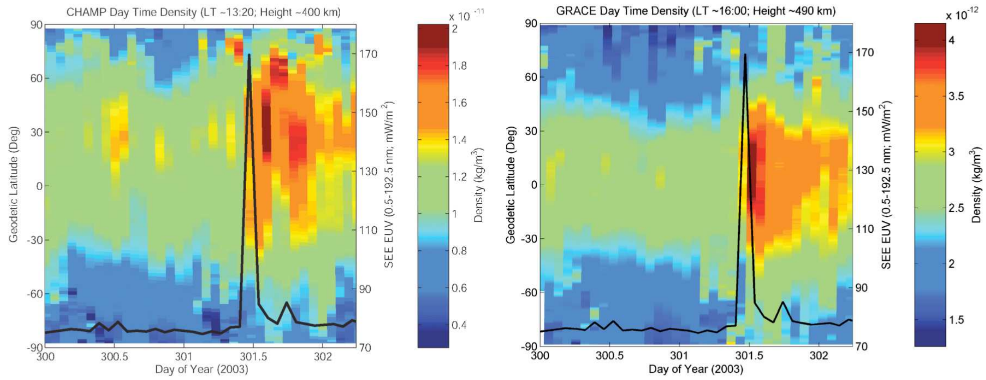

Fig. 12.20. Thermospheric density enhancements measured by accelerometers on the CHAMP satellite (altitude ∼400 km) and GRACE satellite (altitude ∼490 km) during the 28 October 2003 flare (Sutton et al., 2006).

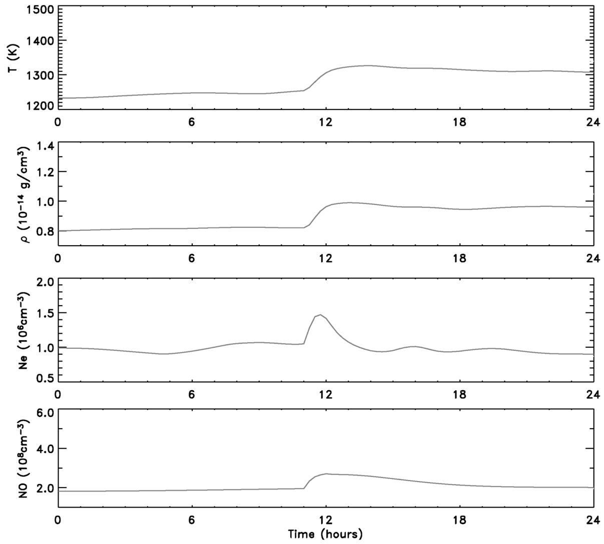

Fig. 12.21. Calculated enhancement and recovery of key thermospheric parameters in response to the 28 October 2003 flare using the NCAR TIE-GCM. Panel 1: neutral temperature at 400 km; panel 2: neutral mass density at 400 km; panel 3: electron density at 300 km; panel 4: nitric oxide density at 110 km. All calculations are at 12 noon local time at the equator.

13

Energetic particles and manned spaceflight

by Stephen Guetersloh and Neal Zapp

14
Energetic particles and technology

by Alan Tribble

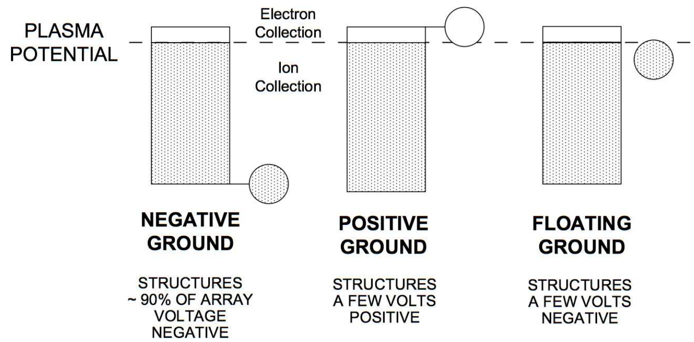

Fig. 14.1. Spacecraft floating potential vs. grounding options (from Tribble, 2000).

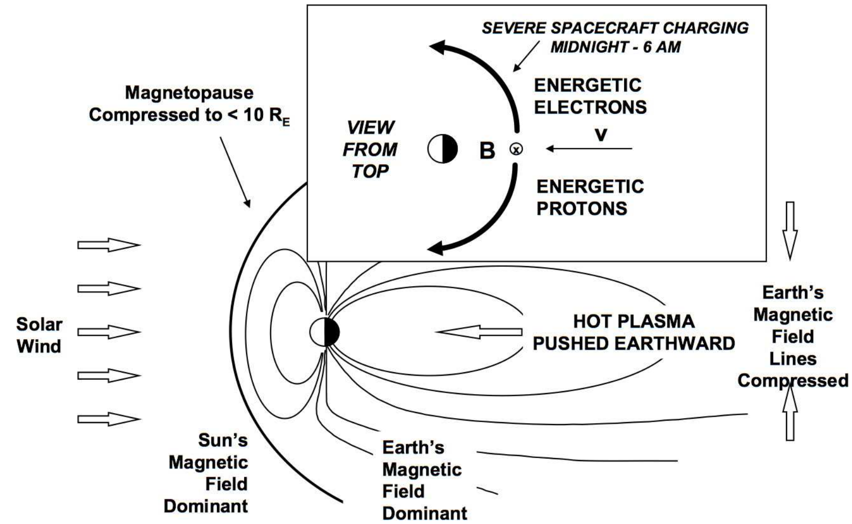

Fig. 14.2. Spacecraft charging in the geosynchronous environment at times of ICME-induced magnetic storms (from Tribble, 2003).

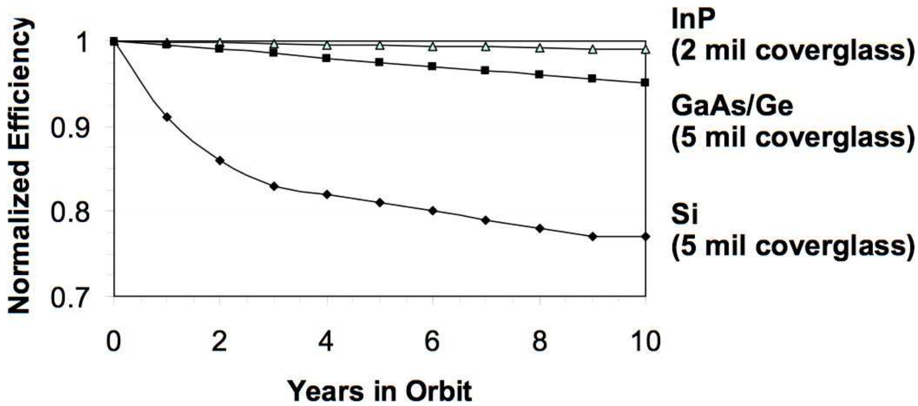

Fig. 14.3. Solar cell power loss vs. radiation (700 km altitude, 30° inclination orbit).

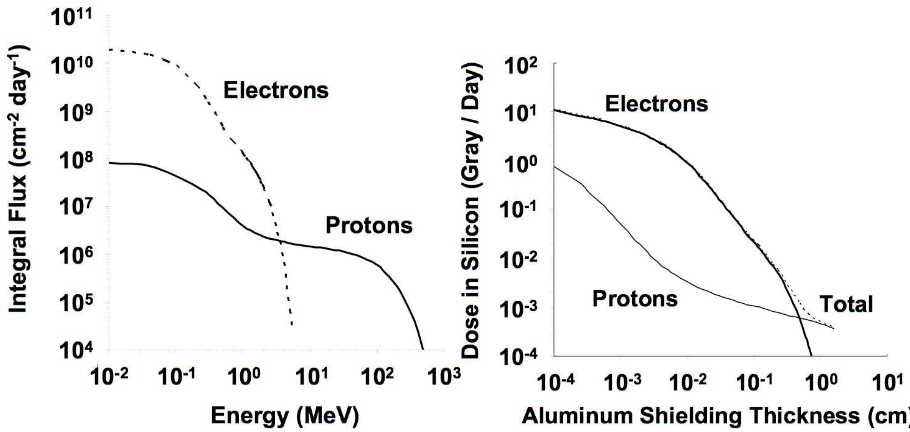

Fig. 14.4. International Space Station trapped-radiation environment *(left)* and total dose vs. shielding depth *(right)*.

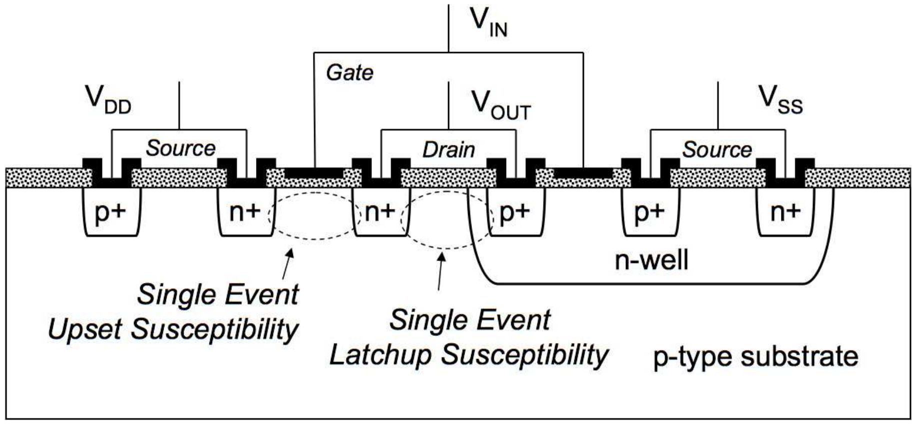

Fig. 14.5. Metal-oxide semiconductor field-effect transistor (MOSFET).

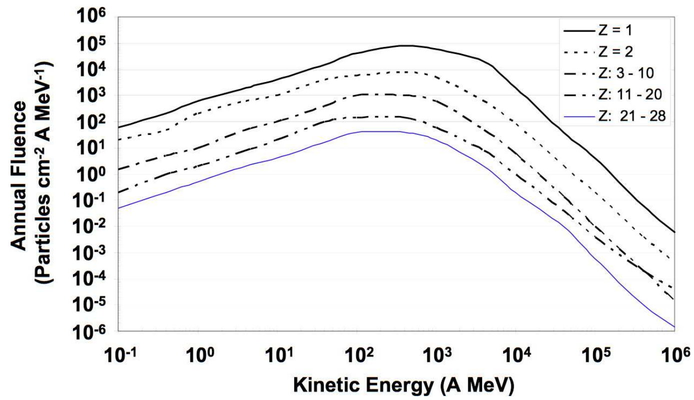

Fig. 14.6. The galactic cosmic ray annual fluence (A is the atomic mass number; A MeV is energy per nucleon). From Wilson et al. (1997).

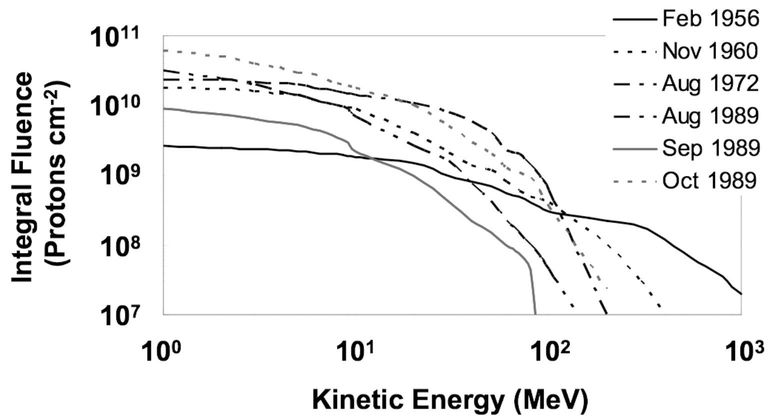

Fig. 14.7. Examples of monthly fluence of particles from solar particle events. From Wilson et al. (1997).

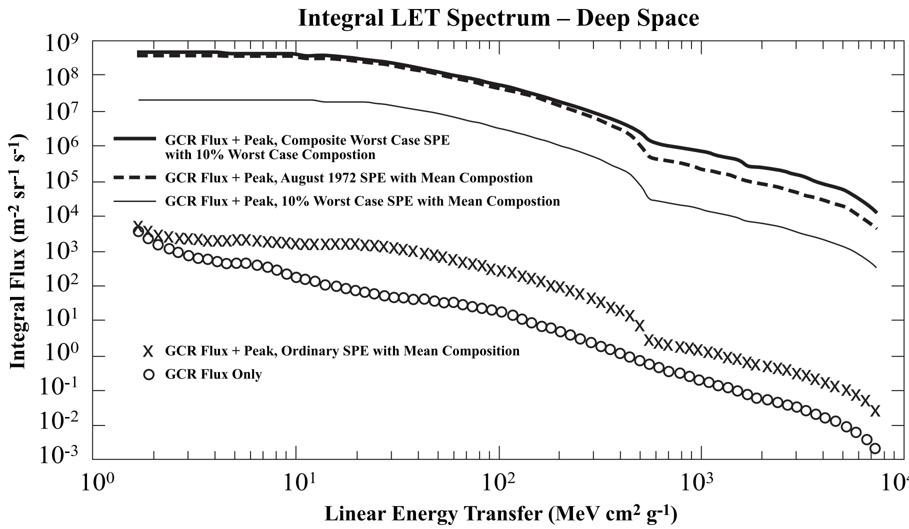

Fig. 14.8. Characteristic energetic particle fluxes as a function of the linear energy transfer (LET) of these particles, for the galactic cosmic ray (GCR) background and for different solar particle events (SPEs). In order to estimate the frequency of an interaction (e.g., upset, latchup, ...) within a device for a given type of SPE or GCR background, one first identifies the threshold value of LET where the interaction will occur (this is usually obtained from the manufacturer). Then one multiplies the integral flux $F_{\rm case}$ value corresponding to the LET threshold by the duration δt of the event or time interval in question and by the solid angle $\delta\omega$ from which the particles can reach the device: $f_{\rm case}(LET) = F_{\rm case}\delta t\,\delta\omega$.